REVIEWS OF MODERN PHYSICS, VOLUME 74, OCTOBER 2002

Electronic structure of quantum dots

Stephanie M. Reimann

Mathematical Physics, Lund Institute of Technology, 22100 Lund, Sweden

Matti Manninen

Department of Physics, University of Jyväskylä, 40351 Jyväskylä, Finland

(Published 26 November 2002)

The properties of quasi-two-dimensional semiconductor quantum dots are reviewed. Experimental techniques for measuring the electronic shell structure and the effect of magnetic fields are briefly described. The electronic structure is analyzed in terms of simple single-particle models, density-functional theory, and "exact" diagonalization methods. The spontaneous magnetization due to Hund's rule, spin-density wave states, and electron localization are addressed. As a function of the magnetic field, the electronic structure goes through several phases with qualitatively different properties. The formation of the so-called maximum-density droplet and its edge reconstruction is discussed, and the regime of strong magnetic fields in finite dot is examined. In addition, quasi-one-dimensional rings, deformed dots, and dot molecules are considered.

CONTENTS

I. Introduction 1284
A. Shell structure 1284
B. "Magic numbers" in finite fermion systems 1286
II. Quantum Dot Artificial Atoms 1287
A. Fabrication 1287
B. Coulomb blockade 1288
C. Probes of single-electron charging 1291
1. Gated transport spectroscopy 1292
2. Single-electron capacitance spectroscopy 1292
3. Transport through a vertical quantum dot 1293
III. Addition Energy Spectra 1293
A. Many-body effects in quantum dots 1294
B. Density-functional method 1295
C. Parabolic confinement 1296
D. Addition energy spectra described by mean-field theory 1296
E. Reproducibility of the experimental addition energy spectra 1298
F. Oscillator potential with flattened bottom 1298
G. Three-dimensionality of the confinement 1299
H. Triangular quantum dots 1300
I. Elliptic deformation 1300
J. Self-assembled pyramidal quantum dots in the local spin-density approximation 1302
IV. Internal Electronic Structure 1302
A. Classical electron configurations 1303
B. Spin polarization in the local spin-density approximation 1304
1. Circular and elliptic quantum dots 1304
2. Quantum wires and rings 1305
a. Quantum wires 1305
b. Quantum rings 1305
3. Artifacts of mean-field theory? 1306
C. Mean-field versus exact diagonalization 1306
D. Quasi-one-dimensional systems 1308
1. One-dimensional square well 1308
2. Quasi-one-dimensional quantum rings 1309
E. Quantum Monte Carlo studies 1310
1. Hund's rule 1310
2. Wigner crystallization 1311
V. Magnetic Fields: Addition Energy Spectra and a Single-Particle Approach 1311
A. Harmonic oscillator in a magnetic field 1312
1. Fock-Darwin spectrum and Landau bands 1312
2. Constant-interaction model 1312
B. Measurements of addition energy spectra 1313
1. Tunneling spectroscopy of vertical dots 1313
2. Gated transport spectroscopy in magnetic fields 1314
3. B-N phase diagram obtained by single-electron capacitance spectroscopy 1315
4. B-N phase diagram of large vertical quantum dots 1315
VI. Role of Electron-Electron Interactions in Magnetic Fields 1316
A. Exact diagonalization for parabolic dots in magnetic fields 1316
B. Electron localization in strong magnetic fields 1319
1. Laughlin wave function 1319
2. Close to the Laughlin state 1319
3. Relation to rotating Bose condensates 1320
4. Localization of electrons and the Laughlin state 1321
5. Localization and the many-body spectrum 1322
6. Correlation functions and localization 1323
VII. Density-Functional Approach for Quantum Dots in Magnetic Fields 1324
A. Current spin-density-functional theory 1324
B. Parametrization of the exchange-correlation energy in a magnetic field 1325
C. Ground states and addition energy spectra within the symmetry-restricted current-spin-density-functional theory 1325
1. Angular momentum transitions 1325
2. Addition energy spectra in magnetic fields 1326
D. Reconstruction of quantum Hall edges in large systems 1326
1. Edge reconstruction in current-spin-density-functional theory 1327
2. Phase diagram 1327
E. Edge reconstruction and localization in unrestricted Hartree-Fock theory 1328

F. Ensemble density-functional theory and noncollinear spins 1328
VIII. Quantum Rings in a Magnetic Field 1329
A. Electronic structure of quantum rings 1329
B. Persistent current 1331
IX. Quantum Dot Molecules 1331
A. Lateral-dot molecules in the local spin-density approximation 1333
B. Vertical double dots in the local spin-density approximation 1334
C. Exact results for vertical-dot molecules in a magnetic field 1334
D. Lateral-dot molecules in a magnetic field 1335
X. Summary 1335
Acknowledgments 1336
References 1336

I. INTRODUCTION

Low-dimensional nanometer-sized systems have defined a new research area in condensed-matter physics within the last 20 years. Modern semiconductor processing techniques allowed the artificial creation of quantum confinement of only a few electrons. Such finite fermion systems have much in common with atoms, yet they are man-made structures, designed and fabricated in the laboratory. Usually they are called "quantum dots," referring to their quantum confinement in all three spatial dimensions. A common way to fabricate quantum dots is to restrict the two-dimensional electron gas in a semiconductor heterostructure laterally by electrostatic gates, or vertically by etching techniques. This creates a bowl-like potential in which the conduction electrons are trapped. In addition to the many possibile technological applications, what makes the study of these "artificial atoms" or "designer atoms" (Maksym and Chakraborty, 1990; Chakraborty, 1992, 1999; Kastner, 1992, 1993; Reed, 1993; Alivisatos, 1996; Ashoori, 1996; McEuen, 1997; Kouwenhoven and Marcus, 1998; Gammon, 2000) interesting are the far-reaching analogies to systems that exist in Nature and have defined paradigms of many-body physics: atoms, nuclei, and, more recently, metallic clusters (see, for example, the reviews by Brack, 1993 and de Heer, 1993) or trapped atomic gases [see the Nobel lectures by Cornell, 2001, Ketterle, 2001, and Wieman, 2001, and, for example, the reviews by Dalfovo *et al.*, 1999, and Leggett, 2001 and the recent book by Pethick and Smith (2002)]. Quantum dots added another such paradigm. Their properties can be changed in a controlled way by electrostatic gates, changes in the dot geometry, or applied magnetic fields. Their technological realization gave access to quantum effects in finite low-dimensional systems that were largely unexplored.

After the initial success in the fabrication and control of mesoscopic semiconductor structures, which are typically about one hundred nanometers in size and confine several hundred electrons, many groups focused on the further miniaturization of such devices. A breakthrough to the "atomic" regime was achieved with the experimental discovery of shell structure in fluctuations of the charging energy spectra of small, vertical quantum dots (Tarucha *et al.*, 1996): the borderline between the physics of bulk condensed matter and few-body quantum systems was crossed. Much of the many-body physics that was developed for the understanding of atoms or nuclei could be applied. In turn, measurements on artificial atoms yielded a wealth of data from which a fundamental insight into the many-body physics of low-dimensional finite fermion systems was obtained (Kouwenhoven, Austing, and Tarucha, 2001). With further progress in experimental techniques, artificial atoms will continue to be a rich source of information on many-body physics and undoubtedly will hold a few surprises.

The field of nanostructure physics has been growing rapidly in recent years, and much theoretical insight has been gained hand in hand with progress in experimental techniques and more device-oriented applications. Reviewing the whole, very broad and still expanding field would be an almost impossible task, given the wealth of literature that has been published in the last decade. We thus restrict this review to a report on the discovery of shell structure in artificial atoms (with a focus on well-controlled dots in single-electron transistors) and summarize aspects of theoretical research concerning the electronic ground-state structure and many-body physics of artificial atoms. (A review of the statistical theory of quantum dots, with a focus on chaotic or diffusive electron dynamics, was recently provided by Alhassid, 2000.) In our analysis of shell structure, we shall be guided by several analogies to other finite quantal systems that have had a major impact on both theoretical and experimental research on quantum dots: the chemical inertness of the noble gases, the pronounced stability of "magic" nuclei, and enhanced abundances in the mass spectra of metal clusters.

A. Shell structure

The simplest approach to a description of finite quantal systems of interacting particles is based on the idea that the interactions, possibly together with an external confinement, create an average "mean field," which, on an empirical basis, can be approximated by an effective potential in which the particles are assumed to move independently. This *a priori* rather simple idea forms the basis of Hartree, Hartree-Fock, and density-functional theories. The last, with its many extensions, provides powerful techniques for electronic structure calculations and is nowadays applied extensively in many different areas of both physics and chemistry (see the Nobel lectures by Kohn, 1999, and Pople, 1999).

The distribution of single-particle energy levels of the mean-field potential can be nonuniform, and bunches of degenerate or nearly degenerate levels, being separated from other levels by energy gaps, can occur. Such grouping of levels or the formation of *shells* (as shown schematically in Fig. 1) is a consequence of both the dimensionality and the symmetry of the mean-field potential. A high degree of symmetry results in a pronounced level bunching (Brack *et al.*, 1972). This level bunching is manifested in many of the physical properties of finite,

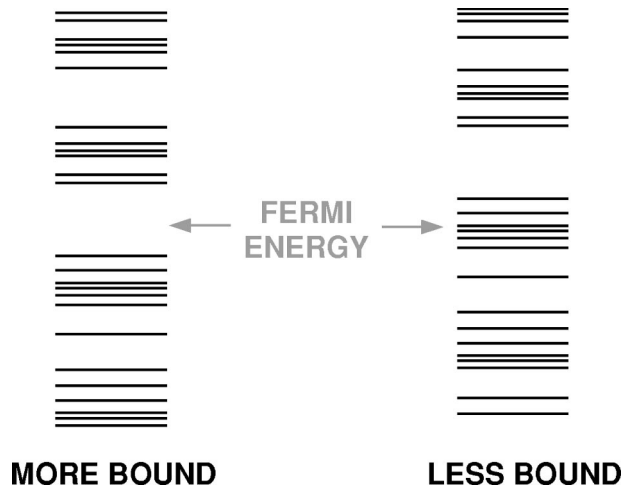

FIG. 1. Schematic illustration of the bunching of single-particle states (shell structure) in a finite fermion system. The binding energy is lower if the single-particle level density at the Fermi energy has a minimum. After Brack *et al.*, 1972.

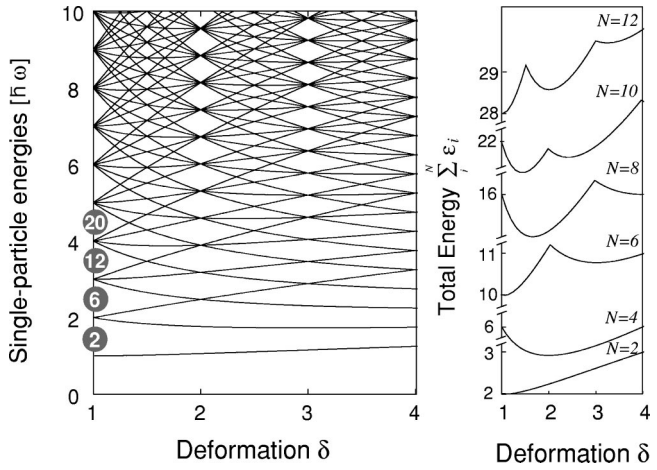

FIG. 2. Effects of deformation. Left: Single-particle states of a two-dimensional anisotropic harmonic oscillator as a function of deformation ($\delta>1$). Degeneracies in the isotropic case ($\delta=1$) lead to closed shells for $N=2,6,12,20,\ldots$ (for noninteracting fermions, including spin degeneracy) and subshells occur at frequency ratios $\delta=q/p$ for integer q,p. Right: Total energies $\Sigma_{n_x,n_y}\varepsilon_{n_x,n_y}$ of the anisotropic harmonic oscillator for $N=2$, 4, 6, 8, 10, and 12 noninteracting particles as a function of deformation.

quantal many-fermion systems, such as, for example, their stability, ionization energies, chemical reactivity, or conductance.

The density of single-particle states at the Fermi surface is of particular importance for the stability of the system. If it is at a minimum, the particles occupy states with a smaller energy on average, and consequently the system is more bound: shell filling leads to particularly stable states. If a shell is not filled, however, the system can stabilize itself by spontaneously breaking its internal symmetry. For atomic nuclei, for example, such a spatial deformation of the mean field was confirmed by an analysis of rotational spectra (see Bohr and Mottelson, 1975, and the review by Alder *et al.*, 1956). More recently, similar effects were observed from plasmon resonances of metallic clusters, as reviewed by Brack (1993), and de Heer (1993).

In a finite quantal system of fermions, the stability condition is that there be no unresolved degeneracy at the Fermi surface. This condition is met for certain numbers of confined particles, for which a degenerate shell with a large energy gap to the next unoccupied shell can be filled. We illustrate this with the example of an anisotropic harmonic-oscillator confinement in two dimensions (x,y),

$$V(x,y)=\frac{1}{2}m^*\omega^2\left(\delta x^2+\frac{1}{\delta}y^2\right), \tag{1}$$

as an empirical mean-field potential in which a number N of fermions with an effective mass m^* are assumed to move independently. The ratio $\delta=\omega_x/\omega_y$ with frequencies $\omega_x=\omega\sqrt{\delta}$ and $\omega_y=\omega/\sqrt{\delta}$ defines the ratio of semiaxes of the ellipse equipotentials. Imposing the constraint $\omega^2=\omega_x\omega_y$ conserves their area with deformation. The corresponding single-particle energy spectrum,

$$\varepsilon_{n_x,n_y}(\delta)=\hbar\omega\left[\left(n_x+\frac{1}{2}\right)\sqrt{\delta}+\left(n_y+\frac{1}{2}\right)\Big/\sqrt{\delta}\right], \tag{2}$$

is shown as a function of deformation δ in Fig. 2 (left). In the isotropic case $\delta=1$, one clearly recognizes the (N_0+1)-fold degeneracy for a principal quantum number $N_0=n_x+n_y=0,1,2,\ldots$. By filling the states with noninteracting fermions, respecting the Pauli principle, and including spin degeneracy with a factor of 2, one can reach closed shells for a sequence of $N=2,6,12,20,\ldots$ particles. For these configurations, particular stability is reached, as the degeneracy of the shell is resolved and the density of states is minimal at the Fermi energy. Adding one more electron to a closed shell would result in single occupancy of an orbit belonging to the next higher shell, and the system would be less stable. In the case of open shells, however, the degeneracy can be lowered by deformation and an energetically more favorable configuration can be reached. (This phenomenon is known as the Jahn-Teller effect; Jahn and Teller, 1937.) In particular, for noncircular shapes, subshells with degeneracies comparable to the nondeformed case can occur, leading to a pronounced stability at the corresponding deformation (Geilikman, 1960; Wong, 1970). Figure 2 (right) shows the total energies $\Sigma_{n_x,n_y}\varepsilon_{n_x,n_y}(\delta)$. We see that depending on the number of confined particles and deformation, cusps and minima in the total energy occur for $\delta>1$ at frequency ratios where more pronounced subshells are formed. As is obvious from the shell patterns in the single-particle spectra, configurations with $N=2$, 6, or 12 particles have the lowest energies in the isotropic case, while for $N=4$, 8, or 10, the energy can be lowered by deformation.

Despite the simplicity of this example, it contains some of the basic features of a finite, fermionic quantum system: the occurrence of shells and the corresponding stability for closed-shell configurations, and the ten-

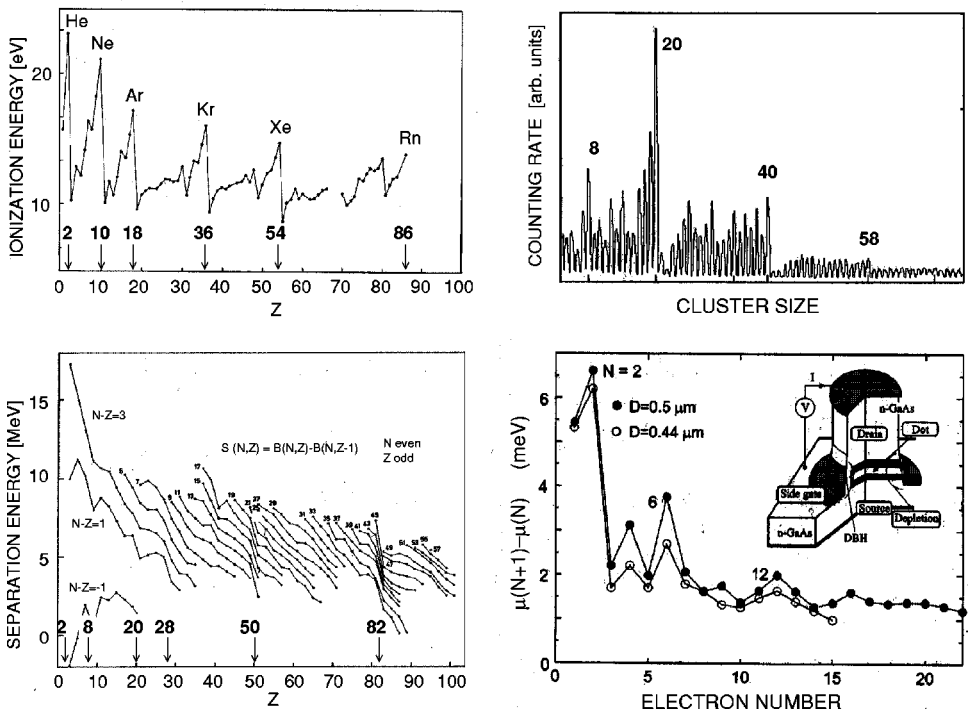

FIG. 3. Shell structure and "magic numbers" in finite fermion systems. Upper left, atomic ionization energies; lower left, separation energies of atomic nuclei (after Bohr and Mottelson, 1975); upper right, abundance spectra of metallic clusters (counting rate in arbitrary units), (after Knight *et al.*, 1984); lower right, differences in the chemical potential $\mu(N+1)-\mu(N)$ of disk-shaped quantum dots; inset, device setup, schematic (from Tarucha *et al.*, 1996).

dency to spontaneously break the symmetry of the mean field in the case of open shells. Subshell closings enhance the stability of the broken-symmetry states compared to the nondeformed, open-shell system.

B. "Magic numbers" in finite fermion systems

The Periodic Table, with the appearance of its eight groups of elements showing similar chemical properties, is the most widely appreciated example of shell structure. *Atomic shells* are most strikingly seen in the pronounced maxima of the ionization energies of neutral atoms for certain atomic numbers $Z=2,10,18,\ldots$, corresponding to the noble gases He, Ne, Ar,... (see upper left panel of Fig. 3). The spherical symmetry of the very rigid confinement of the electrons caused by the strong Coulomb potential of the nucleus results in large degeneracies at the midshell regions. These shells are then populated according to Hund's rules: due to the Pauli principle and the repulsive Coulomb interaction, the spin is maximized for half filled orbitals. (Note that in nuclei the interaction is attractive, and consequently the spins are paired off.)

In nuclei, the separation energy (i.e., the energy that is required to remove a nucleon from the nucleus) of neutrons and protons shows distinct steps for certain particle numbers, originating from the shell structure (lower left panel of Fig. 3). These steps are very similar to the abrupt decrease of the atomic ionization potentials for electron numbers that exceed the atomic shell closings by one.

Parametrizing an average mean-field potential and including spin-orbit coupling, Goeppert-Mayer (1949) and Haxel, Jensen, and Suess (1949) could formulate a shell model that successfully explained the "magic numbers" of nucleons for which particular stability was observed.

In the early 1980s, finite-size *clusters of atoms* attracted much interest: they provided a link between the physics of single atoms or the smallest molecules, and the solid. Knight *et al.* (1984) succeeded in fabricating clusters consisting of from a few up to hundreds of alkali atoms by supersonic expansion of a mixture of metal atoms and a carrier gas through a tiny nozzle. Condensation of droplets and subsequent evaporation of single atoms until equilibrium was reached produced stable clusters that could then be counted and size selected. The anomalies in the mass abundance spectra, i.e., the counting rates of clusters with a given number of atoms per cluster, are striking: for certain numbers of atoms, one observes an enhanced stability of the cluster. The upper right panel of Fig. 3 shows the cluster counting rate (in arbitrary units) as a function of the number of atoms per cluster: pronounced maxima are observed for clusters with 2, 8, 20, 40, and 58 atoms. This reminds us of the magic numbers in nuclei mentioned above. A metal cluster can be described in a simple model that assumes that the delocalized valence electrons experience a homogeneous positively charged background ("*jellium*") of the atom ions. This approach has long been used in solid-state physics to describe, for example, metal surfaces (Lang and Kohn, 1970; Monnier and Perdew, 1978) or voids in metals (Manninen *et al.*, 1975; Manninen and Nieminen, 1978). Indeed, the jellium model of metals provided an explanation for the enhanced stability of clusters with specific sizes. Density-functional calculations for electrons confined by a spherical jellium of sodium ions (Martins *et al.*, 1981, 1985; Hintermann and Manninen, 1983; Beck, 1984; Chou *et al.*, 1984; Ekardt, 1984) actually had suggested the enhanced stability of closed-shell configurations for sodium clusters with $N=2$, 8, 20, 34(40), or 58 atoms

shortly before their experimental discovery in 1984. For large cluster sizes, theoretical and experimental evidence for a supershell structure, i.e., a beating pattern that envelopes the shell oscillations, was found in 1990 (Nishioka, Hansen, and Mottelson, 1990; Pedersen *et al.*, 1991). Much experimental and theoretical effort was devoted in the following years to detailed studies of the electronic and geometric structure of metallic clusters and their physical and chemical properties. (For a review of shell structures in metallic clusters, see Brack, 1993, de Heer, 1993, and the recent monograph by Ekardt, 1999).

In beautiful analogy to atoms, nuclei, or clusters, shell structure can also be observed in the conductance spectra of small semiconductor quantum dots. As an example, the inset to Fig. 3 (lower right panel) schematically shows the device used by Tarucha *et al.* (1996): in an etched pillar of semiconducting material, a small, quasi-two-dimensional electron island is formed between two heterostructure barriers. The island can be squeezed electrostatically by applying a voltage to the metallic side gate that is formed around the vertical structure. The dot is connected to macroscopic voltage and current meters via the source and drain contacts. Measuring the current as a function of the voltage on the gates at small source-drain voltage, one observes current peaks for each single electron subsequently entering the dot (see Sec. II.B). The spacing between two subsequent current peaks is proportional to the difference in energy needed to add another electron to a dot already confining N particles. This quantity is plotted in Fig. 3 (lower right panel) for two different dots with diameters $D=0.5$ μm and $D=0.44$ μm and shows large amplitudes at electron numbers $N=2$, 6, and 12. Indeed, these numbers correspond to closed shells of a two-dimensional harmonic oscillator. As we shall see, the additional structures at the midshell regions are a consequence of spin alignment due to Hund's rules, in analogy to the atomic ionization spectra (Zeng, Goldman, and Serota, 1993; Tarucha *et al.*, 1996; Franceschetti and Zunger, 2000).

II. QUANTUM DOT ARTIFICIAL ATOMS

Quantum dots constitute an excellent model system in which to study the many-body properties of finite fermionic systems. Without attempting to review the many experimental techniques that have been developed, we provide in this section a brief introduction to the fabrication of these man-made structures (Sec. II.A). A substantial amount of information on the electronic properties of quantum dots is drawn from conductance measurements. Here the discrete nature of the electron charge manifests itself as a Coulomb blockade. This important feature is discussed in Sec. II.B, and more details are given in Sec. II.C regarding the different types of experimental setups for studying the level spacing.

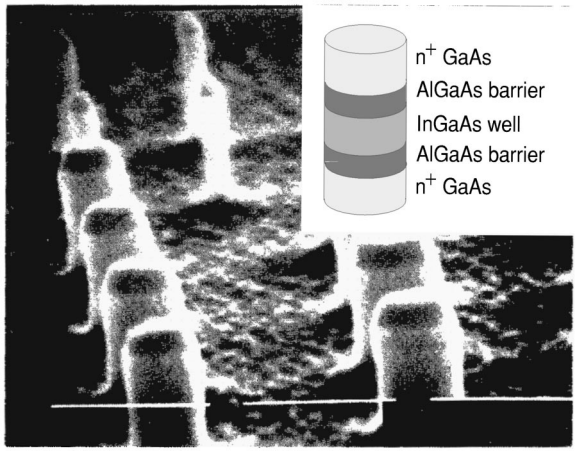

FIG. 4. Scanning electron micrograph showing etched quantum dots. (The white bars have a length of 0.5 μm.) Inset, schematic picture of a single dot structure. After Reed *et al.*, 1988.

A. Fabrication

The development in the early 1970s of superlattice structures (Esaki and Tsu, 1970; Chang *et al.*, 1973) and the demonstration of carrier confinement in reduced dimensions by electron and optical spectroscopy in GaAs-AlGaAs quantum wells (Chang, Esaki, and Tsu, 1974; Dingle, Gossard, and Wiegmann, 1974; Esaki and Chang, 1974) were of crucial importance for further developments in semiconductor physics. With the trend toward miniaturizing electronic devices, systems based on a quasi-two-dimensional electron gas (which can form in heterostructures, quantum wells, or metal-oxide semiconductor devices; see Ando, Fowler, and Stern, 1982) attracted much attention. By applying metallic gate patterns or etching techniques, it became possible to further restrict a two-dimensional electron gas to geometries in which the carriers are confined to a "wire" (i.e., a quasi-one-dimensional system) or a "dot," where the carrier motion is restricted in all three spatial directions (i.e., a "zero-dimensional" system).

Experiments on quantum wires like those, for example, reported in the very early work of Sakaki (1980), led to further investigations of the localization and interaction effects in one-dimensional systems (Wheeler *et al.*, 1982; Thornton *et al.*, 1986). For the fabrication of zero-dimensional artificial atoms and the search for experimental evidence of energy quantization, various approaches were taken in the beginning.[1] Regarding the observation of energy quantization, Reed *et al.* (1988) performed pioneering experimental studies on etched heterostructure pillars. Figure 4 shows a scanning electron micrograph of these dot structures, which had electric contacts on their top and bottom, respectively.

[1]See, among others, Smith *et al.*, 1987, 1988; Hansen *et al.*, 1989, 1990; Sikorski and Merkt, 1989; Demel *et al.*, 1990; Lorke, Kotthaus, and Ploog, 1990; Silsbee and Ashoori, 1990; Meurer, Heitmann, and Ploog, 1992.

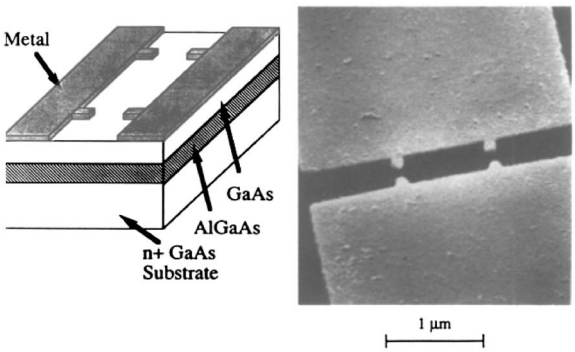

FIG. 5. Lateral device structure. Left, schematic drawing of a lateral device structure; right, scanning electron micrograph of the sample. From Meirav, Kastner, and Wind, 1990.

(A schematic drawing of the double-barrier heterostructure is shown as an inset in Fig. 4.) Measuring the current-voltage characteristics of single dots, Reed *et al.* (1988) reported evidence that electron transport indeed occurred through a discrete spectrum of quantum states.

Single-electron tunneling and the effect of Coulomb interactions in asymmetric quantum pillars was also discussed by Su, Goldman, and Cunningham (1992a, 1992b). Guéret *et al.* (1992) built an etched double-barrier vertical-dot structure, surrounded by a metallic and a separately biased Schottky gate, that allowed a variable control of the lateral confinement. In addition to avoiding edge defects and allowing for a rather smooth confinement of the electrons, with this device one can control the effective size of the quantum dot by varying the voltage on the vertical gate. Despite these efforts, it was not until 1996 when, with a rather similar setup (see the inset to the lower right panel in Fig. 3), Tarucha *et al.* could obtain for the first time very clear experimental evidence for energy quantization and shell structure on a truly microscopic level. We shall return to these measurements and their theoretical analysis later on.

Another method frequently used to create quantum confinement in a semiconductor heterostructure is the lithographic patterning of gates, i.e., the deposition of metal electrodes on the heterostructure surface. An example is shown in Fig. 5, here for an inverted GaAs-AlGaAs heterostructure. Application of a voltage to the top gate electrodes confines the electrons of the two-dimensional electron gas that is formed at the interface between the different semiconductor materials (see Meirav, Kastner, and Wind, 1990).

Other examples of the creation of quantum dots are the selective and self-assembled growth mechanisms of semiconducting compounds (Petroff *et al.*, 2001). In the Stranski-Krastanow process (Stranski and von Krastanow, 1939), a phase transition from epitaxial structure to islands with similar sizes and regular shapes takes place, depending on the misfit of the lattice constants (strain) and the growth temperature. For a description of the self-organized growth of quantum dots at the surfaces of crystals we refer the reader to the monograph by Bimberg, Grundmann, and Ledentsov (1999). The growth conditions determine the form of self-assembled dots, which, for example, can be pyramidal, disk shaped or lens shaped (Marzin *et al.*, 1994; Petroff and Denbaars, 1994; Grundmann *et al.*, 1995; Notzel *et al.*, 1995). Drexler *et al.* (1994), Fricke *et al.* (1996), Miller *et al.* (1997), and Lorke and Luyken (1997, 1998) probed the ground states and electronic excitations of small self-assembled quantum dots and rings by far-infrared and capacitance spectroscopy. Double layers of vertically aligned quantum dots were investigated by Luyken *et al.* (1998). A theoretical analysis of the few-electron states in lens-shaped self-assembled dots compared well with the experimental results of Drexler *et al.* (1994) and showed that the calculated charging and infrared absorption spectra reflect the magnetic-field-induced transitions between different states of interacting electrons (Wójs and Hawrylak, 1996). Ullrich and Vignale (2000) were the first to provide time-dependent spin-density-functional calculations of the far-infrared density response in magnetic fields and were able to reproduce the main features of the far-infrared spectroscopy measurements by Fricke *et al.* (1996) and Lorke *et al.* (1997). Fonseca *et al.* (1998) performed an analysis of the ground states of pyramidal self-assembled dots within spin-density-functional theory, as discussed briefly in Sec. III.J.

Quantum dots and quantum wires can also be fabricated by the so-called cleaved-edge overgrowth (Pfeiffer *et al.*, 1990; see also Wegscheider, Pfeiffer, and West, 1996 and Wegscheider and Abstreiter, 1998). Much experimental and theoretical work has concentrated on optical excitations, as summarized in the monograph by Jacak, Hawrylak, and Wójs (1998). The latter work also provides a comprehensive review on studies of excitons in quantum dots.

B. Coulomb blockade

Electron transport through a quantum dot is studied by connecting the quantum dot to surrounding reservoirs. The fact that the charge on the electron island is quantized in units of the elementary charge e regulates transport through the quantum dot in the Coulomb blockade regime (Kouwenhoven and McEuen, 1999). Here the transport between the reservoirs and the dot occurs via tunnel barriers, which are thick enough that the transport is dominated by resonances due to quantum confinement in the dot (Tanaka and Akera, 1996). This requires a small transmission coefficient through the barriers, and thus the tunnel resistance has to be larger than the quantum resistance h/e^2. If the dot is fully decoupled from its environment, it confines a well-defined number N of electrons. For weak coupling, deviations due to tunneling through the barriers are small, leading to discrete values in the total electrostatic energy of the dot. This energy can be estimated by $N(N-1)e^2/(2C)$, where C is the capacitance of the dot. Thus the addition of a single electron requires energy Ne^2/C, which is discretely spaced by the charging energy e^2/C. If this charging energy exceeds the thermal

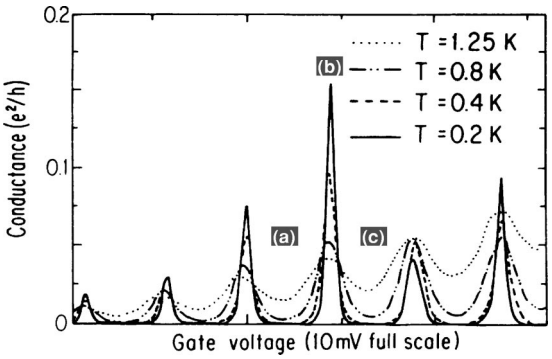

FIG. 6. An example of the first measurements of Coulomb blockade as a function of the gate voltage, observed for a laterally confined narrow channel. The figure is taken from Meir, Wingreen, and Lee, 1991 and goes back to the experimental work of Meirav, Kastner, and Wind, 1990. (a),(c) regions of Coulomb blockade; (b) conductance region, as schematically illustrated in Fig. 7.

energy $k_B T$, the electrons cannot tunnel on and off the dot by thermal excitations alone, and transport can be blocked, which is referred to as a *Coulomb blockade* (Averin and Likharev, 1986, 1991; Grabert and Devoret, 1991; see also Kouwenhoven, Marcus, *et al.*, 1997, Kouwenhoven, Oosterkamp, *et al.*, 1997, and Kouwenhoven and McEuen, 1999).

Single-electron charging effects in electron tunneling were first studied by transport measurements on thin films of small metallic grains (Gorter, 1951; Giaever and Zeller, 1968; Lambe and Jaklevic, 1969; Zeller and Giaever, 1969). In 1975, Kulik and Shekter pointed out that in a double-junction system, the current through a small grain at low bias voltages is blocked by the charge on the island, whereas the differential conductance can vary periodically at a higher bias. The Coulomb blockade and the Coulomb "staircase" were observed by Kuzmin and Likharev (1987) and by Fulton and Dolan (1987) for granular systems and thin-film tunnel junctions, respectively. Single-electron charging effects were further investigated for one-dimensional arrays of ultrasmall tunnel junctions by Kuzmin *et al.* (1989) and Delsing *et al.* (1989a, 1989b). Scott-Thomas *et al.* (1989) found periodic variations in the conductance of a narrow disordered channel in a Si inversion layer, for which van Houten and Beenakker (1989) suggested an interpretation in terms of single-electron charging effects. Their explanation was based on the assumption that charged impurities along the narrow channel would form a partially isolated segment, and the conductance oscillations should arise from its sequential, quantized charging. Groshev (1990) argued that the experiment by Reed *et al.* (1988) mentioned above can be better understood by taking Coulomb charging effects into account. To be able to observe the conductance oscillations in a more controlled way, Meirav, Kastner, and Wind (1990) suggested the construction of a narrow channel by a lithographically defined gate structure, as shown in Fig. 5. The two barriers define the coupling of the channel to its surroundings. Figure 6 shows the result of the experiment, in which the conductance of the double-barrier channel was measured as a function of the gate voltage at different temperatures (see also Meir, Wingreen, and Lee, 1991). One can see how the Coulomb blockade affects transport: clear peaks, equidistantly spaced, are separated by regions of zero conductance. For an early review on conductance oscillations and the related Coulomb blockade, see Kastner, 1992.

The possibility of forming quantum dots by gates on a heterostructure was later used by many different groups, and measurements of Coulomb blockade spectra for dots of various sizes and geometries were analyzed. We restrict our discussion here to the most elementary arguments needed to understand the basic features in the experimental spectra and—for the sake of simplicity—discuss the Coulomb blockade mechanism only on a qualitative level. For a more thorough analysis, see, for example, Meir, Wingreen, and Lee (1991) and the recent review by Aleiner, Brouwer, and Glazman (2001) on quantum effects in Coulomb blockade.

Following Kouwenhoven and McEuen (1999), the upper panel of Fig. 7 schematically illustrates an electron island connected to its environment by electrostatic barriers, the so-called *source* and *drain* contacts, and a gate to which one can apply a voltage V_g. (In this example, the quantum dot is formed by the positively charged back gate, in contrast to Fig. 5, where negatively charged gates surrounded a region in which the dot is formed.)

The level structure of the quantum dot connected to source and drain by tunneling barriers is sketched schematically in Figs. 7(a)–(c). The chemical potential inside the dot, where the discrete quantum states are filled with N electrons [i.e., the highest solid line in Figs. 7(a)–(c)], equals $\mu_{\rm dot}(N)=E(N)-E(N-1)$, where $E(N)$ is the total ground-state energy (here at zero temperature). When a dc bias voltage is applied to the source s and the drain d, the electrochemical potentials μ_s and μ_d are different, and a *transport window* $\mu_s-\mu_d=-eV_{sd}$ opens up. In the linear regime the transport window $-eV_{sd}$ is smaller than the spacing of the quantum states, and only the ground state of the dot can contribute to the conductance. By changing the voltage on the back gate, one can achieve an alignment of $\mu_{\rm dot}(N+1)$ with the transport window [Fig. 7(b)], and electrons can subsequently tunnel on and off the island at this particular gate voltage. This situation corresponds to a conductance maximum, as marked by the label (b) in Fig. 6. Otherwise transport is blocked, as a finite energy is needed to overcome the charging energy. This scenario corresponds to zero conductance as marked by the labels (a) and (c) in Fig. 6. The mechanism of discrete charging and discharging of the dot leads to Coulomb blockade oscillations in the conductance as a function of gate voltage (as observed, for example, in Fig. 6): at zero conductance, the number of electrons on the dot is fixed, whereas it is increased by one each time a conductance maximum is crossed. (If the gate voltage is fixed but the source-drain voltage is varied instead, the current-voltage characteristic shows current steps occurring at integer multiples of the

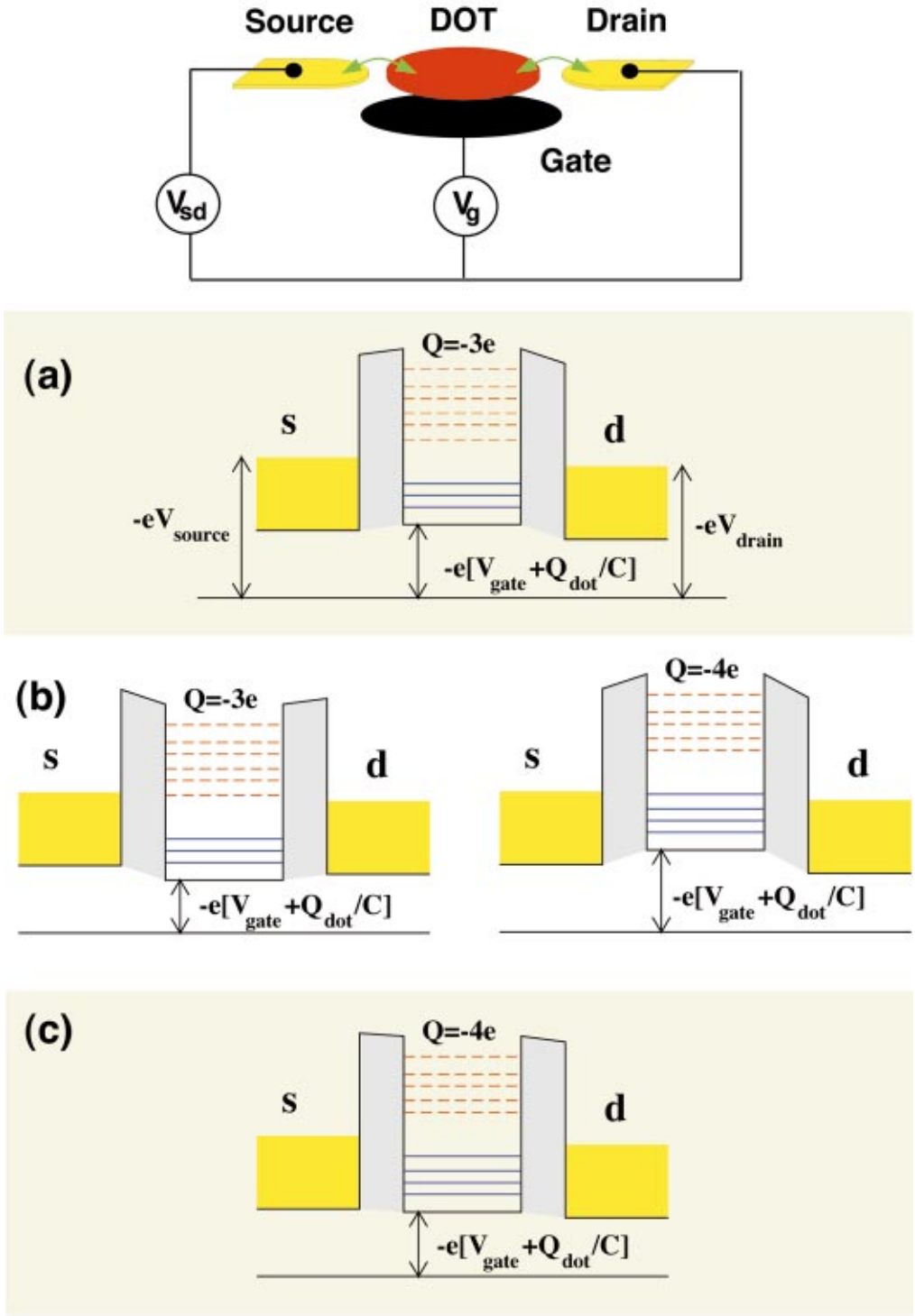

FIG. 7. Single-electron transport in a quantum dot: upper panel, setup for transport measurements on a lateral quantum dot, after Kouwenhoven and McEuen (1999); lower panel, (a)–(c) schematic picture of the level structures for single-electron transport (courtesy of A. Wacker). The solid lines represent the ionization potentials where the upper equals $\mu_{\rm dot}(N)$, whereas the dashed lines refer to electron affinities, where the lowest one equals $\mu_{\rm dot}(N+1)$. The gate bias increases from (a) to (c) [Color].

single-electron charging energy threshold; see, for example, Kouwenhoven *et al.*, 1991.)

The distance between neighboring Coulomb peaks is the difference between the (negative) ionization potential $I(N)=E(N-1)-E(N)$ and the electron affinity $A(N)=E(N)-E(N+1)$ of the artificial atom (Kastner, 1993). It equals the difference in the electrochemical potentials of a dot confining $N+1$ and N electrons, i.e., the second differences of the corresponding total ground-state energies $E(N)$:

$$\Delta_2(N)=\mu_{\rm dot}(N+1)-\mu_{\rm dot}(N)$$
$$=E(N+1)-2E(N)+E(N-1). \quad (3)$$

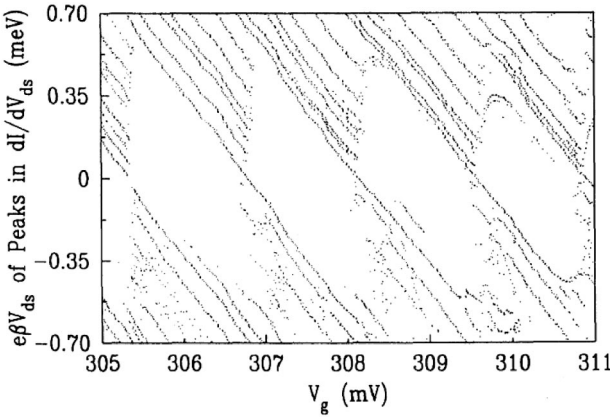

FIG. 8. Peak positions in the differential conductance $dI/dV_{\rm sd}$ as a function of $V_{\rm sd}$ (converted to an energy by some factor $e\beta$) and gate voltage (see Foxman *et al.*, 1993) for a quantum dot structure as shown in Fig. 5 above.

Following Kouwenhoven *et al.* (1991; Kouwenhoven and McEuen, 1999), in the simple, *constant-capacitance model* (Silsbee and Ashoori, 1990; McEuen *et al.*, 1991, 1992) it is assumed that the difference between the chemical potential of a dot confining N or $N+1$ electrons can be approximated by the differences of the single-particle energies $\Delta\varepsilon=\varepsilon_{N+1}-\varepsilon_N$, plus the single-electron charging energy e^2/C:

$$\Delta_2(N)\approx\Delta\varepsilon+e^2/C. \tag{4}$$

As the capacitance of the dot increases and thus leads to a reduced charging energy, the *addition energy* (the energy required to add an electron to the system) decreases with increasing number of confined electrons. From Eq. (4) we see that when $e^2/C\gg k_BT\gg\Delta\varepsilon$, quantum effects can be neglected, and the Coulomb blockade oscillations are periodic in e^2/C. (This, for example, was the case for the Coulomb oscillations shown in Fig. 6, measured for a fairly large sample in the mesoscopic regime.)

For a larger transport window $-eV_{\rm sd}$, i.e., in the nonlinear transport regime, additional structures in the Coulomb blockade occur: the excitation spectrum leads to a set of discrete peaks in the differential conductance $dI/dV_{\rm sd}$ (Johnson *et al.*, 1992; Wies *et al.*, 1992, 1993; Foxman *et al.*, 1993). Plotting the positions of these peaks as a function of $V_{\rm sd}$ and the gate voltage, one observes a characteristic diamond-shaped structure, which reveals information about the ground and excited states; see Fig. 8. (The details of these structures depend on the particular experimental setup; a further description is given, for example, by Kouwenhoven, Marcus, *et al.*, 1997 and Kouwenhoven and McEuen, 1999.) In the linear regime, i.e., $V_{\rm sd}\approx 0$, we observe Coulomb blockade as described above. Upon increasing $V_{\rm sd}$, excited states (though usually only a few low-lying ones) become accessible and additional transport channels are provided (see Fig. 7). The vertical gap (Fig. 8) reflects the charging energy causing the Coulomb blockade. Between successive diamonds touching at the $V_{\rm sd}=0$ axis, the electron number increases from N to $N+1$. Similar observations were reported on vertical quantum dot structures, which allowed a more detailed analysis of the ground and excited states in magnetic fields (see Kouwenhoven, Oosterkamp, *et al.*, 1997, and Sec. VI).

Studying the ground and excited spectra of a quantum dot by linear and nonlinear magnetoconductance measurements, Stewart *et al.* (1997) demonstrated that strong correlations exist between the quantum dot energy-level spectra of successive electron numbers in the dot. They observed a direct correlation between the ith excited state of an N-electron system and the ground state of the $(N+i)$-electron system for $i\lesssim 4$. This was surprising, as a notable absence of spin degeneracy and deviations from the simple single-particle picture are expected due to the interactions of the particles.

C. Probes of single-electron charging

For metallic systems, signatures of quantum effects in the Coulomb blockade spectra were discussed at an early stage by Korotkov *et al.* (1990), Averin and Likharev (1991), Beenakker (1991), and Meir *et al.* (1991). More recent experiments were performed on ultrasmall and very clean metallic nanoparticles (Ralph, Black, and Tinkham, 1997; Davidović and Tinkham, 1999). For a recent review, see von Delft and Ralph, (2001).

For semiconductor quantum dots, different experimental techniques for probing single-electron charging effects on single dots or arrays of dots have been applied, allowing a detailed spectroscopic study of the ground and excited states of individual artificial atoms. Infrared and optical spectroscopy was reported for arrays of quantum dots (Sikorski and Merkt, 1989; Bawendi, Steigerwald, and Brus, 1990; Meurer, Heitmann, and Ploog, 1992). Brunner *et al.* (1992) were among the first to apply optical spectroscopy to individual dots. The first capacitance measurements of quantum dots were reported by Smith *et al.* (1988). Single-electron capacitance spectroscopy has been applied both to arrays (Hansen *et al.*, 1989; Silsbee and Ashoori, 1990; Ashoori, Silsbee, *et al.*, 1992) and to individual quantum dots (Ashoori, Stormer, *et al.*, 1992).

From a microscopic approach to electron tunneling through a quantum dot based on a Hartree-Fock calculation, Wang, Zhang, and Bishop (1994) inferred that, for a small number of electrons, the Coulomb oscillations are nonperiodic and become periodic only in the large-N limit. Such irregularities in the single-electron transport spectra of quantum dots were observed experimentally rather early (see Ashoori *et al.*, 1993, and Schmidt *et al.*, 1995). However, sample-dependent inhomogeneities probably inhibited a very clear observation of shell structure in these pioneering experiments. For gated vertical-dot structures, Tarucha *et al.* (1995, 1996) and Austing *et al.* (1996) were the first to demonstrate very clearly the electronic shell structure of small vertical dots.

The methods of gated transport spectroscopy, single-electron capacitance spectroscopy, and single-electron transport through a vertical quantum dot are briefly treated in what follows, before we turn to a theoretical analysis of the electronic structure of quantum dots. Many of the experimental data can be well understood within a model that assumes the quantum dot to be isolated from its environment.

1. Gated transport spectroscopy

A measurement of the Coulomb blockade peaks as a function of gate voltage for a lateral gate structure was shown in Fig. 6 above. As this dot was rather large, quantization effects were negligible and the Coulomb blockade peaks were equidistant. The sensitivity of "gated transport spectroscopy" (Ashoori, 1996) on Coulomb blockade and quantum level splittings was demonstrated by McEuen *et al.* (1991, 1992) for systems confining $\sim$100 electrons. For transport measurements on small lateral quantum dots in both the linear and the nonlinear regime, Johnson *et al.* (1992) observed a combined effect of zero-dimensional quantum states and single-electron charging. Oscillations in the conductance measured on a lateral gated quantum dot with circular shape, formed electrostatically by gates on top of a GaAs-AlGaAs heterostructure, were later reported by Persson *et al.* (1994), Persson, Lindelof, *et al.* (1995), and Persson, Petterson, *et al.* (1995). Here the dot was fairly large, confining between about 600 and 1000 electrons. While the discreteness of the quantum states could not be observed directly from the measurements, the pronounced oscillations in the conductance could be related to regular shell patterns in the quantum density of states, modeled by a simple single-particle model for a circular disk confinement with ideally reflecting walls. A semiclassical interpretation of these experiments in terms of periodic orbits was suggested by Reimann *et al.* (1996; see also Brack and Bhaduri, 1997). For metallic clusters, a similar analysis had been performed earlier by Nishioka, Hansen, and Mottelson (1990). They predicted a *supershell structure*, as we briefly mentioned in the Introduction: a beating pattern in the density of states is superposed on the individual shell oscillations (Balian and Bloch, 1970, 1971, 1972). Such a supershell structure was experimentally discovered in mass abundance spectra of metallic clusters (Pedersen *et al.*, 1991), but has not yet been observed in two-dimensional quantum dot systems (Bøggild *et al.*, 1998).

If the Fermi wavelength is small compared to both the device dimensions and the phase coherence length, and if the mean free path exceeds the dot size, the electron motion in the dot becomes ballistic. Such dots can be treated like electron billiards, where the electrons move as classical particles but do carry phase information. Interference effects of trajectories scattered from the confining walls of microstructures with irregularly shaped boundaries have been compared to disordered materials, in which the electron motion is diffusive and quantum interference adds to the classical conductance. These studies of mesoscopic transport, quantum interference, and classically chaotic systems constitute a large field of research in themselves. We refer the reader to Beenakker and van Houten (1991) and Altshuler, Lee, and Webb (1991) for reviews of mesoscopic phenomena in semiconductor nanostructures. The recent review by Alhassid (2000) discusses statistical theories in the mesoscopic regime. A description of chaos in ballistic nanostructures was further provided by Baranger and Westervelt (1998).

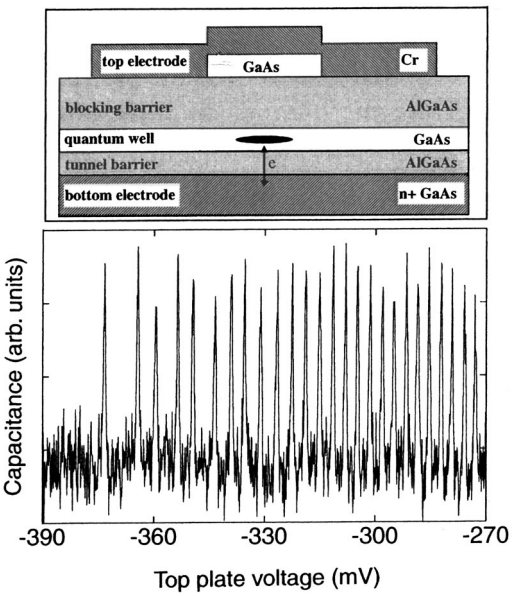

FIG. 9. Single-electron capacitance spectroscopy. Upper panel, scheme of the quantum dot device used in single-electron capacitance measurements by Ashoori, Störmer, *et al.* (1992), Ashoori *et al.* (1993), and Ashoori (1996). The arrow indicates the tunneling of an electron back and forth between the dot and the bottom electrode in response to a (periodic) voltage applied to the top gate. Lower panel, capacitance measured as a function of the gate voltage V_g. From Ashoori, 1996.

Large electron numbers are rather typical for lateral quantum dot structures: it is very difficult to decrease the number of confined electrons to below about 20 (Kouwenhoven, Marcus, *et al.*, 1997), as the tunnel barriers formed by the depletion potential become too large for observation of a current. Progress was made only recently, when Ciorga *et al.* (2000) demonstrated that by designing specially formed gates on a GaAs-AlGaAs heterostructure, one can create lateral quantum dots even in the few-electron regime.

2. Single-electron capacitance spectroscopy

Ashoori, Störmer, *et al.* (1992), and Ashoori *et al.* (1993) applied capacitance spectroscopy to a GaAs tunnel capacitor containing a microscopic region for charge accumulation (see Fig. 9, upper panel) in which the charge could be varied from zero to thousands of electrons. The structure consisted of a thin AlGaAs layer (forming a tunnel barrier), followed by a layer of GaAs forming the quantum well, and a thick layer of AlGaAs

that acted as an insulator, prohibiting the tunneling of electrons to the top electrode. A circular GaAs disk was grown on top of this AlGaAs layer, right above the quantum well, and the wafer was covered with a top electrode. This capacitor was shaped so that when a gate voltage was applied, electrons were confined in the GaAs quantum well. The quantum dot formed between the two electrodes (top and bottom) was close enough to the bottom electrode that single electrons could tunnel on and off. Single-electron capacitance spectroscopy measures the capacitance signal due to the tunneling of a single electron into the dot, which induces charge on the top electrode. Detection of this charge makes it possible to accurately determine the gate voltage at which a single electron can enter the dot.

Figure 9 shows a plot of the capacitance versus gate bias. With increasing positive bias on the top plate, electrons tunnel subsequently into the dot. The spacing between the peaks is approximately constant, similar to what was observed by Meirav, Kastner, and Wind (1990) for larger, lateral quantum dots. For smaller bias, however, the data of Ashoori, Störmer, *et al.* (1992) and Ashoori *et al.* (1993) show irregularities: the distances between subsequent peaks are increased and are nonuniform. These deviations from the equidistant Coulomb blockade spectra can be attributed to energy quantization in the dot structure, as we shall explain later.

3. Transport through a vertical quantum dot

Despite the early success in obtaining very clear Coulomb blockade spectra (Kastner, 1992), for a rather long time it remained a challenge to fabricate dots so regular and clean that clear signals of energy quantization and shell structure in the small-N limit could be observed.

In vertical dots (as already described briefly in Secs. I.B and II.A above) one uses thin heterostructure barriers that are only very weakly affected by the gate potential. Such dots were the most promising candidates for achieving a truly quantum-mechanical confinement of a small number of electrons. Their fabrication, however, is difficult, and until about 1996, transport measurements on such structures were reported by only a few groups (Reed *et al.*, 1988; Dellow *et al.*, 1991; Goodings *et al.*, 1992; Guéret *et al.*, 1992; Kolagunta *et al.*, 1995). Tarucha *et al.* (1996) worked with a gated vertical quantum dot structure (as schematically shown earlier in the inset to Fig. 3, lower right panel). The quantum dot was made from a double-barrier heterostructure by etching techniques, and the electron puddle was located between two heterostructure barriers that separated it from the outside environment. A metallic Schottky gate was wrapped around the circular etched pillar close to the dot region. Tunnel junctions allowed Tarucha *et al.* to vary the electron number N by applying a negative voltage V_g to the Schottky gate. The energy gap between conductance and valence band could be reduced by includingly indium in the well. The bottom of the conduction band was then below the Fermi level of the contacts, i.e., electrons could accumulate in the dot even

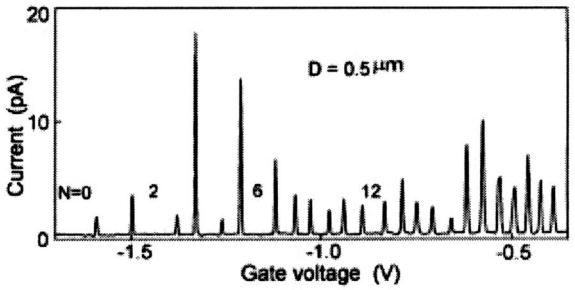

FIG. 10. Coulomb blockade oscillations in the linear regime as a function of gate voltage, measured on the vertical gated quantum dot structure by Tarucha *et al.* (1996). The quantum dot is estimated to have a diameter of 0.5 μm. The measurement was performed at 50 mK.

if no voltage was applied. This made it possible to study electron transport even at very small bias voltages. The gate changed the effective diameter of the island. In the experiment, the current flowed vertically through the dot in response to a small dc voltage applied between the contacts (i.e., in the linear transport regime as sketched in Fig. 7). By measuring this conductance as a function of the gate voltage V_g, Tarucha *et al.* (1996) could observe clear Coulomb oscillations, corresponding to a one-by-one increase in the number of confined electrons in the dot each time a Coulomb blockade peak was crossed. The period of the Coulomb peaks showed a very pronounced N dependence: the spacings between the second and third, sixth and seventh, and twelfth and thirteenth peaks were larger than the spacings between the neighboring peaks (Fig. 10). This becomes even more clear when looking at the addition energy differences $\Delta_2(N)$, which are proportional to the spacings between the Coulomb blockade peaks, as shown in Fig. 3. [Note that Tarucha *et al.* (1996) used a scaling factor for converting gate voltages to energies.] Pronounced maxima at $N=2$, 6, and 12 can be seen in $\Delta_2(N)$ for devices with a diameter of 0.5 and 0.44 μm.

The vertical quantum dot structure has a diameter that is about ten times larger than its thickness in the vertical direction. To a good approximation one can assume that the motion of the electrons in the z direction is frozen, i.e., only the ground state is occupied, and the dot can be well approximated by a smoothly confined circular electron island in two dimensions (x,y). It is obvious that the maxima in the spacings of the conductance peaks or in the addition energy differences $\Delta_2(N)$ are related to shell structure. In fact, the numbers coincide with the lowest closed shells of the two-dimensional harmonic oscillator confinement in the isotropic case, $N=2,6,12,\ldots$ (see Fig. 2 for $\delta=1$). Keeping in mind the discussion of atomic ionization spectra, we should furthermore expect that as a consequence of Hund's rules the pronounced structures at the midshell regions are related to spin alignment. These issues are discussed in the next section.

III. ADDITION ENERGY SPECTRA

The independent-particle model provides an intuitive understanding of the shell structure. At low electron

densities or in strong magnetic fields, however, one should turn to more sophisticated models for an accurate description.

Hartree-Fock calculations give a first estimate of exchange effects. The correlation energy can be included within density-functional theory (DFT), while keeping the description on a mean-field level. This restriction can be overcome by numerical, "exact" diagonalization of the many-body Hamiltonian (the *configuration-interaction method*), in which one must necessarily restrict the Hilbert space to a finite basis (i.e., the "exact" method is not truly exact), or by quantum Monte Carlo methods. All these methods have been applied to a variety of different systems such as circular or deformed quantum dots, rings, and quantum wires.

After some general remarks in Sec. III.A, we turn to a brief discussion of spin-density-functional theory in Sec. III.B. Most authors consider a parabolic confinement for the external quantum dot potential, which is explained in Sec. III.C. After setting the stage, results for addition energy spectra and spin configurations in quantum dots are discussed in Secs. III.D, III.H, and III.I; these results can be directly related to the experimental results addressed in the previous section.

A. Many-body effects in quantum dots

The electrons in the quantum dot belong to the conduction band of the semiconductor. The conduction-electron density is low, the mean electron-electron distance being of the order of 10 nm. Consequently effects due to the underlying lattice and to interaction with the valence and core electrons can be taken into account using the effective-mass approximation: the conduction electrons in the quantum dot form a separate interacting electron system with an effective mass m^*, and their mutual Coulomb interaction is screened with the static dielectric constant of the semiconductor in question.

The many-body Hamiltonian H of a quantum dot, decoupled from its environment, is usually written as the sum of a single-particle part (kinetic and potential contributions) and the two-body part, describing the Coulomb interaction between the electrons confined in the dot:

$$H=\sum_{i=1}^{N}\left(\frac{\mathbf{p}_i^2}{2m^*}+V(\mathbf{r_i})\right)+\sum_{i<j}^{N}\frac{e^2}{4\pi\epsilon\epsilon_0|\mathbf{r}_i-\mathbf{r}_j|}. \tag{5}$$

Here, m^* is the effective electron mass and ϵ is the dielectric constant of the corresponding background material. [The energy and length units are frequently given in effective atomic units, with the effective rydberg $\mathrm{Ry}^*=m^*e^4/2\hbar^2(4\pi\epsilon\epsilon_0)^2$ or hartree $\mathrm{Ha}^*=2\ \mathrm{Ry}^*$ and the effective Bohr radius $a_B^*=\hbar^2(4\pi\epsilon\epsilon_0)/m^*e^2$, as this allows a scaling to the actual values for typical semiconductor materials. For GaAs, $a_B^*=9.8$ nm and $\mathrm{Ry}^*=6$ meV.]

Interacting electrons confined in a two-dimensional harmonic trap form a seemingly simple many-body problem: if the number of electrons is not too large, standard methods can be applied. Bryant (1987) was the first to point out the importance of electron correlations that give rise to many intriguing properties of quantum dots. For a two-electron system in a long and narrow rectangular box, he studied theoretically the continuous evolution from single-particle-level structure to a regime in which the electron-electron interactions dominate and a Wigner crystal can form (see also Sec. IV.A). A quantum dot confining two electrons (the so-called *quantum dot helium*; Pfannkuche, Gerhardts, *et al.*, 1993) is the simplest example for which the eigenstates and spectra of the two-particle Schrödinger equation can be obtained analytically (Taut, 1994; see also El-Said, 1996; González, Quiroga, and Rodriguez, 1996; Dineykhan and Nazmitdinov, 1997). For realistic interactions like the Coulomb repulsion, analytic solutions for $N>2$ are impossible to obtain. Only for some modified forms of the interparticle interaction, which, however, are of more academic interest, have exact analytic solutions been obtained; see, for example, Johnson and Payne, 1991; Quiroga, Ardila, and Johnson, 1993; Johnson and Quiroga, 1994, 1995.)

The traditional way to attack a correlated few-electron problem (Bryant, 1987; Maksym and Chakraborty, 1990; Pfannkuche, Gerhardts, *et al.*, 1993, Pfannkuche, Gudmundsson, *et al.*, 1993) is to apply configuration-interaction methods, which are also frequently used in quantum chemistry. (For a detailed description of the exact diagonalization method for quantum dots, see Chakraborty, 1999.) In many cases, however, we have to face the drawback that numerical diagonalization methods are applicable only to fairly small numbers of electrons at not too low densities. If enough configurations, i.e., linear combinations of Slater determinants made up from the single-particle basis states, are included in the calculation, the solution converges to the exact result and both ground and low-lying excited states are obtained with rather high accuracy. The advantage of exact diagonalization methods is that, in addition to the ground-state energy and wave function, all low-lying excitations are computed with essentially no extra cost or reduction of accuracy. This is important, since the excitation spectrum can also provide insight into the electronic structure of the ground state. On the experimental side, transport spectroscopy can be used to identify the quantum numbers of excited states and offers a direct link between theory and experiment (Kouwenhoven, Oosterkamp, *et al.*, 1997; see Sec. VI.A).

Configuration-interaction calculations have been particularly useful for a description of dots in strong magnetic fields (see Sec. VI), where restrictions of Hilbert space allow us to obtain accurate results for dots confining up to about ten electrons (Maksym and Chakraborty, 1990; Hawrylak and Pfannkuche, 1993; Pfannkuche, Gudmundsson, and Maksym, 1993; Yang, MacDonald, and Johnson, 1993; Palacios *et al.*, 1994).

An alternative to the configuration-interaction method is the use of quantum Monte Carlo calculations, which have been performed for quantum dots in magnetic fields [see Bolton, 1994a, 1994b (fixed-node quantum Monte Carlo), Harju *et al.*, 1999, and Pederiva, Um-

rigar, and Lipparini, 2000 (diffusion quantum Monte Carlo)] as well as in the low-density regime [see Egger *et al.*, 1999 (variational quantum Monte Carlo) and Secs. VI.A and IV.E].

B. Density-functional method

The mean-field approach offers considerable simplification: it models a many-body system by noninteracting particles confined in an average potential into which the interactions are incorporated. To study large electron systems in the presence of correlations, density-functional theory in the self-consistent formulation of Kohn and Sham (1965) provides a particularly powerful tool. (For reviews see, for example, Jones and Gunnarsson, 1989; Dreizler and Gross, 1990; Gross, Runge, and Heinonen, 1991.) Density-functional theory is based on the theorem by Hohenberg and Kohn (1964) and its generalization by Levy (1979): the exact ground-state energy of a many-body system is a unique functional of the electron density $n(\mathbf{r})$. Its variation with respect to the density yields an absolute energy minimum for the true-ground state density. Initially, DFT was developed in a spin-independent formalism. Effects of spin polarization (as they can occur in open-shell atoms or systems with broken spin symmetry, such as ferromagnets) were later incorporated by von Barth and Hedin (1972). This so-called spin-density-functional theory (SDFT) relies on the assumption that orbital currents give only a neglible contribution to the energy functional. A further extension of the theory to include gauge fields was later formulated by Vignale and Rasolt (1987, 1988) and became known as the current-spin-density-functional theory (CSDFT). This method, which was frequently applied to the description of artificial atoms in magnetic fields, is further described in Sec. VII.

In SDFT, the total energy is a functional of the spin-up and spin-down densities $n_\sigma(\mathbf{r})$, where $\sigma=(\uparrow,\downarrow)$ labels the spin. Equivalently, we can use the total density $n(\mathbf{r})=n_\uparrow(\mathbf{r})+n_\downarrow(\mathbf{r})$ and the spin polarization $\zeta(\mathbf{r})=[n_\uparrow(\mathbf{r})-n_\downarrow(\mathbf{r})]/n(\mathbf{r})$. By minimizing this functional one obtains the well-known Kohn-Sham equations,

$$\left(-\frac{\hbar^2}{2m^*}\nabla^2+V_{KS,\sigma}[n,\zeta]\right)\phi_{i,\sigma}(\mathbf{r})=\epsilon_{i,\sigma}\phi_{i,\sigma}(\mathbf{r}), \tag{6}$$

with the effective potential

$$V_{KS,\sigma}[n,\zeta]=V(\mathbf{r})+\frac{e^2}{4\pi\varepsilon_0\varepsilon}\times\int d\mathbf{r}'\frac{n(\mathbf{r}')}{|\mathbf{r}-\mathbf{r}'|}+\frac{\delta E_{xc}[n,\zeta]}{\delta n_\sigma(\mathbf{r})} \tag{7}$$

consisting of the external potential, the Hartree contribution, and the variational derivative of the exchange-correlation energy. Because the mean-field potential V_{KS} depends on the single-particle wave functions or densities, the equations have to be solved self-consistently by iteration. For a finite system with nonuniform density $n(\mathbf{r})$ one often makes the assumption that locally, the exchange-correlation energy per particle can be approximated by that of the corresponding infinite system at constant density. We label this energy by $e_{xc}(n(\mathbf{r}),\zeta(\mathbf{r}))$ and write

$$E_{xc}^{LSDA}[n,\zeta]=\int d\mathbf{r}\ n(\mathbf{r})e_{xc}(n(\mathbf{r}),\zeta(\mathbf{r})). \tag{8}$$

[The most frequently used parametrizations of e_{xc} in the local spin-density approximation (LSDA) are discussed, for example, by Dreizler and Gross (1990).] For the two-dimensional electron gas, Tanatar and Ceperley (1989) provided a parametrized form of e_{xc} as a Padé form for nonpolarized ($\zeta=0$) and ferromagnetic ($\zeta=1$) cases, obtained by a fit to a small set of numerical Monte Carlo data for a few discrete values of the electron density. For intermediate polarizations, a standard practice is the *ad hoc* assumption that the unknown polarization dependence of the correlation energy can be adopted from the analytical expression for the exchange energy. [This approach has been implemented for the electron gas in three dimensions by von Barth and Hedin (1972) and Perdew and Zunger (1981).] For the interpolation, one writes

$$e_{xc}(n,\zeta)=e_{xc}(n,0)+f(\zeta)[e_{xc}(n,1)-e_{xc}(n,0)], \tag{9}$$

with the polarization dependence (in the two-dimensional case)

$$f(\zeta)=\frac{(1+\zeta)^{3/2}+(1-\zeta)^{3/2}-2}{2^{3/2}-2}. \tag{10}$$

It should be emphasized that the mean-field equations given in Eq. (6) in principle need to be solved in a geometrically unrestricted scheme, i.e., the symmetry of the solution should not be constrained by the symmetry of the confinement. In the quantum dot literature, many authors choose to simplify the solution of the Kohn-Sham equations by imposing axial symmetry. We refer to this scheme in the following discussion as the restricted (spin) density-functional approach. A more general solution requires unrestricted symmetries in both the spatial and the spin parts of the single-particle wave functions. We shall return to this point later when discussing the broken-symmetry ground states in the mean-field description. We note that the degree to which the restricted DFT scheme gives a reliable approximation to the exact ground-state energies and densities depends on the average electron density in the dot. In two dimensions for high densities n, i.e., small values of the Wigner-Seitz parameter $r_s=1/\sqrt{\pi n}$, the single-particle part of the Hamiltonian Eq. (5) dominates over the interactions. In this case, the solutions of the restricted DFT scheme compare well with those found in the unrestricted approach. Broken-symmetry solutions originating from spatial deformation of the mean field occur for larger values of r_s, i.e., in the correlated regime. Here, the energies usually are lower than those of the symmetry-restricted DFT approach, reflecting the gain in correlation energy.

From the Hohenberg-Kohn theorem we know that the ground state is characterized by the single-particle ground-state density n, which can be determined varia-

tionally by minimizing the total energy functional. This argument applies to the lowest state of a given symmetry (Gunnarsson and Lundqvist, 1976). Starting the self-consistent iterations of the Kohn-Sham equations with different initial configurations in general leads to a set of converged solutions out of which we have to identify the true ground state. (Note that in order to achieve a reliable scan of the potential-energy surface, it is essential to start with a rather large set of initial conditions.) The addition energy differences $\Delta_2(N)$ are then computed from the Kohn-Sham ground-state energies after Eq. (3). In this connection, it is useful to note that Koopmans's theorem (Koopmans, 1933) connects the negative of the ionization energy with the highest occupied single-particle level. This theorem was originally formulated for the Hartree-Fock approximation and was later generalized to density-functional theory by Schulte (1974, 1977) and Janak (1978).

Capelle and Vignale (2001) have recently shown that in the spin-dependent formalism the effective potentials are not always unique functionals of the spin densities. While this notion is important for many applications of SDFT, it does not invalidate the use of LSDA as an approximate method for calculating ground-state properties using local approximations based on the homogeneous electron gas.

The time-dependent version of DFT can be used to study collective excitations. For applications to quantum dots, see, for example the work by Serra and Lipparini (1997), Serra *et al.* (1998, 1999), Lipparini and Serra (1998), and Ullrich and Vignale (2000).

C. Parabolic confinement

Kumar, Laux, and Stern (1990) determined the effective single-particle confinement for a square-shaped quantum dot of the type shown in Fig. 5 in a self-consistent Hartree approach, where the electrostatic confinement was incorporated by a self-consistent solution of the combined Hartree and Poisson equations. They found that in the limit of small particle numbers, the effective confinement can have a symmetry very close to circular, even if the confinement was formed by a square-shaped metallic gate pattern. On the basis of their work, the simple isotropic harmonic oscillator was adopted as the standard quantum dot model potential for electronic structure calculations, in both exact diagonalization studies and mean-field approaches. We used this model above when we identified oscillatorlike shell structure and magic numbers in the addition energy spectra (see Sec. I.A).

In many cases, measurements of far-infrared absorption spectra on ensembles of quantum dots (see, for example, Sikorski and Merkt, 1989; Demel *et al.*, 1990; Lorke, Kotthaus, and Ploog, 1990; Meurer, Heitmann, and Ploog, 1992) correspond to those of a noninteracting system. In the view of the generalized Kohn theorem (Kohn, 1959, 1961; Brey *et al.*, 1989; Yip, 1991), this further supports the assumption of parabolic confinement: the center-of-mass motion separates out and the only possible dipole excitation is the center-of-mass excitation. Kohn's theorem implies that the effects of electron-electron interactions in a quantum dot can be observed by far-infrared spectroscopy only if the anharmonicity of the confinement is sufficiently strong (Gudmundsson and Gerhardts, 1991; Darnhofer and Rössler, 1993; Pfannkuche *et al.*, 1994; Gudmundsson, Braatas, *et al.*, 1995).

Much of the theoretical work modeling the addition energy spectra for small, parabolic quantum dots has been performed under the assumption that the finite thickness of a quantum dot, typically much smaller than the lateral extension of the electrostatic confinement, can be neglected. As a compromise between realistic simulation and numerical feasibility (Macucci, Hess, and Iafrate, 1993), one can separate the effective confinement into an in-plane and perpendicular part, $V=V(x,y)+V(z)$. With the assumption that in the z direction only the ground state is occupied, the solution can then be restricted to the (x,y) plane. For the 2D parabolic confinement $V(x,y)=\frac{1}{2}m\omega^2(x^2+y^2)$, if we keep the oscillator parameter ω constant, the electron density in the dot increases with N. Experimentally, however, if one makes the voltage on the (side or top) gates less negative, the effective confinement strength ω decreases. At the same time, the number of electrons in the dot increases. Thus we may also consider keeping the average electron density in the dot constant, i.e., fixing the density parameter r_s and varying ω with N. Indeed, for vertical dots it turns out that as N increases, the confinement weakens so that the particle density tends to a constant (Austing, Tokura, *et al.*, 1999). The average value of the electron-density parameter r_s for the circular quantum dot sample studied by Tarucha *et al.* (1996) is estimated to be between $1.3a_B^*$ and $1.4a_B^*$. This value is close to the equilibrium value of the two-dimensional electron gas, $r_s=1.5a_B^*$. For a constant average density the N dependence of the oscillator parameter ω can be approximated by

$$\omega^2=\frac{e^2}{4\pi\varepsilon_0\varepsilon m^* r_s^3\sqrt{N}} \tag{11}$$

(Koskinen *et al.*, 1997).

D. Addition energy spectra described by mean-field theory

Macucci, Hess, and Iafrate (1993, 1995) extended the work by Kumar, Laux, and Stern (1990), including the exchange and correlation contributions within density-functional theory. As a consequence of the degeneracies introduced by the symmetry of the dot confinement, they observed a shell-like grouping of the values of the chemical potentials $\mu(N)$. Extensive density-functional calculations were performed by Stopa (1993, 1996) for studying the Coulomb blockade in 2D dots containing 50–100 electrons. Fujito, Natori, and Yasunaga (1996) used an unrestricted Hartree-Fock approach to study both the effects of electron spin and the vertical extent

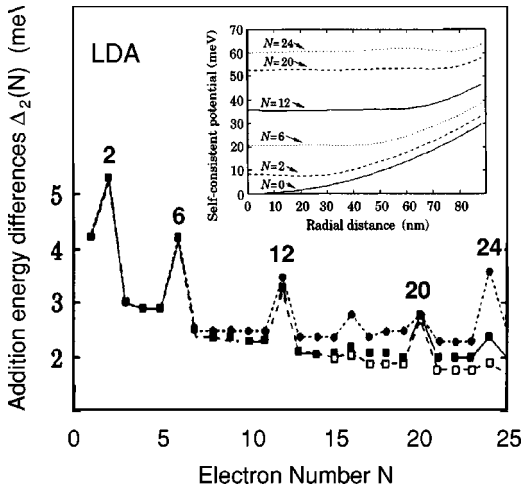

FIG. 11. Shell structure of a parabolic quantum dot with constant $\hbar\omega = 3$ meV in the dot center and hard walls at three radii: ●, $r > 75$ nm; ■, $r > 90$ nm; □, $r > 120$ nm. The inset shows the self-consistent potential of a quantum dot with a hard wall at $r = 90$ nm for different electron numbers. After Macucci *et al.*, 1997.

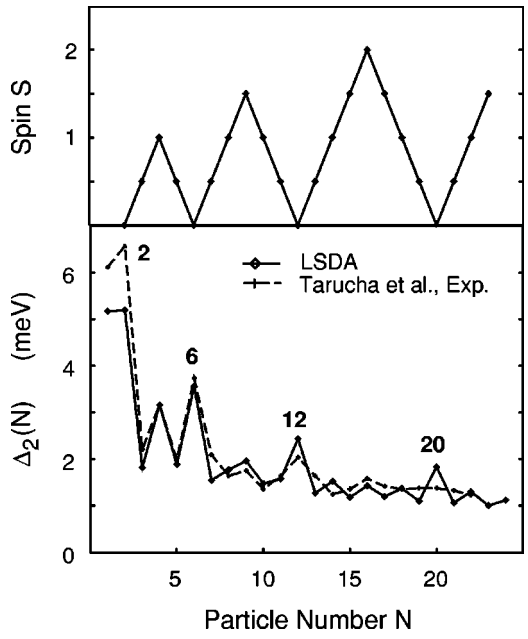

FIG. 12. Addition energies compared with experimental data: upper panel, ground-state spin S as a function of N. At closed shells $N = 2,6,12,20$, $S = 0$, while Hund's rule leads to maxima in S at midshell. Lower panel, addition energies $\Delta_2(N)$ as a function of the number N of electrons in a quantum dot with circular symmetry: solid line, energies obtained in spin-density-functional theory; dashed line, experimental results of Tarucha *et al.*, 1996. From Reimann, Koskinen, Kolehmainen, *et al.* (1999).

of the trapping potential. Oscillations in the dot capacitance caused by shell structure clearly demonstrated the occupation of single-particle levels in accordance with Hund's rules. The unrestricted Hartree-Fock method was also applied to a calculation of the addition energy spectra of cylindrical quantum dots by Szafran, Adamowski, and Bednarek (2000).

Macucci, Hess, and Iafrate (1997) determined the addition energy differences $\Delta_2(N)$ [see Eq. (3)] for 2D quantum dots confining up to 24 electrons. They worked in the symmetry-restricted DFT formalism and neglected the spin degree of freedom. Figure 11 shows the addition energy spectra obtained in the local-density approximation (LDA) for material parameters $m^* = 0.0648\, m_0$ (where m_0 is the bare electron mass) and $\epsilon = 12.98$. Macucci *et al.* assumed a parabolic confinement for dot radii $r \leqslant a$ and "hard walls" for $r > a$, where a is a maximum value for the quantum dot radius. As expected, pronounced maxima are seen for shell closings $N = 2$, 6, 12, (20), and 24. At fairly high electron densities the system very closely resembles the noninteracting one. As we saw above, a harmonic 2D oscillator filled with noninteracting particles has shells at $N = 2,6,12,20,30,\ldots$, while the spectrum of a 2D disk with hard walls shows major shell fillings for $N = 2,6,12,24,34,\ldots$ with weaker subshells at 16 and 20. In LDA, the spin-degenerate single-particle orbitals are occupied in pairs, following the Pauli principle. Consequently the addition energies do not show much structure in between the closed shells. We see a small hump at $N = 16$ and a more pronounced maximum at $N = 24$, the latter corresponding to a closed shell in hard-wall disk confinement. This change in the shell structure originates both from the hard-wall boundary conditions at larger radii and from the fact that the bottom of the effective self-consistent potential flattens with increasing number of electrons due to the effect of the Hartree term (see inset in Fig. 11).

Let us now proceed to include the spin degree of freedom in the local-density approximation in order to obtain a more accurate description of the midshell regions. For the spin polarization one usually applies the Barth-Hedin interpolation, Eqs. (9) and (10). To obtain the electron densities which minimize the total-energy functional $E[n_\uparrow, n_\downarrow]$, the Kohn-Sham equations Eq. (6) are then solved self-consistently. Koskinen *et al.* (1997) performed these calculations for 2D parabolic quantum dots in a symmetry-unrestricted approach. (Note that the energy differences to a symmetry-restricted solution can be significant. In the unrestricted scheme, a Fermi gap opens and the self-consistent energy is lowered with respect to the energy of the restricted solution with circular symmetry. However, if the electron density is relatively high, the differences in addition energy between the restricted and the unrestricted solutions are very small.)

Figure 12 shows the addition energy differences $\Delta_2(N)$ obtained from the Kohn-Sham ground-state energies $E(N)$ and compares them to the experimental data (Tarucha *et al.*, 1996) for a quantum dot with a diameter of about 0.5 μm. Here the oscillator confinement ω was taken to be N dependent [Eq. (11)], with the average electron density kept approximately constant at $r_s = 1.5 a_B^*$.

For closed-shell configurations with $N=2$, 6, and 12, a large energy gap between the highest occupied and the lowest unoccupied Kohn-Sham single-particle levels is found. The dot is nonmagnetic with "total" spin zero (which in Kohn-Sham theory implies that it has equal spin-up and spin-down electron densities). The systematic development of the total spin S is plotted in the upper panel of Fig. 12. Comparing the two panels, the fine structure at midshell (i.e., the peaks at $N=4$ and $N=9$) is clearly associated with maximized spin (Zeng, Goldmann, and Serota, 1993; Tarucha *et al.*, 1996; Hirose and Wingreen, 1999; Reimann, Koskinen, Kolehmainen, *et al.*, 1999; Austing *et al.*, 2001). This is expected, as Hund's first rule implies that the electron spins align up to half filling of a degenerate shell. The total energy is lowered, as exchange energy is gained by the maximized spin. In the large-N limit, deviations from the above picture (Hirose and Wingreen, 1999) are a simple consequence of the increasing nonparabolicity of the mean-field potential (see Fig. 11).

At relatively large electron densities, the 2D SDFT addition energy spectra compare rather well to results obtained in the unrestricted Hartree-Fock formalism (Yannouleas and Landman, 1999). The Hartree-Fock formalism was also applied to spherical quantum dots, in which the 3D spherical confinement yields the lowest closed shells at $N=2,8,20$ (Bednarek, Szafran, and Adamowski, 1999). These magic numbers were also observed in metallic clusters (Sec. I.B and Fig. 3, upper right panel). However, as the jellium clusters are not rigidly confined, their physical behavior at midshell is different: Jahn-Teller deformation is often energetically more favorable than spin alignment due to Hund's rule at maintained spherical symmetry.

E. Reproducibility of the experimental addition energy spectra

We have seen above that the unrestricted spin-density-functional formalism with the quantum dot electron density as the only fitting parameter indeed seems to provide a fairly accurate description of the addition spectra. However, we notice from Fig. 12 that the agreement between the theoretical data and the experimentally measured addition energies becomes worse with increasing electron number N. Comparing the peak structures in the third and fourth shells, i.e., between $N=6$, $N=12$, and 20, the theoretical and experimental values $\Delta_2(N)$ show very clear deviations. Recently a series of experimental addition energy spectra for 14 different structures was published (Matagne *et al.*, 2001), with diameters between 0.44 and 0.6 μm, similar to the vertical quantum dot device used in the earlier work by Tarucha *et al.* (1996). This work very clearly reveals strong variations in the spectra from device to device: While all structures show the first shell at $N=2$, only 71% of them show shells at both $N=2$ and 6, 64% at $N=2$, 6, and 12, and 21% at $N=2$, 6, 12, and 20. In view of these recent data, which seems to indicate each single quantum dot has its own properties, one should be cautious about a quantitative comparison between theory and experiment like that was in Fig. 12. An explanation for the disagreement at larger shell fillings could, for example, be either nonparabolicity of the confining potential or the unavoidable inaccuracies in device fabrication that randomly disturb the perfect circular symmetry.

F. Oscillator potential with flattened bottom

The effect of deviations from a pure parabolic external confinement on $\Delta_2(N)$ in the midshell regions was further analyzed by Matagne *et al.* (2001), taking into account components of the electrostatic quantum dot confinement in the vertical direction. They solved a 3D Poisson equation for a charge model that included the doped material above and below the quantum dot in a cylindrical configuration. The resulting contributions effectively add an anharmonicity $\sim\lambda r^4$ to the potential. Such a perturbation does not affect the single-particle states of the lowest two shells. In the third shell, however, where the single-particle states $|n,m\rangle=|1,0\rangle$ and $|0,\pm2\rangle$ (with radial and azimuthal quantum numbers n and m) are degenerate in the nonperturbed system, the states $|0,\pm2\rangle$ with nonzero angular momentum are shifted downwards[2] by an energy difference E_λ. Matagne *et al.* (2001) discuss the addition energy spectra for the three cases $E_x>E_\lambda$, $E_x\sim E_\lambda$, and $E_x<E_\lambda$, where E_x labels the exchange energy between two spin-parallel electrons. The chemical potential values $\mu(N)=E(N+1)-E(N)$ were obtained within SDFT in a manner similar to that used by Nagaraja *et al.* (1999; see also Jovanovic and Leburton, 1994).

Figures 13 and 14 summarize the results of Matagne *et al.* (2001) for the filling of the third shell, i.e., between $N=6$ and $N=12$. For $E_x>E_\lambda$ (see upper panel of Fig. 13) the situation is similar to that of a purely harmonic external confinement. When all single-particle states in the third shell are exactly degenerate, the shells are filled according to the sequence $(\Sigma m)^{(\Sigma s_z)}=2^{1/2}\rightarrow2^1\rightarrow0^{3/2}\rightarrow2^1\rightarrow2^{1/2}\rightarrow0^0$ when proceeding from the second shell at $N=6$ to the third shell at $N=12$ (see Fig. 14).

The addition energy spectra in Fig. 13 are consistent with the addition energies and spin fillings in Fig. 12 above. If the degeneracy between the $|0,\pm2\rangle$ and $|1,0\rangle$ states is lifted by a small difference in energy (see Fig. 14, middle panel), the shell-filling sequence changes to $(\Sigma m)^{(\Sigma s_z)}=2^{1/2}\rightarrow0^1\rightarrow0^{3/2}\rightarrow2^1\rightarrow0^{1/2}\rightarrow0^0$. For very small splitting the addition energy spectrum does not change significantly. For larger splitting, at midshell $N=9$ the spin remains at its maximum value (Hund's rule). The enhanced energy difference between the

[2]Note the similarity to the Nilsson model in nuclear physics, in which phenomenological $\mathbf{l}^2$ term for angular momentum $\mathbf{l}$ and a spin-orbit contribution, which we may neglect here, were subtracted from the oscillator Hamiltonian to flatten the bottom of the harmonic well: states with higher single-particle angular momenta are shifted to smaller energies (Nilsson, 1955; Bohr and Mottelson, 1975).

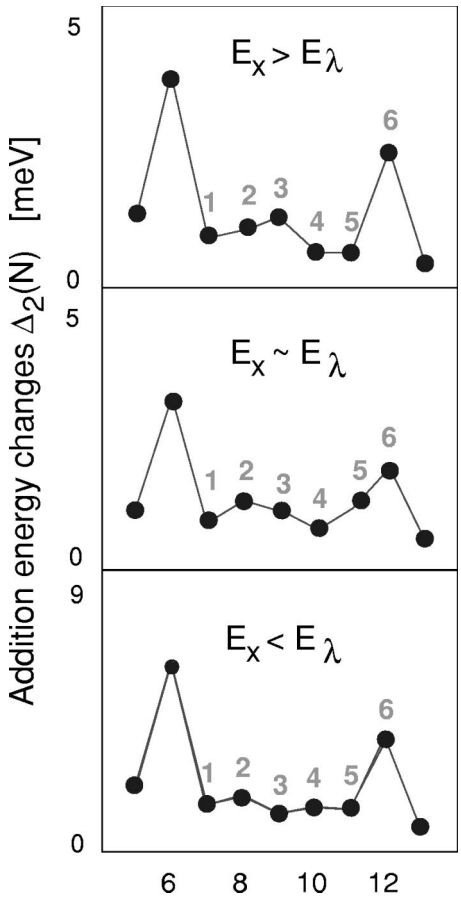

FIG. 13. Addition energy differences for different magnitudes of E_λ compared to E_x, where E_x labels the exchange energy between two spin-parallel electrons and E_λ is the energy shift due to an anharmonicity $-\lambda r^4$ of the confining potential. After Matagne *et al.*, 2001.

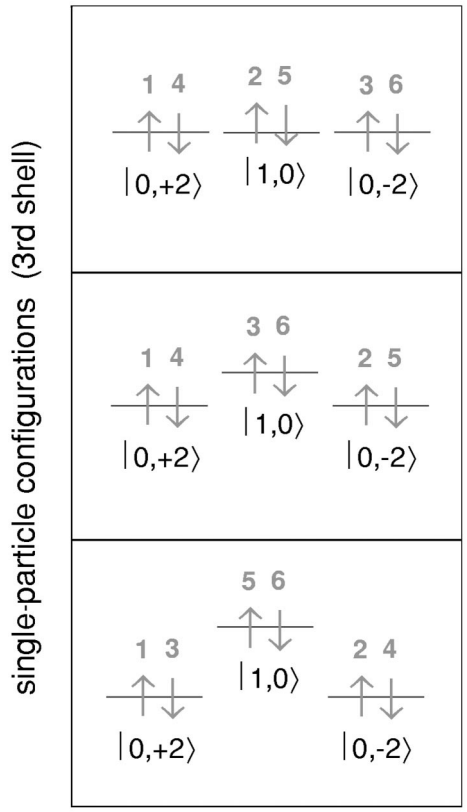

FIG. 14. Schematic single-particle configurations $|n,m\rangle$ and occupation sequences in the third shell from $N=7$ to $N=12$. After Matagne *et al.*, 2001.

$|0,\pm 2\rangle$ and $|1,1\rangle$ states, however, leads to a reduction in $\Delta_2(9)$ and to a higher value of the addition energy at $N=8$ ($E_x \sim E_\lambda$, Fig. 13, middle panel). For an even larger energy splitting between the $|0,\pm 2\rangle$ and $|1,0\rangle$ states, maximum spin alignment is first reached for the subshell formed by the $|0,\pm 2\rangle$ states. The $|1,0\rangle$ state is filled subsequently (Fig. 14, lower panel). Thus the addition energies show a small maximum at $N=8$ and an even smaller one at $N=10$ ($E_x < E_\lambda$, Fig. 13, lower panel). Matagne *et al.* (2001) concluded that maximum spin alignment at midshell does not guarantee the occurrence of corresponding maxima in the addition energy spectra. They also pointed out that for Hund's first rule to apply, the states do not necessarily need to be quasidegenerate (see also Austing *et al.*, 2001).

G. Three-dimensionality of the confinement

The actual thickness of a quantum dot relative to its lateral extent depends on both the fabrication method and the applied gate voltages. Experimentally, for typical quantum dots the depth in the growth direction of the heterostructure material is about one order of magnitude smaller than the lateral extent. Thus, neglecting a possible extension of the electron cloud in the z direction, the above description of quantum dots in two dimensions seemed justified. Within this approximation, the addition energy spectra from both exact diagonalization and mean-field approaches compare well with the experimental results. [This also holds for the dependence of $\Delta_2(N)$ on magnetic fields; see Sec. V.] However, as pointed out by several authors, such a comparison may be obscured by an adjustment of the average electron density, which (as it defines the strength of the Coulomb interactions between the particles) can mask 3D effects (Fujito *et al.*, 1996; Maksym and Bruce, 1997; Nagaraja *et al.*, 1997; Lee *et al.*, 1998; Rontani *et al.*, 1999a, 1999b; Jiang *et al.*, 2001; Pi, Emperador, *et al.*, 2001).

Rontani *et al.* (1999a, 1999b) compared the exact energies and pair correlations for a two-electron quantum dot to results of Hartree-Fock and a single-site Hubbard model. They showed that the differences between these approximate approaches and the exact solution are reduced in the three-dimensional case. This is due to the fact that the 2D description artificially enhances the strength of the Coulomb and exchange matrix elements.

Bruce and Maksym (2000) used the exact diagonalization method to study the effects of the three-dimensionality of the confinement potential in a realistic quantum dot (here with $N=3$), including the screening of the electrons by the metallic gates.

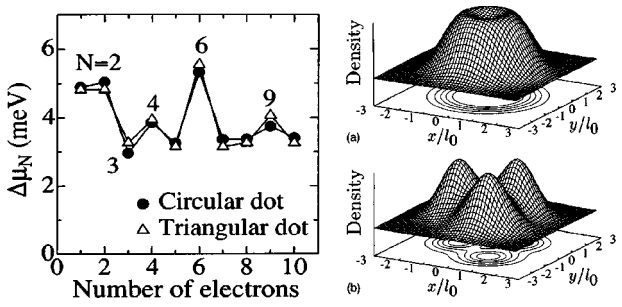

FIG. 15. Addition energy differences and density distribution for (a) circular and (b) triangular quantum dots with three electrons. The length unit is $l_0 = 20$ nm. From Ezaki *et al.*, 1997.

The most important 3D effect in small dots seems to be the change in the effective Coulomb interaction between the electrons. However, while important for a detailed quantitative description, this effect seems not to lead to qualitatively new features when compared to the strictly 2D model. This holds as long as the dot is quasi-two-dimensional in the sense that only the lowest single-particle state perpendicular to the dot plane is occupied. In this review we concentrate mainly on the strictly 2D case, which has turned out to be surprisingly rich and difficult. When comparing with experiments, the reader should note, however, that the parameters (such as electron density, confinement strength, etc.) providing a good agreement with experiment might be slightly different in a 3D model.

H. Triangular quantum dots

Ezaki *et al.* (1997, 1998a, 1998b) determined the addition energy spectra from numerical diagonalization of the full many-body Hamiltonian, Eq. (5) (excitations along the z direction of the confinement were ignored). In addition to a circular oscillator, they considered a triangular deformation of the confinement,

$$V(r,\phi) = \frac{1}{2} m^* \omega^2 r^2 \left(1 + \frac{2}{7} \cos(3\phi) \right), \tag{12}$$

with polar coordinates (r,ϕ). For material parameters $m^* = 0.065 m_e$, $\varepsilon = 12.9$ (corresponding to values between InAs and GaAs), and an oscillator shell spacing $\hbar\omega = 3$ meV, the addition energy spectra obtained from the many-body ground-state energies $E(N)$ are shown in Fig. 15.

In the single-particle model, the lowest shells of both circular (spherical) and triangular (tetrahedral) geometries in 2D (3D) are similar (Hamamoto *et al.*, 1991; Brack *et al.*, 1997; Reimann *et al.*, 1997; Reimann, Koskinen, Helgesson, *et al.*, 1998). Thus it is not surprising that at relatively large densities, the addition energy spectra for both symmetries differ only very little. In both cases, shell closings are found at $N = 2$ and $N = 6$, with additional maxima at $N = 4$ and 9 due to spin polarization.

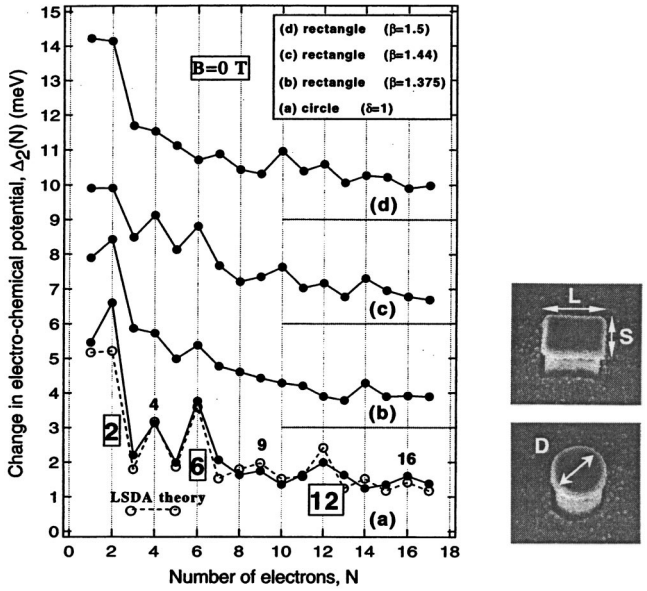

FIG. 16. Measured addition energy differences $\Delta_2(N)$ as a function of electron number N for different rectangular quantum dot structures with estimated length/side ratios: (b) $L/S = 1.375$; (c) 1.44; and (d) 1.5. The different curves are offset by 3 meV and the results for the circular dot (a) are shown for comparison. From Austing, Sasaki, *et al.*, 1999.

Naturally, for a confinement with circular symmetry, the density distribution obtained from the "exact" wave function, as shown in the upper right panel of Fig. 15, has azimuthal symmetry. Triangular deformation breaks this symmetry, and localization of electrons due to their Coulomb repulsion becomes visible in the electron density: Three electrons confined by a triangular potential localize in the corners of the triangle. [Similar results were reported by Creffield *et al.* (1999), who studied two interacting electrons in polygonal quantum dots by exact diagonalization techniques. They observed a transition from a weakly correlated charge distribution for small dots to a strongly correlated Wigner molecule. See also Jefferson and Häusler (1997). A further discussion of Wigner crystallization in parabolic quantum dots is given in Sec. IV.A.]

I. Elliptic deformation

For a rectangular dot structure like that displayed in the upper right panel of Fig. 16, one should expect the effective lateral confinement to have an elliptic shape: at the corners, the electrostatic potential is rounded off, provided that the number of electrons in the dot is not too large. The left panel of Fig. 16 shows the experimental addition energy changes $\Delta_2(N)$ for deformed quantum dots with estimated ratios of side lengths $L/S = 1.375$ [curve (b)], 1.44 [curve (c)] and 1.5 [curve (d)]. We notice that the shell structure for circular dot shape [curve (a) in Fig. 16] has been smeared out in the deformed case: for the rectangular dot structures [curves (b)–(d)], no prominent maxima of $\Delta_2(2,6,12)$ are found.

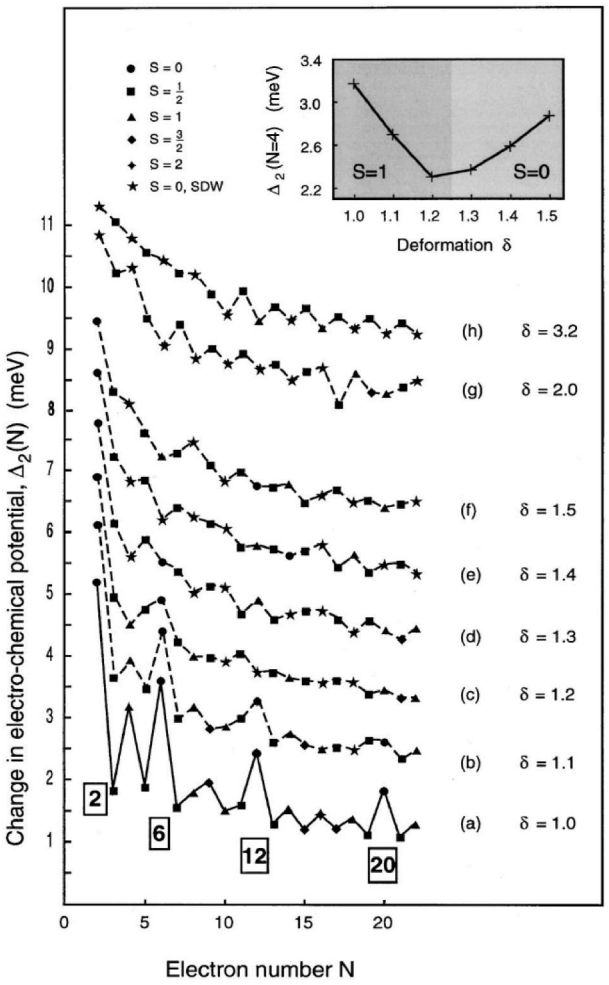

FIG. 17. Calculated addition energy differences $\Delta_2(N)$ for elliptic quantum dots with deformation δ, obtained within the local spin-density approximation. The curves are offset by 1 meV. There is an additional offset of 1 meV between (f) and (g). The different symbols correspond to the different spins, as defined in the figure. The inset shows $\Delta_2(4)$ versus δ. Between $\delta=1.2$ and $\delta=1.3$, a transition between a spin-triplet and a spin-singlet state occurs. From Austing, Sasaki, *et al.*, 1999.

Exact numerical diagonalization methods (Ezaki *et al.*, 1997, 1998a, 1998b; Maksym, 1998; Zhu, 2000), as well as spin-density-functional methods (Lee *et al.*, 1998, 2001; Reimann, Koskinen, Helgesson, *et al.*, 1998, Reimann, Koskinen, Lindelof, *et al.*, 1998; Austing, Sasaki, *et al.*, 1999; Hirose and Wingreen, 1999; Reimann, Koskinen, Kolehmainen, *et al.*, 1999) predict significant modifications of the addition energy spectra, accompanied by transitions in the spin states with increasing deformation. One can model such a rectangular quantum dot by an anisotropic oscillator potential $V=(1/2)\,m^*(\omega_x^2x^2+\omega_y^2y^2)$ with deformation-dependent frequencies $\omega_x=\omega\sqrt{\delta}$ and $\omega_y=\omega/\sqrt{\delta}$ [see Eq. (1)]. We impose the constraint $\omega^2=\omega_x\omega_y$, which is equivalent to conserving the area of the quantum dot with deformation. For $\delta=1$, the dot shape is circular, whereas $\delta>1$ corresponds to an elliptical shape. The oscillator frequency ω is approximated by Eq. (11). Minimizing the Kohn-Sham energy density functional in a manner similar to that described in Sec. III.D above allows us to determine the addition energy spectra $\Delta_2(N)$ for various values of the deformation δ, as displayed in Fig. 17 [where the circular shell structure in local spin-density approximation is included again in panel (a) for comparison]. By deforming the confinement slightly, one can still identify the shell closures at $N=2, 6$, and 12, but with significantly suppressed amplitudes: even a very small deviation from perfect circular symmetry, where the single-particle level degeneracies are lifted by just a small amount, can have a very noticeable effect on $\Delta_2(N)$. For $\delta\geqslant1.2$, the circular shell structure is completely eliminated. At certain deformations one expects accidental degeneracies, leading to subshells (see Fig. 2), for which the sequence of magic numbers differs from the circular case. At $\delta=2$, for example, shell closures occur at 2, 4, 8, 12, and 18. Compared to circular symmetry, however, the reduced separation between the subshells makes any shell structure less clear to observe. A systematic comparison between curves (b)–(d) in Fig. 16 and curves (b)–(h) in Fig. 17 fails: although the experimental data of curve (b) in Fig. 17 partly resemble the theoretical addition energies for deformations between $\delta=1.1$ and $\delta=1.3$, the data of curves (c) and (d) do not compare well to the SDFT values for $\delta>1.3$. For $\delta\geqslant2$ we observe a tendency to odd-even oscillations.

The SDFT calculations described here are strictly two dimensional, so the strength of the Coulomb interactions may be overestimated. Lee *et al.* (2001) take the finite thickness into account and provide a systematic study of addition energies as a function of the dot deformation for $N\lesssim12$. They point out that, due to electron-electron interactions, the anisotropy of the elliptic effective potential is higher than the deformation of the trap, in agreement with the results of Austing, Sasaki, *et al.* (1999).

In practice, screening by the metal contacts surrounding a dot is also believed to reduce the influence of Coulomb interactions (Bruce and Maksym, 2000). The three-dimensional model of Lee *et al.* (1998) incorporated the self-consistent solution of the Poisson equation into the spin-density-functional calculation for an anisotropic oscillator. Since the confinement strength was considerably larger, a direct comparison to the above results is difficult. Qualitatively, however, their results, as well as those of Hirose and Wingreen (1999), are in agreement with those of Fig. 17. When comparing the experimental spectra to the predictions of LSDA as well as to exact diagonalization results, however, one meets a major difficulty: even a small deformation can make a big difference, as is evident from the very different patterns in spectra (a)–(d) in Fig. 16. It is nearly impossible to determine the actual ratio of semiaxes of the dot with an accuracy high enough to allow a comparison with the theoretical model at the corresponding deformation. Furthermore, the precise details are device dependent: we saw in Sec. III.E that even for two circular structures, the addition energy spectra can vary considerably from dot to dot.

Transitions in the ground-state spin configurations with deformation are indicated in Fig. 17. These transitions are particularly numerous for, but not restricted to, dots with an even electron number. The change of spin with deformation is most easily understood for the example $N=4$. The inset in Fig. 17 shows $\Delta_2(4)$ versus deformation up to $\delta=1.5$. In the circular dot, the degeneracy at the Fermi surface leads to a spin-triplet state (Hund's rule). The deformation resolves the degeneracy and, at a certain energy splitting of the two single-particle levels, it is energetically favorable to form a spin-singlet state (see the single-particle spectra of an elliptic harmonic oscillator in Fig. 2 above). For $N=6$ a transition from $S=0$ at circular shape (corresponding to a shell closing with nonmagnetic ground state) to an $S=1$ triplet state at $\delta=1.5$ occurs. As a function of deformation, the dots can show *piezomagnetic behavior*, i.e., changes in the magnetization with deformation. Clearly these spin changes are very sensitive to the actual value of the deformation. Such behavior was also predicted from exact diagonalization studies for ellipsoidal quantum dots with up to 10 electrons (Ezaki *et al.*, 1998a, 1998b). These calculations revealed a transition from spin singlet to triplet at $\delta\approx1.2$ for $N=4$, as well as the consecutive filling of states by spin-up and spin-down electrons [see curves (g) and (h) in Fig. 17]. Experimentally, evidence for such singlet-triplet transitions as a function of deformation came from a careful study of the magnetic-field dependence of the addition energy spectra. We refer the reader to the work by Austing, Sasaki, *et al.* (1999), in which a detailed discussion is given of the four-electron case. [For a given deformation as a function of N, the spin changes only in steps of 1/2. This indicates that spin blockade (Weinmann, Häusler, and Kramer, 1995), which requires $\Delta S>1$, should not occur in small deformed quantum dots.]

J. Self-assembled pyramidal quantum dots in the local spin-density approximation

Fonseca *et al.* (1998) studied the electronic structure of pyramidal self-assembled InAs-GaAs quantum dots in the local spin-density approximation. An example of such a dot structure is shown in Fig. 18(a), where the pyramidal InAs quantum dot is embedded in a GaAs matrix. A continuum model for the strain in the pyramid, the thin InAs layer from which the pyramidal dots are formed, and the surrounding GaAs matrix was applied. The electron-electron interactions were treated in density-functional theory in the LSDA. For different heights of the pyramids, Fig. 18(b) shows the number of electrons in the dot as a function of the applied voltage V_g. As in the above example of a two-dimensional parabolic dot, it could be shown that the electron filling of the InAs dots follows Hund's rule, the results being in good agreement with the experimental data of Fricke *et al.* (1996).

In a similar study, Shumway *et al.* (2000) quantified the error introduced by the LSDA by comparison to the diffusion quantum Monte Carlo method. They showed that the LSDA errors in this case are small, the largest error coming from the local approximation to the exchange.

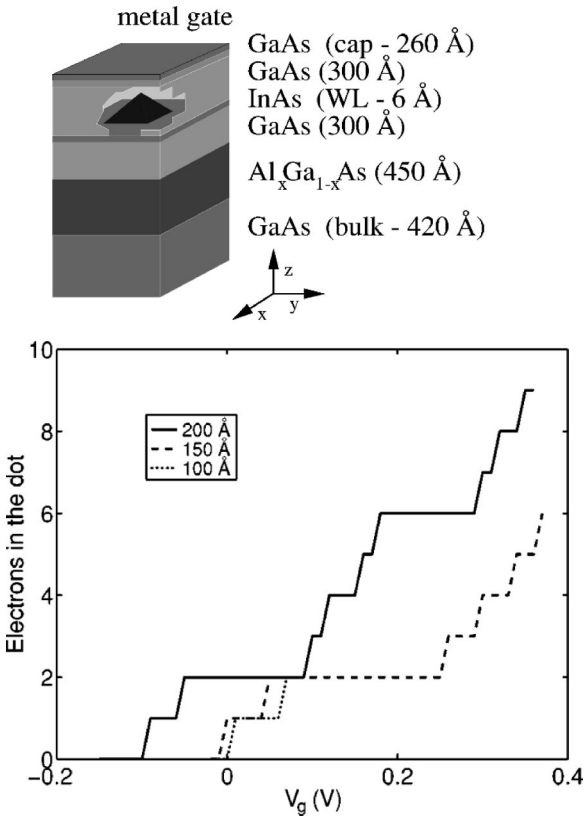

FIG. 18. Pyramidal structure of a self-assembled InAs quantum dot: upper panel, schematic picture; lower panel, number of electrons vs gate voltage for different pyramid height $d/2$. From Fonseca *et al.*, 1998.

IV. INTERNAL ELECTRONIC STRUCTURE

In this section we turn to a discussion of correlated states in quantum dots, which typically exhibit a complicated internal structure and lead to characteristic features in the excitation spectrum. It is well established that for low electron densities the repulsion between the electrons causes an ordered spatial structure, the Wigner lattice, which breaks the translational symmetry in the infinite electron gas. Corresponding phenomena for finite-size electron droplets are discussed in Sec. IV.A. Spin-density-functional calculations predict broken-symmetry states for both the spin and charge densities of quantum dots (see Sec. IV.B), while *a priori* these features are less obvious in the many-body correlated states evaluated by the configuration-interaction method. A comparison of these approaches is made in Secs. IV.C and IV.D, where we demonstrate that characteristic features related to Wigner crystallization and spin-density waves indeed are present in the configuration-interaction results. We conclude with a discussion of quantum Monte Carlo results, which provide an alternative method (Sec. IV.E).

A. Classical electron configurations

In 1934, Wigner predicted that electrons crystallize and form a lattice if the density of the three- or two-dimensional electron gas is lowered beyond a certain critical value. This is due to the fact that the Coulomb energy increases relative to the kinetic energy and correlations begin to strongly dominate the electronic structure. For a homogeneous three-dimensional electron gas, such crystallization is expected at very low densities, i.e., at large values of the average Wigner-Seitz radius r_s. For the critical value at which this transition occurs, Ceperley and Alder (1980) reported the value $r_s = 100a_B^*$. In two dimensions, however, this transition to a Wigner-crystal-like state occurs at densities corresponding to $r_s > 37a_B^*$ (Tanatar and Ceperley, 1989). According to Rapisarda and Senatore (1996), the formation of the Wigner crystal is preceeded by a transition to a polarized phase. If translational invariance is broken in a two-dimensional electron gas, the critical density for the transition to the Wigner crystal is shifted to the considerably smaller value $r_s \approx 7.5a_B^*$ (Chui and Tanatar, 1995). Thus one may speculate that, in finite systems with broken translational invariance, localization should occur at significantly larger densities than in the 2D bulk. Studies along these lines were recently performed by various authors (see, for example, Creffield *et al.*, 1999; Egger *et al.*, 1999; Yannouleas and Landman, 1999; Filinov, Bonitz, and Lozovik, 2001) using different calculational methods. For circular and ring-shaped quantum dots, we shall compare these results (which were mostly based on the quantum Monte Carlo approach) with those obtained by exact diagonalization.

In the low-density limit, where the electron gas becomes crystallized, it is not *a priori* obvious how the electrons, now behaving as classical point charges, will arrange geometrically in the harmonic trap. In the 2D bulk, the crystal would form a triangular lattice (Tanatar and Ceperely, 1989). For finite sizes, however, a compromise must be found between the triangular lattice and the shape of the confinement. Early studies of this problem were performed by Lozovik and Mandelshtam (1990, 1992). Bolton and Rössler (1993) modeled the classical charge distribution in Wigner-like states of a quantum dot using a Monte Carlo algorithm (see Date, Murthy, and Vathsan, 1998, for a general analytic approach.)

For the smallest systems $N \leqslant 5$, simple polygons are formed. The first nontrivial configurations are found for $N=6$: in addition to the ground state with five particles surrounding a single particle in the trap center, metastable states and isomers at very similar energies exist. The bent triangle shown in Fig. 19 is practically degenerate, with a perfect hexagon (not shown in Fig. 19). For $N=10$, the ground state with a "dimer" in the center and eight surrounding electrons has an isomer with a triangular center and seven electrons on the outer ring. The lowest-energy geometries obtained for 15, 19, 30, and 34 point charges are shown in the other panels of Fig. 19. Following Bolton and Rössler (1993), for the smaller sizes the formation of a geometric shell pattern can be observed, in which the electrons are arranged in concentric rings. This was noticed earlier by Lozovik and Mandelshtam (1990, 1992) and was also confirmed by Bedanov and Peeters (1994) for somewhat larger N. Each of these ringlike geometric shells can be filled with a certain maximum number of particles, independent of the confinement frequency. Bedanov and Peeters used this property to group the configurations by the point symmetry of the inner shell. When all geometric shells are filled up to a maximum number of particles, a new singly occupied shell is created in the center. If two neighboring shells are filled with particle numbers that are incommensurate, low-energy excitations in the form of inner-shell rotations are found (Lozovik and Mandelshtam, 1992; Schweigert and Peeters, 1994, 1995). In the commensurate case, however, the configuration is particularly stable against structural excitations and is frequently called "magic," in some analogy to the magic shell closings discussed in the previous sections. We emphasize that the terminology of a "shell" used here must not be confused with the grouping of levels in the eigenspectra, which is why we should actually prefer "geometric shells" and "geometric magic numbers" to describe the most stable classical electron configurations. For large systems $N > 200$, the center region of the system very closely resembles a triangular lattice in which all the particles are sixfold coordinated, while the outer electrons form ringlike shells (Bedanov and Peeters, 1994). Schweigert and Peeters (1994, 1995) found that the melting of the classical configurations at finite temperature begins by the rotation of neighboring

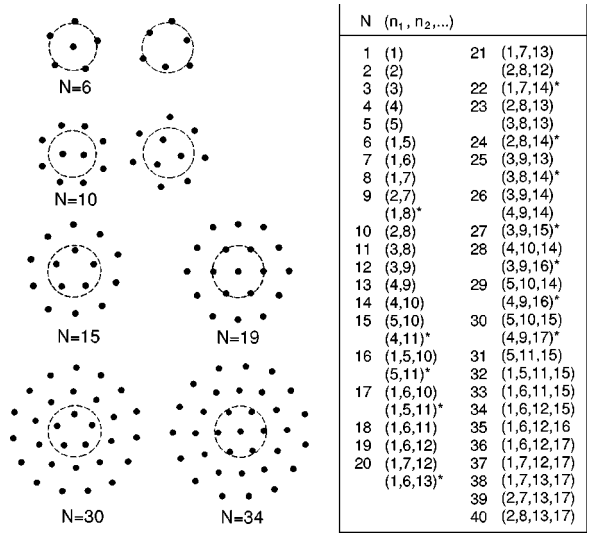

N	$(n_1, n_2, \ldots)$		
1	(1)	21	(1,7,13)
2	(2)		(2,8,12)
3	(3)	22	(1,7,14)*
4	(4)	23	(2,8,13)
5	(5)		(3,8,13)
6	(1,5)	24	(2,8,14)*
7	(1,6)	25	(3,9,13)
8	(1,7)		(3,8,14)*
9	(2,7)	26	(3,9,14)
	(1,8)*		(4,9,14)
10	(2,8)	27	(3,9,15)*
11	(3,8)	28	(4,10,14)
12	(3,9)		(3,9,16)*
13	(4,9)	29	(5,10,14)
14	(4,10)		(4,9,16)*
15	(5,10)	30	(5,10,15)
	(4,11)*		(4,9,17)*
16	(1,5,10)	31	(5,11,15)
	(5,11)*	32	(1,5,11,15)
17	(1,6,10)	33	(1,6,11,15)
	(1,5,11)*	34	(1,6,12,15)
18	(1,6,11)	35	(1,6,12,16
19	(1,6,12)	36	(1,6,12,17)
20	(1,7,12)	37	(1,7,12,17)
	(1,6,13)*	38	(1,7,13,17)
		39	(2,7,13,17)
		40	(2,8,13,17)

FIG. 19. Classical electron configurations: Left, schematic view of the classical electron configurations in a parabolic potential for $N=6$, 10, 15, 19, 30, and 34, after Bolton and Rössler, 1993; right, classical ground-state configurations with geometric shells $(n_1, n_2, \ldots)$, after Bedanov and Peeters, 1994. In some cases, in particular for large N, the calculated configurations differ from those observed in a macroscopic experimental setup by Saint Jean, Even, and Guthmann, 2001. These configurations are marked with a star.

shells relative to each other, finally leading to a radial broadening and overlap of the shells.

Experimental investigations of classical Wigner clusters were performed by Saint Jean, Even, and Guthmann (2001) with a macroscopic setup consisting of electrostatically interacting charged balls of millimetric size. These balls moved in an electrostatically created, cylindrically symmetric confining potential, which could be considered as parabolic. In agreement with the numerical simulations discussed above, regular polygons were formed for $N \leqslant 5$. For $N=6$, they confirmed the centered pentagon (Fig. 19) as the ground state, together with the hexagonal metastable states. In the experiment, for increasing N one finds the configurations (1,6), (1,7), (1,8), and then (2,8), labeled by the number of particles $(n_1, n_2, \ldots)$ in each geometric shell, starting from the dot center.

Differences in the results reported by Bolton and Rössler (1993), Bedanov and Peeters (1994), Schweigert and Peeters (1995), and Lai and Lin (1999) were observed for $N=9$ and $N \geqslant 15$. Using a Monte Carlo approach, Campbell and Ziff (1979) predicted (1,8) and (4,11) as the ground-state configurations for $N=9$ and $N=15$, respectively. In contrast to the previously mentioned numerical results, which predicted the configurations (2,7) and (5,10), these data coincide with the experimental result. For larger N, generally the data by Campell and Ziff are closer to the experiment. According to Saint Jean *et al.* (2001), the explanation for these discrepancies could lie in the fact that, with increasing N, the number of metastable states and isomers, all being very close in energy, increases drastically. This introduces difficulties that could account for the observed differences.

In a three-dimensional harmonic confinement, the classical electrons tend to form concentric spheres with, again, several isomers (Manninen, 1986).

B. Spin polarization in the local spin-density approximation

Let us now consider the liquid regime at higher electron densities, i.e., smaller values of the two-dimensional density parameter $r_s = 1/\sqrt{\pi n}$. It was mentioned above that in addition to providing a reliable approximation to the ground-state energy and the spin, spin-density-functional theory also yields the ground-state density $n(\mathbf{r}) = n_\uparrow(\mathbf{r}) + n_\downarrow(\mathbf{r})$ for which the energy functional $E[n_\uparrow, n_\downarrow]$ is minimal. Surprisingly, in some cases the mean-field solution predicts a spatial modulation of the spin density (i.e., the spin polarization $\zeta = [n_\uparrow - n_\downarrow]/n$). Such ground states with broken symmetry were recently much debated and it was argued that they are an artifact of spin-density-functional theory. To resolve this question, after summarizing the controversial SDFT results, we shall compare them with the results of the exact diagonalization method (see Secs. IV.B.3, IV.C, and IV.D).

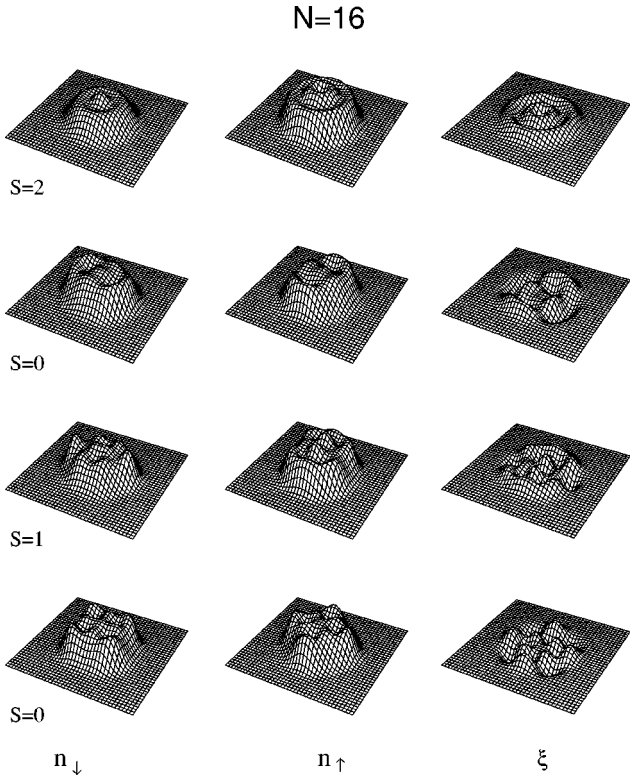

FIG. 20. Ground state ($S=2$, first row) and isomeric states for a circular dot with 16 electrons at $r_s = 1.5 a_B^*$. The maximum amplitude for the polarization corresponds to $\zeta \approx 0.23$. The energy differences with respect to the ground state are 18.1 mRy* ($S=0$, second row), 20.2 mRy* ($S=1$, third row), and 20.7 mRy* ($S=0$, fourth row). From Koskinen *et al.*, 1997.

1. Circular and elliptic quantum dots

Dots with closed shells have a large Fermi gap and are nonmagnetic, with spin $S=0$. For nonclosed shells, the spin in most cases is determined by Hund's first rule. For larger dots, one finds different spin isomers, all slightly higher in energy than the ground-state configuration.

As an example, Fig. 20 shows the spin-up and spin-down densities $n_\uparrow$ and $n_\downarrow$ and the polarization $\zeta = (n_\uparrow - n_\downarrow)/n$ of four different spin states with $S=2$, 0, 1 and 0 (with increasing energy) for a quantum dot with 16 electrons, calculated in SDFT. The ground state has a total spin $S=2$ in agreement with Hund's first rule. Intriguingly, the distribution of excess spin at both $S=2$ and $S=1$ is nonhomogeneous, with some similarity to the spin-inversion states found by Gudmundsson and Pálsson (1994) and Gudmundsson and Palacios (1995) for finite magnetic fields. If the total spin is zero, one would expect the system to be unpolarized, $\zeta(\mathbf{r}) = 0$. However, in both cases with $S=0$ one notices that the densities $n_\uparrow$ and $n_\downarrow$ are spatially deformed and twisted against each other by $\pi/2$. The total density $n_\uparrow + n_\downarrow$ retains circular symmetry. However, the spin density $n_\uparrow - n_\downarrow$ and correspondingly the spin polarization show a spatial dependence reminiscent of the spin-density-wave states in the bulk (Overhauser, 1960, 1962, 1968). For larger N or below a critical density, in the local spin-density approximation such spin-density-wave-like states with $S=0$ can

occur as ground states. At $r_s=1.5a_B^*$, for example, this is the case for $N=24$ and $N=34$.

The occurrence of $S=0$ spin-density-wave states is accompanied by a change in the single-particle spectrum: one always finds a pair of degenerate spin-up and spin-down orbitals and a large Fermi gap. The latter effect is well known: in the case of degeneracy (as, for example, at nonclosed shells), spontaneous Jahn-Teller (1937) symmetry breaking of the effective field, accompanied by a lowering of the density of states at the Fermi surface, leads to an energetically more stable situation (see also the discussion in Sec. I.A). In this context one should be aware that the mean-field solution maps out the internal structure of the wave function, in contrast to the exact wave function, which naturally retains rotational symmetry. The spin-density-wave internal symmetry breaking is closely related to the internal deformation found in nuclei and atomic clusters (Häkkinen *et al.*, 1997).

If within the Hartree-Fock approximation one considers a linear combination of all possible single Slater determinants, one can generate a proper eigenfunction to S^2 and S_z. The symmetry-restored state would then show two-particle correlations which are consistent with the single-determinant state. While the LSDA scheme does not formally yield a single determinantal wave function and the Kohn-Sham single-particle wave functions lack a direct physical interpretation (as do the corresponding single-particle energies), a similar reasoning applies (Yakimenko, Bychkov, and Berggren, 2001). The Kohn-Sham mean-field ground-state density mimics the internal structure of the exact wave function, trying to reveal correlations inherent in the true ground state (see Sec. IV.B.3).

Looking more systematically at the polarization of dots with different N, one finds that for $r_s=1.5a_B^*$ at closed shells, $N=6$, 12, 20, and 30, the dot is completely unpolarized and $S=0$. For nonclosed shells, Hund's first rule favors the spin alignment. In cases where $S\neq 0$, naturally the spin polarization takes nonzero values and furthermore shows a strong spatial dependence. As observed for $N=16$ in Fig. 20, such a nonuniform spin polarization can also occur when the total spin is zero. For increasing values of r_s, i.e., at lower densities, shell structure gets disrupted and spatial variations in ζ can also be found for closed shells $N=2,6,12,20,\ldots$. The spin-density-wave states can then occur together with the formation of charge-density-wave states, as discussed by Hirose and Wingreen (1999) and Yannouleas and Landman (1999, 2000b) in the framework of geometrically unrestricted spin-density-functional and Hartree-Fock calculations.

If we deform the external harmonic confinement elliptically as described by Eq. (1), the $S=0$ spin-density-wave states occur frequently as ground states even at rather high densities of the 2D electron gas. (The changes in spin structure as a function of deformation are displayed in Fig. 17 above.) For example, at $r_s=1.5a_B^*$ and circular shape ($\delta=1$), a closed-shell quantum dot with $N=6$ is unpolarized. By deformation, the shell structure changes considerably and an $S=0$ spin-density-wave state is formed. For $\delta>1.5$ this state changes to a ground state with spin $S=1$, and then it changes back to a spin-density-wave state ($\delta=2$). This piezomagnetic behavior originates from the fact that the level structure at the Fermi surface changes with deformation (Reimann, Koskinan, Lindelof, *et al.*, 1998).

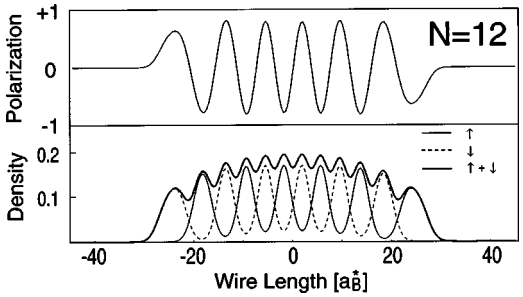

FIG. 21. Spin polarization (upper panel) and densities (lower panel) of a finite quantum wire with 12 electrons at deformation $\delta=25$, plotted along the x axis ($y=0$). From Reimann, Koskinen, and Manninen, 1999.

2. Quantum wires and rings

a. Quantum wires

Turning to extreme deformations $\omega_x \ll \omega_y$ of the oscillator potential, the occupied single-particle orbitals are mostly determined by the quantization in the x direction, i.e., the system becomes quasi-one-dimensional. An example is shown in Fig. 21 for a finite quantum wire with 12 electrons at a deformation $\delta=25$, where the parameter ω equals that of a 2D system at $r_s=1.5a_B^*$. Densities and spin polarizations are plotted along the x axis at $y=0$. Spin-up and spin-down densities show a pronounced oscillation and are shifted against each other, leading to a very pronounced spin-density wave, with a weak charge-density wave superimposed. The fully polarized solution is 88.2 mRy* higher in energy than the spin-density wave. The single-particle energies show a Fermi gap that is a factor 1.6 larger than the full bandwidth of 125 mRy* (i.e., the energy difference between the highest and the lowest occupied single-particle level). In the quasi-one-dimensional electron gas the spin-density wave results from a spin Peierls transition opening a Fermi gap. In such finite quantum wires the electron states can be localized at the ends of the wire, similar to the way in which surface states can appear in a crystal lattice (Tamm, 1932; Zangwill, 1988; Ohno *et al.*, 1990), but with the periodic potential now created by the spin-density wave (Reimann, Koskinen, and Manninen, 1999).

b. Quantum rings

A ring-shaped quasi-one-dimensional quantum wire can be modeled by a potential of the form $V(r)=1/2\,m^*\omega^2(r-r_0)^2$, which for moderate confinement corresponds to a harmonic dot with its center removed. The parameters determining the properties of the quantum ring are its radius r_0, the number of electrons N,

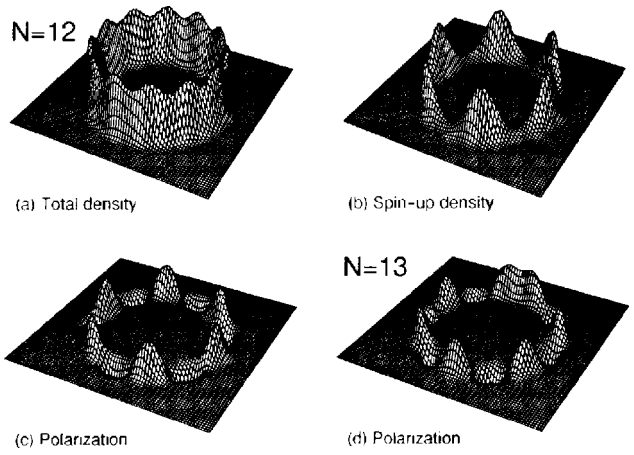

FIG. 22. Quantum rings with $N=12$ and $N=13$ electrons (parameters as defined in the text): (a) total electron density ($n_{\max}=0.157a_B^{*-2}$); (b) spin-up density; (c) spin polarization; (d) like (c) but for $N=13$. The maximum spin polarization in (c) and (d) is $\zeta=0.8$. From Reimann, Koskinen, and Manninen, 1999.

and the strength ω of the harmonic confinement in the radial direction. The quantities r_0 and ω are related to the one-dimensional density $n=1/(2r_s)$ along the ring, $r_0=Nr_s/\pi$, and a dimensionless parameter C_F describing the excitation energy of the next radial mode. The latter is defined to be C_F times the 1D Fermi energy, and one thus obtains $\hbar\omega=C_F\hbar^2\pi^2/(32m^*r_s^2)$ (see Koskinen *et al.*, 2001).

Figure 22 shows the LSDA densities and spin polarizations of quantum rings with $N=12$ and $N=13$ electrons at $r_s\approx 2a_B^*$, with $r_0=8a_B^*$ and $C_F\approx 17$. In the 12-electron case, the spin-down density (not shown in Fig. 22) is rotated against the spin-up density [panel (b)] by an angle of $\pi/6$, forming a strong spin-density wave with antiferromagnetic order. The spin-density wave is 213 mRy* lower in energy than the fully polarized case and 227 mRy* lower than the nonmagnetic LDA solution. The Fermi gap with 220 mRy* is a factor of 3.6 larger than the bandwidth of the occupied levels, pointing to the possibility that the low-energy excitations are collective in nature as for a strictly 1D Coulomb gas (Kolomeisky and Straley, 1996).

For both $N=12$ and $N=13$ [where the "unpaired" spin has led to two parallel spins for neighboring electrons; see panel (d) in Fig. 22], a small-amplitude charge-density modulation occurs, which can be interpreted as a precursor to a charge-density-wave state or, in the low-density limit, to a 1D "Wigner molecule" (Häusler and Kramer, 1993; Jauregui, Häusler, and Kramer, 1993; Maksym, 1993; Schulz, 1993).

3. Artifacts of mean-field theory?

The above mean-field results for circular, elliptical and ring-shaped quantum dots very clearly revealed the possible occurrence of Jahn-Teller-type solutions with broken symmetries in both the spin and charge densities (Jahn and Teller, 1934). Hirose and Wingreen (1999) and later Pederiva *et al.* (2000) argued that for a circular quantum dot the eigenstates can always be chosen to have definite angular momentum, and hence the density distribution should be rotationally invariant. Indeed, one encounters the conceptual difficulty that the symmetry of the solution differs from the symmetry of the Hamiltonian. The underlying problem, however, is that the single-determinant wave function of the mean field is a poor approximation to the full many-body ground state, which naturally cannot account for its full quantum-mechanical description. Ring and Schuck (1980) pointed to this general difficulty in any description of strongly correlated many-particle systems: trying to describe the system by simple wave functions (such as, for example, the single-determinantal states in Hartree-Fock) and taking into account important correlations becomes impossible, if one at the same time requires the solution to have the proper symmetry.

The orientation of the mean-field wave function (or, correspondingly, the single-particle density distributions and associated spin polarizations, as shown in Figs. 20 and 22 above) is arbitrary, and mean-field wave functions $\psi_{MF}(\mathbf{r},\theta)$ rotated by different angles θ are all equivalent solutions. This degeneracy can be used to improve the wave function by projection techniques, as pointed out by Peierls and Yoccoz (1957) and Peierls and Thouless (1962). The symmetry-violating mean-field wave functions and their corresponding single-particle densities can be interpreted as "intrinsic" states. States with different angular momenta projected from this intrinsic state form a rotational band. These issues were first discussed in nuclear physics in the case of open-shell nuclei, in which the assumption of a nonspherical shape was found essential for a description of nuclear spectra in terms of rotations (Bohr and Mottelson, 1953, 1975; see also the recent reviews by Butler and Nazarewicz, 1996, and Frauendorf, 2001).

We show in Secs. IV.C and IV.D that such broken-symmetry states in quantum dots can be identified by an analysis of the rotational and vibrational states (Häusler, 2000; Yannouleas and Landman, 2000a; Koskinen *et al.*, 2001) or from conditional probabilities obtained within a truncated diagonalization of the full many-body Hamiltonian (Maksym *et al.*, 2000; Reimann *et al.*, 2000; Yannouleas and Landman, 2000a).

A similar discussion will be taken up again in Sec. VI, where broken symmetry states in the electronic structure of quantum dots in large magnetic fields are discussed.

C. Mean-field versus exact diagonalization

Let us now look at the results of a numerical diagonalization of the many-body Hamiltonian, Eq. (5) for a circular, parabolic quantum dot. [Similar exact diagonalization studies for deformed dots by Ezaki *et al.* (1998a, 1998b) were discussed in Sec. III.H.] Unfortunately, nowadays numerical resources restrict us to relatively high densities and small electron numbers. (The maximum values of r_s and N for which a convergence of the

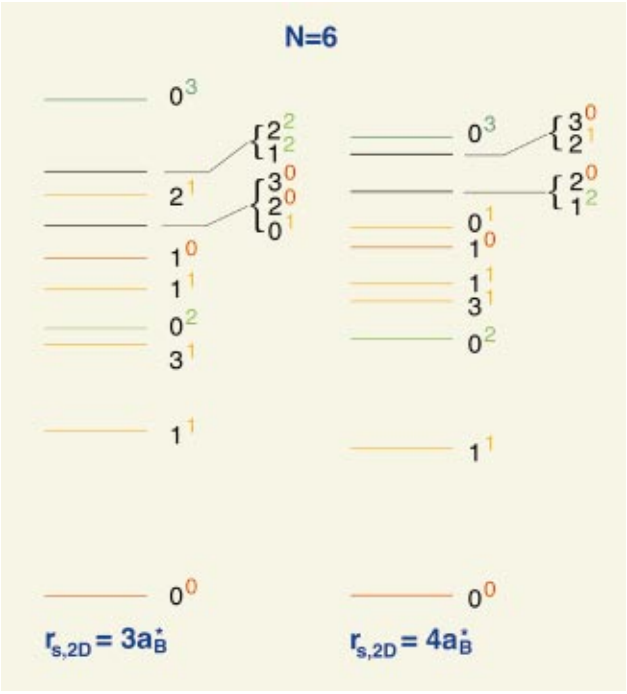

FIG. 23. Sequence of lowest many-body states for a quantum dot with $N=6$ electrons at $r_s=3a_B^*$ and $r_s=4a_B^*$, obtained from a configuration-interaction calculation. Angular momentum and spin are indicated by the labels L^S. The energy difference between the $S=0$ ground state and the polarized state with $S=3$ amounts to 126 mRy* at $r_s=3a_B^*$ and 52 mRy* at $r_s=4a_B^*$ [Color].

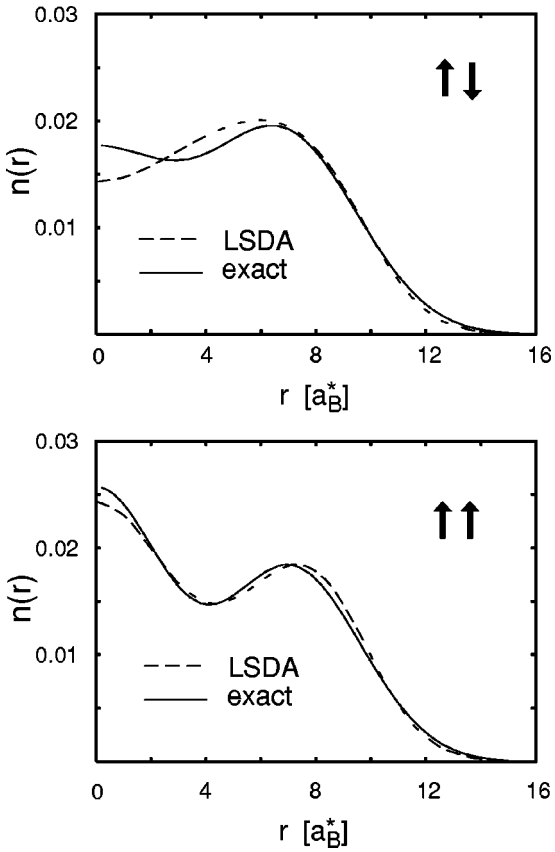

FIG. 24. Density profile of ground state (S=0; upper panel) and polarized state ($S=3$; lower panel) for a six-electron quantum dot at $r_s=4a_B^*$. The dashed line shows the corresponding LSDA result. From Reimann *et al.*, 2000.

many-body spectrum could still be reached were $r_s \leqslant 4a_B^*$ and $N=6$.) Figure 23 shows the lowest many-body states, each labeled by its angular momentum and spin, for a quantum dot confining six electrons for density parameters $r_s=3a_B^*$ and $r_s=4a_B^*$ (Reimann *et al.*, 2000). The ground state has $S=0$. The fully polarized state with $S=3$ lies at much higher energies, and many states are found in between these two configurations. A systematic analysis of the evolution of the energy difference between the spin-polarized state with $S=3$ and the $S=0$ ground state did not indicate any crossing between the energies of these states unless r_s became significantly larger than $4a_B^*$. An extrapolation of the configuration-interaction energies to higher r_s values supported the result of Egger *et al.* (1999) that the ground state of a six-electron dot is not polarized for $r_s<8a_B^*$.

Previously reported LSDA results give a surprisingly accurate estimate for the energy difference between the fully polarized and the nonmagnetic state. Although LSDA suffers from the self-interaction problem, it could correctly reproduce the nonmagnetic state as the ground state. The density of the configuration-interaction results is shown in Fig. 24 for the ground state with $S=0$ and the polarized state $S=3$, plotted along the dot radius. (The LSDA densities are included for comparison.) Being an azimuthal average, the density profile in the polarized case with the maximum at the center can be identified with the C_{5v} symmetry of the classical Wigner molecule. This polarized state lies higher in energy than the $S=0$ ground state, which shows a minimum in the dot center, pointing to a sixfold symmetry in which all particles are localized at the perimeter of the dot.

Yannouleas and Landman (1999) studied the formation of Wigner molecules in a six-electron dot within the unrestricted Hartree-Fock approximation, which (like the unrestricted SDFT formalism discussed previously) allows for internal symmetry breaking and shows the electron localization directly in the electron density. They found that, in contrast to LSDA and exact results, for $r_s \approx 4a_B^*$ the ground state has $S=3$ and the density exhibits the same geometry as classical electrons in a harmonic trap (i.e., a fivefold ring with one electron in the center). The $S=0$ state had the classical geometry of a deformed hexagon, but was higher in energy. While the unrestricted Hartree-Fock approach in some cases might reveal the internal structure of a quantum state, it is well known that it often fails to give the correct ground state (Pfannkuche, Gudmundsson, and Maksym, 1993). Reusch, Häusler, and Grabert (2001) reconsidered the Hartree-Fock studies of Yannouleas and Landman. For strong correlation the densities indeed are azimuthally modulated for an even number of electrons. However, within unrestricted Hartree-Fock the density was still found to be azimuthally symmetric for an odd number of electrons.

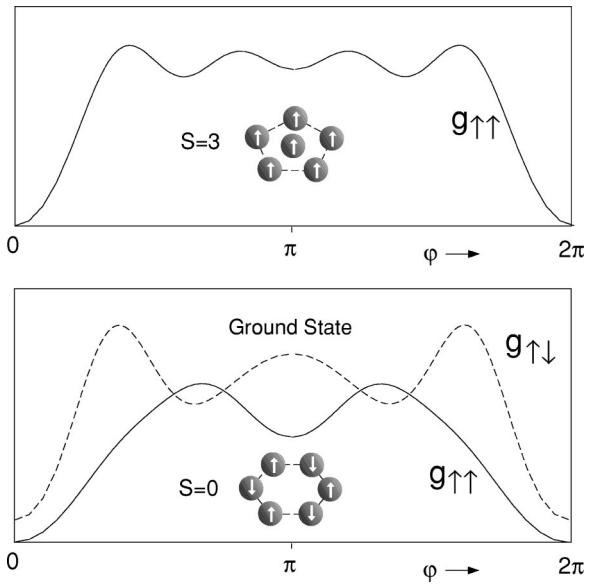

FIG. 25. Pair-correlation functions $g_{\uparrow\downarrow}(\varphi)$ and $g_{\uparrow\uparrow}(\varphi)$ for $N=6$ and $r_s=4a_B^*$, calculated at the outer maxima of the density distribution (see Fig. 25), as a function of the angle φ. Upper panel, excited state, $S=3$; lower panel, ground state, $S=0$. From Reimann *et al.*, 2000.

Let us finally look at the pair-correlation function to map out the internal symmetry of the "exact" many-body wave function. In polar coordinates, the pair correlation is defined as

$$g_{\uparrow\sigma}(\phi)=\langle \hat{n}_{\uparrow}(r,0)\hat{n}_{\sigma}(r,\phi)\rangle \tag{13}$$

and describes the probability of finding a (spin-up or spin-down) particle at (r,ϕ), if another particle (with spin up) is placed at $(r,0)$. Taking for r the radius of maximum density and varying ϕ, Fig. 25 shows for $N=6$ the quantities $g_{\uparrow\downarrow}(\phi)$ and $g_{\uparrow\uparrow}(\phi)$ for both the configuration-interaction ground state and the polarized state at $r_s=4a_B^*$. Clearly the $S=0$ state has symmetry C_{6v} and antiferromagnetic spin ordering, much like the spin-density-wave states discussed in Sec. IV.B.2 above. The fully polarized case shows four maxima in $g_{\uparrow\uparrow}(\phi)$, corresponding to C_{5v} symmetry. We note that the geometrically unrestricted Kohn-Sham formalism tends to overestimate the r_s values at which (for a given N) spontaneous symmetry breaking (spin- and/or charge-density waves) can occur in the internal structure of the wave function. For $r_s=4a_B^*$ the converged Kohn-Sham densities are azimuthally symmetric, with no signs of antiferromagnetic order. The onset of the spin-density wave at a critical density is indeed an artifact of the LSDA: In the full many-body state, the antiferromagnetic order is seen in the pair-correlation function prior to the LSDA transition point (Koskinen *et al.*, 1997; Reimann *et al.*, 2000).

We noted above that in the classical case for $N\leqslant 5$, all particles are located on a single geometrical shell, and only one possible stable configuration exists. For a dot and ring confining four electrons, for example, this corresponds to a square with the electrons localized at its corners. Figure 26 compares the rotational spectra (see also Sec. IV.D). The low-lying rotational bands are in both cases very similar and are consistent with electron localization, as explained in the next section. The only difference between the dot and the ring is that for the four-electron dot, at $L=4$ the spins of the two lowest states have opposite order from that at $L=0$. This may result from the possibility of radial oscillations in the dot, which are inhibited in the ring. Within the configuration-interaction approach, the ground state of the four-electron quantum dot remains $S=1$ at least up to $r_s=6a_B^*$. This contradicts the result of Chengguang *et al.* (1996), who obtained a ground-state spin $S=0$, but it is in agreement with a quantum Monte Carlo calculation by Harju *et al.* (1999); (see also the discussion in Sec. IV.E.1).

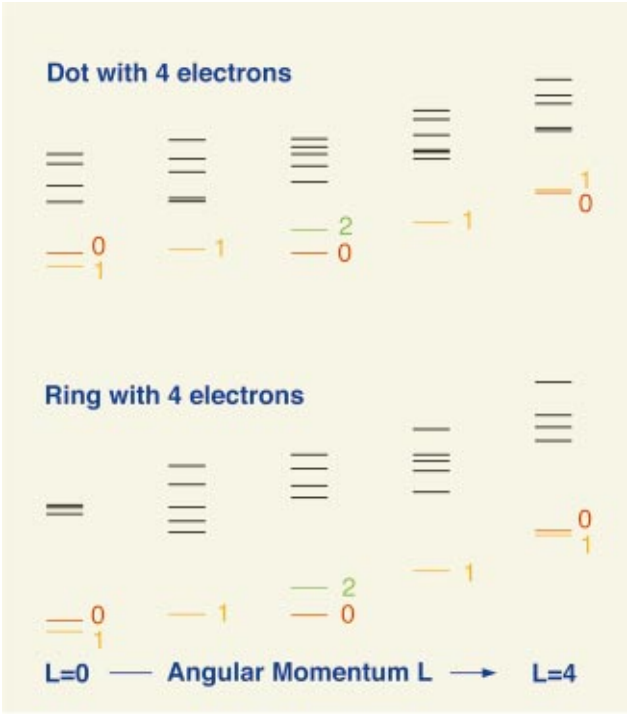

FIG. 26. Rotational spectra (low-lying states) for (upper panel) a quantum dot confining four electrons ($r_s=4a_B^*$) and (lower panel) a ring ($r_s=2a_B^*$ and $C_F=10$), each confining four electrons (see text). The spin S is given for the low-lying states (as also indicated by different colors of the levels). The energies are rescaled for comparison; the energy difference between the yrast states for $L=0$ and $L=4$ is for the dot 69 mRy* and for the ring 287 mRy*, respectively. After Manninen, Koskinen, *et al.*, 2001 [Color].

D. Quasi-one-dimensional systems

1. One-dimensional square well

By using numerical diagonalization including the spin degree of freedom, Häusler and Kramer (1993) and Jauregui, Häusler, and Kramer (1993) investigated the spectral properties and density distribution of up to $N=4$ electrons in a finite-length one-dimensional square-well

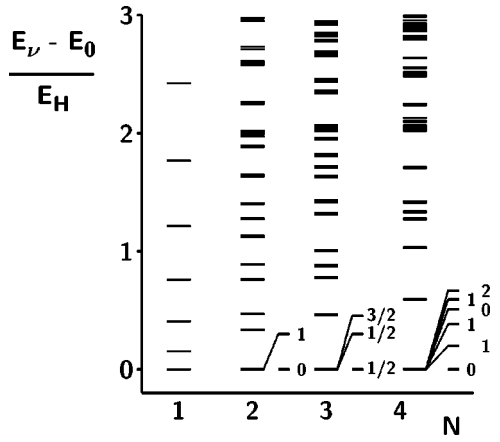

FIG. 27. Many-body spectra of a linear quantum dot with $N \leqslant 4$ and length $l = 9.45a_B^*$. The lowest multiplets are magnified and indicate the total spin of each level. From Häusler and Kramer, 1993.

potential. The electron-electron interaction potential was approximated by $V(x,x') \propto 1/\sqrt{(x-x')^2+\lambda_\perp^2}$, for larger distances reproducing the usual long-range Coulomb form. The parameter $\lambda_\perp$ measures the width of the wave function in the transverse direction. Häusler and Kramer chose $\lambda_\perp / l \ll 1$ (where l is the length of the wire). Typical spectra for $N<4$ are shown in Fig. 27. One observes that at strong correlations, groups of multiplets are formed, the total number of states within each multiplet being 2^N, corresponding to the dimensionality of the spin space. The energy splitting within a multiplet is much smaller than the energy differences between the multiplets. The near degeneracy of the states in a multiplet can be understood if one bears in mind that in a Wigner crystal the spin orientation of the crystallized electrons becomes irrelevant. Indeed, looking at the total charge density of the system, which is plotted in Fig. 28 for $N=3$ as an example, at $l \geqslant 9.5a_B^*$ one observes three distinct peaks, forming a Wigner-crystal-like configuration with the single electrons being equidistantly separated to minimize the Coulomb energy. Surprisingly, this picture was found to hold down to rather small values of l, i.e., large densities. Pronounced oscillations are observed even when the mean electron separation was of the order of a_B^* (see, for example, the density distribution for $l = 1.9a_B^*$ in Fig. 28).

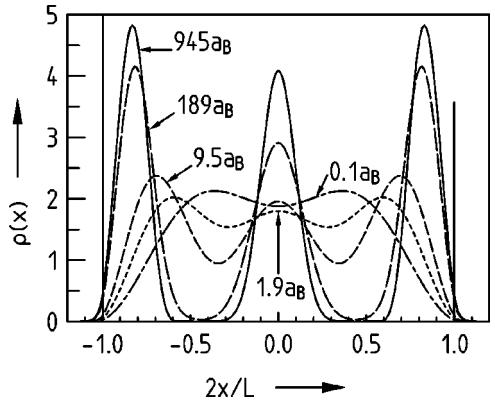

FIG. 28. Many-body densities of linear quantum dots with $N=3$ electrons for various lengths l. From Jauregui, Häusler, and Kramer, 1993.

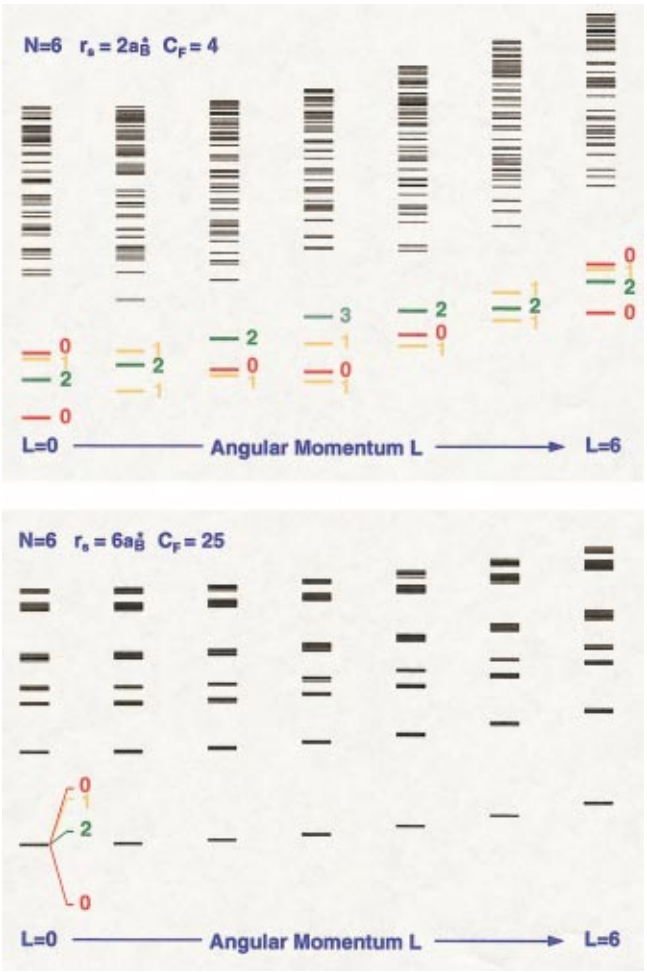

FIG. 29. Many-body spectra of a quantum ring with $N=6$ electrons. The spin S is given for the low-lying states (as also indicated by different colors of the levels). Upper panel, $r_s = 2a_B^*$ and $C_F = 4$. The energy difference between the yrast states for $L=0$ and $L=6$ is 286 mRy*. Lower panel, $r_s = 6$ and $C_F = 25$. The seven lowest vibrational bands are shown. The $L=0$ levels are shown in a magnified scale; the energy ratios are the same as for the much wider ring shown in the upper panel. From Koskinen *et al.*, 2001 [Color].

2. Quasi-one-dimensional quantum rings

The formation of Wigner molecules in quasi-one-dimensional systems was also studied for quantum rings, as discussed in Sec. IV.B.2 above in connection with the density-functional approach in the local spin-density approximation. By applying the configuration-interaction method to a quantum ring confining $N=6$ electrons at a one-dimensional density corresponding to $r_s = 2a_B^*$ and $C_F = 4$ [where $\hbar\omega = C_F \hbar^2 \pi^2 / (32 m^* r_s^2)$; see Eq. (11) for the definition of ω] one obtains for fixed angular momentum L a set of many-body eigenstates, as displayed in Fig. 29, with each state characterized by its angular

momentum and the total spin S. The lowest energy at a given angular momentum L defines the *yrast line*, a term that was originally introduced in nuclear physics and comes from the Swedish word "yrast" for "the most dizzy." From Fig. 29 we observe that a band of low-lying states close to the yrast line is separated from the states at higher energies by a sizable energy gap. One further notices a sixfold periodicity in angular momentum: the lowest levels at $L=0, 1$, and 2 have the same total spin and level spacing as the levels corresponding to $L=6, 5$, and 4, respectively. An analysis of these sequences by group-theoretical methods pointed to a moleculelike structure of rigidly arranged electrons with underlying antiferromagnetic spin order in the rotational ground state. One can describe the eigenenergies in a similar way to the spectra of a planar, polygonal molecule composed of N identical spin-1/2 atoms (Herzberg, 1945) with an effective Hamiltonian

$$H_{\text{eff}}=\frac{L^2}{2I}+\sum_a \hbar\omega_a n_a+J\sum_{i,j}^{N} \mathbf{S}_i\cdot\mathbf{S}_j \tag{14}$$

in terms of independent rotation, vibration, and the intrinsic spin degrees of freedom. The first term describes rigid rotations of a ring of electrons with a moment of inertia I; the second describes the vibrational modes. The third term is an antiferromagnetic Heisenberg Hamiltonian of localized electrons with nearest-neighbor coupling J. It was found that the whole rotational spectrum close to the yrast line can be determined by such a spin model combined with a rigid center-of-mass rotation (Koskinen *et al.*, 2001). If the ring is made much narrower, the higher vibrational states separate to individual bands. The energy differences agree well with a classical model of six vibrating electrons. The lowest band is the vibrational ground state and consists of the rotational levels. The different spin levels become almost degenerate, as localization reaches a degree at which the spin-spin interactions become less important. These results agree well with the observations of Häusler and Kramer (1993) and Jauregui, Häusler, and Kramer (1993) in the linear case described above.

Jefferson and Häusler (1997) suggested a "pocket-state" analysis in the spirit of the Hubbard model. They noted that an effective Heisenberg model with antiferromagnetic exchange and a low-spin ground state (Lieb and Mattis, 1962) was obtained in the one-dimensional case.

The ground-state antiferromagnetic order, as clearly observed in the rotational spectra, was actually predicted by density-functional studies within the local spin-density approximation, where a strong spin-density-wave state occurred in the ground state (see Fig. 22 in Sec. IV.B.2). We have already noted from the simple mean-field picture in LSDA, that low-lying excitations most likely will be collective in nature. The above many-body spectra and their one-to-one comparison to a Heisenberg model (Koskinen *et al.*, 2001) confirm that, indeed, the LSDA can to a surprisingly large degree correctly map out the internal symmetry of the many-body ground state.

E. Quantum Monte Carlo studies

Three different quantum Monte Carlo methods have been applied to the study of electronic structure in small circular quantum dots: variational Monte Carlo, path-integral Monte Carlo, and diffusion Monte Carlo. A common difficulty in applying Monte Carlo methods to fermionic systems lies in preserving the proper antisymmetry of the wave function. In the variational Monte Carlo method, the many-body ground state is approximated by a suitably chosen variational wave function with a large number of parameters. The Monte Carlo method is then used to perform multidimensional integrals and to find the set of parameters minimizing the total energy. The advantage of the method is that the Pauli exclusion principle can be taken into account by building antisymmetry into the variational wave function, usually consisting of a Jastrow factor for the two-body correlations (Bolton, 1994b; Harju *et al.*, 1999). In diffusion Monte Carlo the lowest energy state is projected from an antisymmetric trial wave function in keeping the nodal structure fixed (the fixed-node approximation; Pederiva *et al.*, 2000). Path-integral Monte Carlo applies the path-integral description of quantum mechanics and uses, for example, blocking algorithms (Mak *et al.*, 1998) to keep the solution antisymmetric. This method was used in electronic structure calculations for small quantum dots by Egger *et al.* (1999) and Harting *et al.* (2000).

1. Hund's rule

The results of the Monte Carlo methods generally agree with those obtained by other many-body methods. However, recent studies have pointed to a disturbing difference for a four-electron dot: using diffusion Monte Carlo, two independent groups (Bolton 1994b, 1996; Pederiva *et al.*, 2000) have found that the ground state has spin zero, i.e., it violates Hund's first rule. This result was also reported by Harting *et al.* (2000) based on a path-integral Monte Carlo study. However, Harju *et al.* (1999), using variational Monte Carlo, and Egger *et al.* (1999) using path-integral Monte Carlo both find $S=1$ for the ground state according to Hund's rule. Configuration-interaction calculations (Manninen, Koskinen, *et al.*, 2001) predicted that the $S=1$ state would be below the $S=0$ state regardless of r_s (from 0 up to 6). Häusler (2000) generalized the "pocket-state method" (Hüller and Kroll, 1975; Häusler, 1994) for the low-density regime of quantum dots. This model also confirmed the $S=1$ ground state.

Although the energy difference is small, the number of electrons in this case is so small that an essentially exact energy can be obtained even for such small r_s values. Moreover, the low-energy rotational spectrum is nearly identical to that obtained for a four-electron ring (Fig. 26). We conclude that the exact many-body state of four electrons in a quantum dot indeed obeys Hund's first rule and the gound state has $S=1$. The diffusion Monte Carlo method with fixed-node approximation was not able to predict the correct ground state.

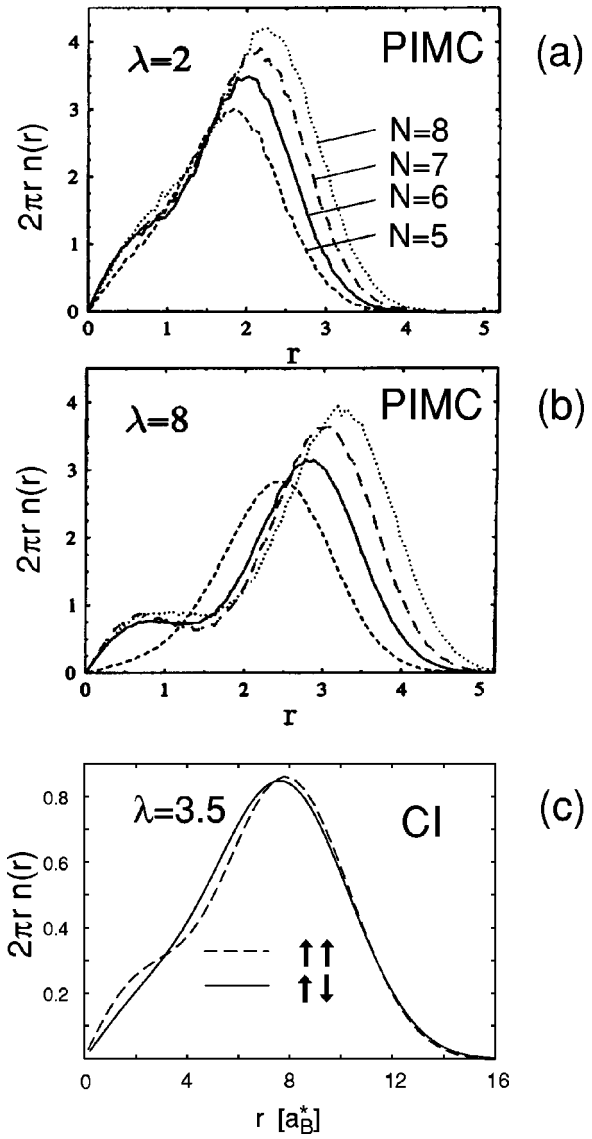

FIG. 30. Density profiles of quantum dots confining a small number of particles, as obtained from path-integral Monte Carlo simulations (after Egger *et al.*, 1999) for different values of $\lambda=\ell_0/a_B^*$. The densities are multiplied by a factor $2\pi r$. The configuration-interaction (CI) results (Reimann *et al.*, 2000) for $N=6$ at $r_s=4a_B^*$ with $S=0$ and $S=3$, corresponding to $\lambda=3.52$, are plotted in (c) for comparison. Here we use the symbol n for the electron density, while Egger *et al.* used ρ.

2. Wigner crystallization

Quantum Monte Carlo methods have also been applied to studies of Wigner crystallization in circular quantum dots and quantum rings. Egger *et al.* (1999) performed path-integral Monte Carlo calculations that also indicate the beginning formation of spatial shell structure at rather high densities.

Figure 30 compares the density profiles for the ratios of oscillator length ℓ_0 to Bohr radius $\lambda=\ell_0/a_B^*=2$ and $\lambda=8$ (Egger *et al.*, 1999) to the configuration-interaction result (Reimann *et al.*, 2000), for both the lowest $S=0$ and the $S=3$ state for $N=6$ at $\lambda=3.52$ [where Eq. (11) was used to obtain ℓ_0]. The densities are multiplied by a factor of $2\pi r$, so that a maximum in the center (see Fig. 24 above) now appears as a broad shoulder [Fig. 30(b)] towards the dot center.

As expected from the classical configurations, no such shoulder is seen for $N\leqslant 5$. The particles are located on a single shell even at large densities. With increasing λ, the onset of shell formation can be seen clearly. As predicted by the classical model (see. Fig. 19), a second geometrical shell is formed for $N>5$. For $N=6$, for weak correlations Egger *et al.* (1999) report a ground-state spin zero, while at about $\lambda=8$ a transition to a $S=1$ state forms. In the configuration-interaction result, which was calculated at a density intermediate between the two values reported by Egger *et al.*, the "shoulder" visible in Fig. 30(a), pointing to a (5,1) geometric shell structure (i.e., a C_{5v} symmetry with one particle at the center), is not seen in the $S=0$ ground state.

We conclude from the above comparison that although some signals for the formation of geometric shells can be identified at rather small values of $r_s\approx 4a_B^*$, the sequence of geometries in ground and excited states still can be rather different from that of a truly classical picture. In addition, for values below $r_s=4a_B^*$ and $N>5$, in the configuration-interaction spectra no clear signals for rotational spectra were identified, which could indicate a truly crystallized ground state. For $N\leqslant 5$, however, where only one classical configuration is seen, for densities as large as $r_s=2a_B^*$ the low-lying spectra could be well understood by assuming a regular Wigner molecule for the internal structure of the wave function and analyzing its rotational structure (see the discussion of the four-electron quantum dot above).

Filinov, Bonitz, and Lozovik (2001) studied the distribution of closed electron paths obtained by the path-integral Monte Carlo technique. They found that if the kinetic energy is small as compared to the electron-electron interaction, the internal structure of the state is a Wigner molecule consistent with the classical geometry discussed in Sec. IV.A. Increasing the interaction causes "orientational melting" of the molecule. By analyzing the angular and distance fluctuations, Filinov *et al.* (2001) determined that the onset of Wigner crystallization happens only at $r_s\approx 60$ ($n=10,\ldots,20$) and that the orientational ordering occurs only at even larger values of r_s. These results seem to contradict the above-mentioned results of small values of r_s at which Wigner crystallization occurred in a few-electron system. However, the analyzing method is different and at this point a direct comparison of these two approaches could not be made.

V. MAGNETIC FIELDS: ADDITION ENERGY SPECTRA AND A SINGLE-PARTICLE APPROACH

The electronic structure of quantum dots in magnetic fields displays a rich scenario of different phases in the ground state. An overwhelming amount of literature on this topic has been published, mostly concerning exact diagonalization studies and mean-field approaches. Different milestones were set by measurements of the

magnetic-field dependence of the addition energy spectra (McEuen *et al.*, 1991, 1992; Ashoori, Störmer, *et al.*, 1992, 1993; Tarucha *et al.*, 1996; Austing, Tokura, *et al.*, 1999; Oosterkamp *et al.*, 1999), and by the discovery of spin-singlet-triplet oscillations (Wagner, Merkt, and Chaplik, 1992) and the polarization transition with subsequent formation of the maximum-density droplet and its reconstruction (MacDonald, Yang, and Johnson, 1993; de Chamon and Wen, 1994).

A. Harmonic oscillator in a magnetic field

When studying the field-free case we saw earlier that the harmonic oscillator is a realistic potential for a quantum dot. As a first simple approach, let us now consider N particles in a harmonic trap with a homogeneous magnetic field in the z direction, $\mathbf{B}=(0,0,B)$, and ignore the interactions between the particles for the moment.

1. Fock-Darwin spectrum and Landau bands

The single-particle spectrum of a two-dimensional harmonic oscillator in a homogeneous magnetic field was discussed by Fock (1928) and Darwin (1930) in the early days of quantum mechanics (see also Landau, 1930). The Fock-Darwin energy spectra have been rederived in many recent articles and monographs (see, for example, Jacak, Hawrylak, and Wójs, 1998; Chakraborty, 1999). Nevertheless, we shall briefly repeat this discussion here, as the Fock-Darwin model forms an essential and simple analytic concept for the analysis of single-particle effects in quantum dots and furthermore provides the basis for more sophisticated many-body calculations when the interactions between the particles are taken into account.

For parabolic confinement with circular symmetry and a homogeneous magnetic field with $\mathbf{A}=(1/2)B(-y,x,0)$ in symmetric gauge the single-particle Hamiltonian equals

$$H_{sp}=\frac{\mathbf{p}^2}{2m^*}+\frac{1}{2}m^*\left(\omega^2+\frac{1}{4}\omega_c^2\right)r^2+\frac{1}{2}\omega_c l_z, \tag{15}$$

with the cyclotron frequency $\omega_c=eB/m^*c$ and l_z being the z component of the angular momentum operator. The single-particle spectrum at fixed magnetic field is given by

$$\varepsilon_{nm}=\hbar\omega_h(2n+|m|+1)+\frac{1}{2}\hbar\omega_c m, \tag{16}$$

where $n=0,1,2,3,\ldots$ is the radial and $m=0,\pm1,\pm2,\pm3,\ldots$ is the azimuthal quantum number. The effective length scale is given by the effective oscillator length $\ell_h=\sqrt{\hbar/m\omega_h}$ with $\omega_h^2=\omega^2+\omega_c^2/4$. The evolution of the single-particle energies ε_{nm} with magnetic field is illustrated schematically in Fig. 31. We note that the spectrum is very similar to that of a deformed oscillator (cf. Fig. 2).

In the Fock-Darwin spectrum displayed in Fig. 31, for $B\gtrsim0$ energy levels with positive or negative m move up or down in energy as they have magnetic moments pointing opposite or along the magnetic field. At large

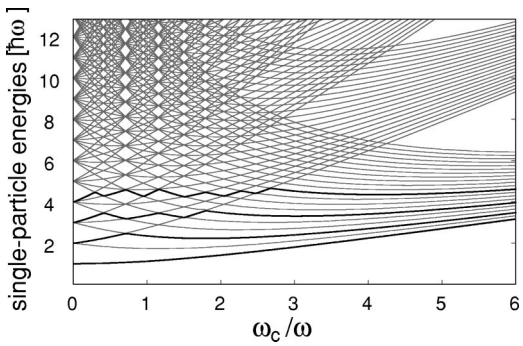

FIG. 31. Fock-Darwin energy spectra as a function of ω_c/ω. The bold lines indicate the addition energies for $N=2$, 6, 12, and 20 independent particles. (Note that some states with larger m values were omitted in order to make the formation of Landau bands in strong fields more visible.)

fields, free-electron behavior prevails over the confinement of the oscillator and the energy levels form a sequence of so-called *Landau bands*. From the spectrum in Fig. 31 we clearly see that at high magnetic fields it is energetically favorable to populate only the lowest states sequentially with single-particle angular momenta $m=0,-1,-2,\ldots,-(N-1)$, and the energy is increasing monotonically with B. (We note that in the lowest Landau band, the sign of m is frequently omitted to simplify the notation. In the following, we shall use this convention.)

The pronounced shell structure at zero magnetic fields is reduced in a magnetic field $B>0$ until for integer ratios of $\omega_+:\omega_-$ (where $\omega_\pm=\omega_h\pm1/2\,\omega_c$) accidental degeneracies occur, again leading to enhanced bunching of single-particle levels, as seen in Fig. 31 at $\omega_c/\omega=1/\sqrt{2},2/\sqrt{3},3/2$, etc. In the limit $\omega_c/\omega\to\infty$, the eigenvalues asymptotically approach the degenerate Landau levels $\hbar\omega_c(N_L+1/2)$ with Landau level index $N_L=0,1,2,\ldots$.

The strength of the magnetic field is often described in terms of the *filling factor* ν, which in an infinite system is the number of filled Landau levels (considering spin-up and spin-down states to be different levels). In a quantum dot, for $\nu=2$ the states $m=0,1,\ldots,(N/2-1)$ are doubly occupied, while $\nu=1$ is a spin-polarized state with $m=0,1,\ldots,(N-1)$ singly occupied. [For the definition of fractal filling factors for $\nu<1$, see Eq. (17).]

2. Constant-interaction model

In relatively weak magnetic fields and for small r_s, the ground-state properties of typical GaAs-AlGaAs quantum dots confining a smaller number of electrons can be described in the simple single-particle picture to a good degree of approximation. We argued in Sec. II.B that the addition energy to put the Nth electron in the dot can be approximated in a simple model where we still treat the electrons as independent particles, but add a constant charging energy e^2/C, as it costs energy to place the Nth electron in a dot already confining $N-1$ electrons

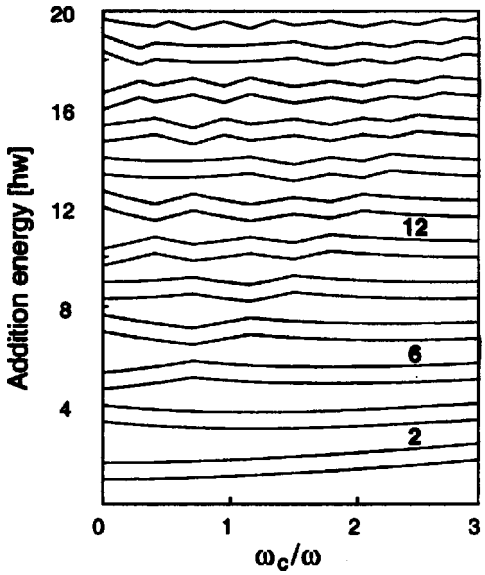

FIG. 32. Addition energies in the constant-interaction model (a charging energy $e^2/C=\frac{2}{3}\hbar\omega$ was assumed).

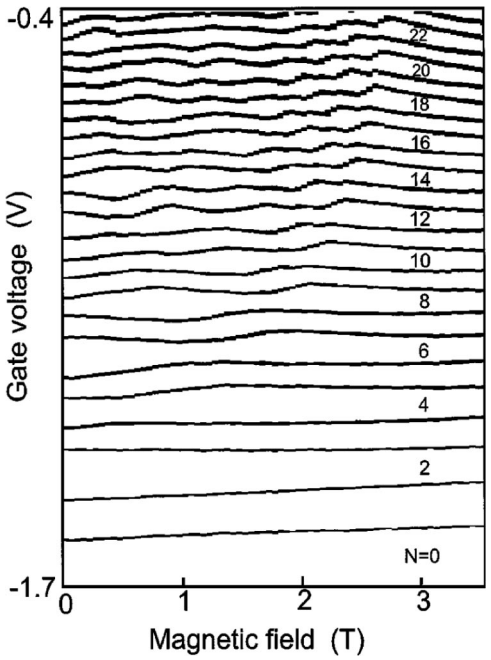

FIG. 33. Evolution of the peak positions (voltages) of the Coulomb blockade oscillations with magnetic field. The large gaps for closed shells with $N=2$, 6, and 12 at $B=0$ are clearly seen. The particle numbers N are indicated at each of the Coulomb peaks. From Tarucha *et al.*, 1996.

(McEuen *et al.*, 1991; Tarucha *et al.*, 1996; Kouwenhoven, Austing, and Tarucha, 2001).

For an even number of electrons, assuming spin degeneracy and neglecting the Zeeman energy, the Nth electron occupies the same orbital as the $(N-1)$th electron. Then only the charging energy is needed for the electron to tunnel into the dot. Figure 32 shows the addition energy spectra obtained in this way, plotted as a function of magnetic field. A constant charging energy $e^2/C=2/3\hbar\omega$ was assumed. One clearly recognizes a "wiggling" in the single addition energy curves and additional subshell closings at nonzero B, originating from the level crossings in the Fock-Darwin spectrum (Fig. 31). For fixed N, above a certain field strength only single-particle states belonging to the lowest Landau band become occupied (here with spin degeneracy). No more level crossings occur, and the addition energy increases smoothly with B.

Let us now see how far our simple model can reach in providing an understanding of the experimentally determined $B-N$ dependence of the addition energies.

B. Measurements of addition energy spectra

1. Tunneling spectroscopy of vertical dots

Tarucha *et al.* (1996) measured the Coulomb blockade spectra of a vertical quantum dot (see. Figs. 3 and 10) as a function of a magnetic field applied perpendicular to the dot plane (i.e., parallel to the tunneling current). The development of the current peak positions [being proportional to the addition energy $\mu(N)=E(N+1)-E(N)$; see Sec. II.B] with increasing B is displayed in Fig. 33. Just as predicted by the constant-interaction model (Fig. 32), one observes that the lowest curves depend smoothly on B, while the peak positions that are higher in addition energy show pronounced "wiggles," the number of which increases with the number of confined electrons. One also notices that the current peaks shift in pairs with B until they get out of phase just before the wiggling stops at a certain field strength and the Coulomb blockade curves for all dot sizes N show a very smooth B dependence.

In the simple Fock-Darwin single-particle model for a quantum dot in a magnetic field, we saw that level crossings occur as the magnetic field is increased (Fig. 31). Such level crossings then appear as cusps in the addition energies of the constant-interaction model, as shown in Fig. 32. We can identify these cusps with the wiggles in the small-B range in the experimental data, and, indeed, the constant-interaction model can reproduce many of the observed features. On an enlarged scale, the current peaks for $3\leqslant N\leqslant 6$ are shown in Fig. 34 (Tarucha *et al.*, 1996). Below 0.4 T, one observes a rearrangement of the pairing between (otherwise neighbored) current peaks, which can be interpreted in terms of Hund's first rule, favoring spin alignment at midshell. As a first and simple approach, Tarucha *et al.* (1996) incorporated the spin alignment into the constant-interaction model by introducing a constant energy shift due to exchange interactions between electrons with parallel spins. They obtained remarkable agreement with the experimental data (see the comparison given in Fig. 34): at $B=0$, $\mu(4)$ is decreased due to the energy gain by spin alignment (the spin configuration is illustrated by the pictorial diagram), while correspondingly $\mu(5)$ is increased as only one unpaired spin occupies the highest single-particle orbital. As the magnetic field splits the degeneracy of oscillator states with quantum numbers $(n,\pm m)$, at a certain field strength the spin flips back to a paired con-

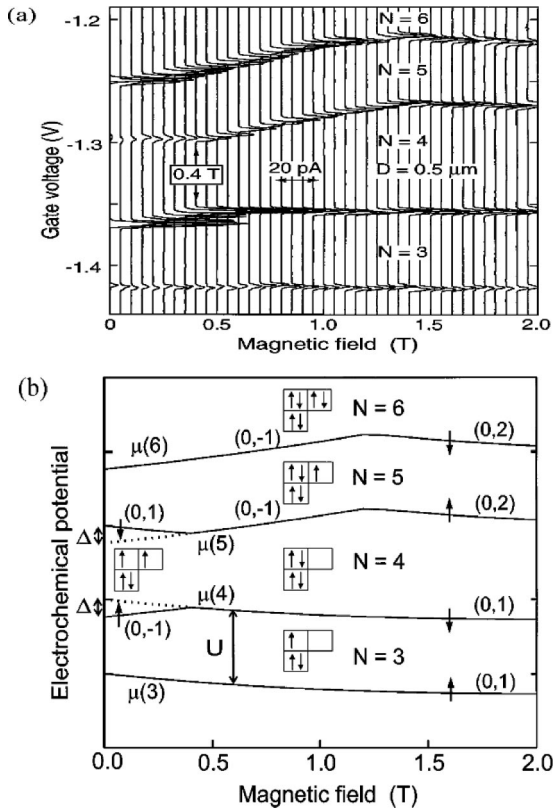

FIG. 34. Hund's rule in quantum dots. (a) Current peaks as in Fig. 33 above, on an enlarged scale for $N=3$, 4, 5, and 6; (b) constant-interaction model, taking into account exchange effects. The energy splitting Δ accounts for the energy gain by spin alignment, following Hund's rule for orbital degeneracy at $B=0$. From Tarucha *et al.*, 1996.

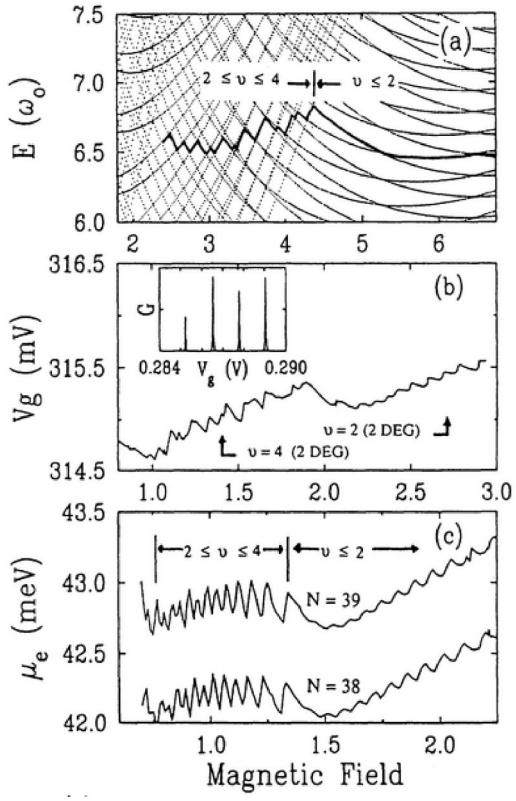

FIG. 35. Effect of magnetic field on level spectrum and conductance: (a) Noninteracting level spectrum as a function of magnetic field B in units ω_c/ω, taking into account a constant charging energy and a Zeeman term. The solid line indicates the total energy for $N=39$ electrons as an example. (b) Experimental conductance peak position as a function of B (in T) at $T\approx 30$ mK. (c) Chemical potential obtained from a semiclassical self-consistent model. From McEuen *et al.*, 1992.

figuration. Note, however, that "accidental" degeneracies occur for $B>0$, which may also lead to spin alignment at finite fields (see Sec. VII.C).

2. Gated transport spectroscopy in magnetic fields

An early report on gated transport spectroscopy of artificial atoms in a magnetic field was given by McEuen *et al.* in 1991. With increasing B or, equivalently, a decreasing number of occupied Landau bands, they observed regular oscillations in the conductance peaks. These were associated with the properties of the quantized single-particle spectra, resulting from changes in the occupation of the two lowest Landau bands.

In analogy to Figs. 31 and 32 above, Fig. 35(a) shows the noninteracting level spectrum as a function of B, but now also taking into account a constant charging energy and a Zeeman term $g^*\mu_B B S_z$ with an effective g factor g^*. Note that the bare electron mass enters μ_B. Thus $g^*\mu_B B \ll \hbar\omega_c$ in contrast to free electrons, in which both magnitudes are almost equal. The total energy is indicated by the solid line for $N=39$ electrons as an example (from McEuen *et al.*, 1992). Very few level crossings are found for $\nu \lesssim 2$. This is in obvious disagreement with the frequent and rather regular oscillations observed in the experimental data [shown in Fig. 35(b)]. The failure of the single-particle picture is not too surprising, as stronger fields effectively increase the interaction between the electrons, and many-body effects lead to significant deviations.

For filling factors between $\nu=2$ and $\nu=1$, McEuen *et al.* (1992, 1993) developed a semiclassical self-consistent model for the charge distribution in the dot. In the spirit of the Thomas-Fermi model, they approximated the kinetic-energy contribution to the energy functional by its bulk value. The finite z extent of the dot was taken into account by a modified electron-electron interaction. A self-consistent minimization of the total energy yielded an electrochemical potential $\mu(N)$, which appeared in reasonable agreement with the experimental data [see Fig. 35(c)]. McEuen *et al.* noted that an incompressible ring separates a compressible dot center from a compressible edge. With increasing field, electrons transfer from the center region to states with opposite spin in the lowest Landau band at the edge, leading to $N/2$ wiggles in the conductance peak positions as a function of B. Level crossings for $\nu \lesssim 2$ occur whenever a flux quantum is added. Then one more electron flips its spin and can be accommodated in the lowest Landau band.

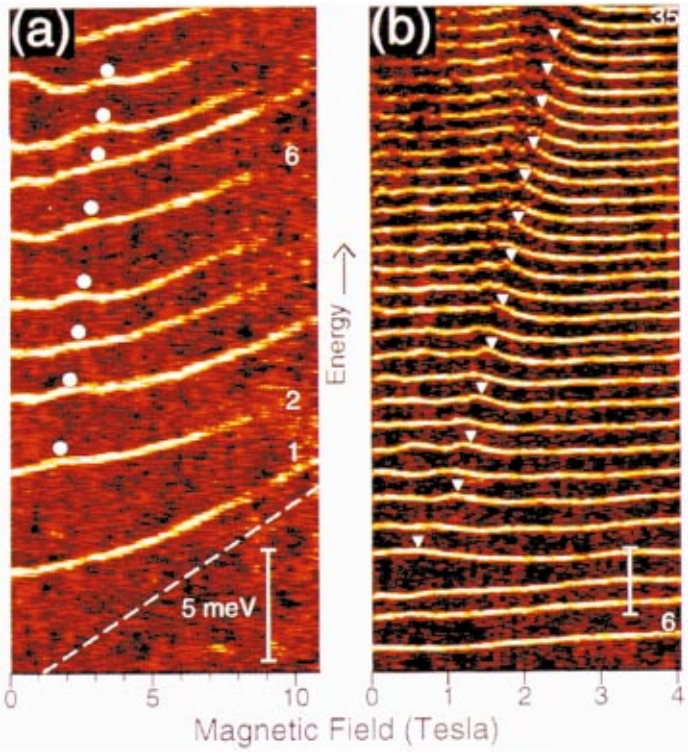

FIG. 36. Color scale plot of the B-N diagram from single-electron capacitance spectroscopy (from Ashoori *et al.*, 1993) for (a) $N<10$ and (b) $6\leqslant N\leqslant 35$. The vertical axis is proportional to the gate voltage, i.e., the energy scale of electron addition. White, red, and black regions correspond to highest, intermediate, and lowest capacitance. (a) Dots mark the singlet-triplet transitions. (b) Triangles mark the filling factor $\nu=2$ [Color].

The magnetic-field dependence of the Coulomb blockade spectra was recently measured by Ciorga *et al.* (2000) for small lateral quantum dots (see. Sec. II.C.1). Removing the charging energy in the addition energy spectrum, they obtained a B-N phase diagram with similarities to the spectra shown above, although a direct comparison appeared difficult.

3. B-N phase diagram obtained by single-electron capacitance spectroscopy

Ashoori *et al.* (1993; Ashoori, 1996) used single-electron capacitance spectroscopy (as briefly discussed earlier in Sec. II.C.2) to systematically measure ground-state energies and their magnetic-field dependence for a single quantum dot confining up to 35 electrons. The B-field evolution of the ground-state energies for $N<35$ is shown in Fig. 36.

Trivially, the single-electron state [Eq. (16), with the Zeeman energy added] increases with magnetic field due to the enhancement of the effective confinement. The two-electron case, however, shows a kink at $B\approx 1.5$ T. This kink can be understood from a spin flip of one of the electrons, such that the state changes from a singlet to a triplet. Su *et al.* (1994) observed such an effect for $N=2$ in single-electron tunneling measurements. It was noticed by Wagner, Merkt, and Chaplik (1992; see also Maksym and Chakraborty, 1992) that it is actually the Coulomb interaction between the particles, rather than the Zeeman effect alone, that leads to these spin-singlet-triplet oscillations with magnetic field. For larger N, the data of Ashoori *et al.* show kinks similar to that associated with singlet-triplet transition for $N=2$ (marked by the white dots). These kinks shift to higher fields as N increases. They are related to the flipping of the last electron moment in line with the magnetic field (Palacios *et al.*, 1994; Ashoori, 1996).

In larger dots at lower densities, a bunching pattern in the addition spectrum was observed, indicating that two or more successive electrons could enter the dot at nearly the same energy. A strong magnetic field created a sharp boundary between paired and unpaired regions in the electron addition spectrum (Ashoori, Störmer, *et al.*, 1992; Zhitenev *et al.*, 1997, 1999). It was surmised that the bunching was caused by electron localization in the low-density droplet, splitting it into smaller fragments caused by disorder and electron-electron interactions (localization-delocalization transition). Further experimental studies of an artificially disordered dot consisting of two potential minima separated by a barrier (i.e., a quantum dot molecule, as further discussed in Sec. IX.D) supported this interpretation (Brodsky *et al.*, 2000). A similar phenomenon was discussed by Canali (2000), who numerically investigated the addition energy spectra of quantum dots in the presence of disorder and associated the observed pairing with electron tunneling into the distinct fragments of the droplet.

4. B-N phase diagram of large vertical quantum dots

Oosterkamp *et al.* (1999) systematically extended the measurements of the B-N phase diagram by Ashoori *et al.* (1993) and Klein *et al.* (1995) to stronger fields and larger sizes. They used a vertical quantum dot as described by Tarucha *et al.* (1996). The positions of the Coulomb blockade peaks as a function of magnetic field are displayed in Fig. 37.

While the low-field limit could be well understood in the constant-interaction model, in stronger magnetic fields features are observed which can be associated with many-body effects as a consequence of enhanced correlations. The dotted line in Fig. 37 marks the B value at which all electrons occupy spin-degenerate states corresponding to $\nu=2$, i.e., the value at which the ground state has total spin $S=0$ and angular momentum $N(N-2)/4$ (Austing, Sasaki, *et al.*, 1999; Austing, Tokura, *et al.*, 1999). Beyond $\nu=2$, as discussed previously, electrons successively flip the spin and move to the dot edge, filling empty states with higher angular momenta. Consequently the polarization of the dot starts at the dot edge and continues inwards, until the dot is fully polarized. (A similar edge polarization is also obtained in quantum wires; see Dempsey, Gelfand, and Halperin, 1993.)

In the data by Oosterkamp *et al.* (1999), the overall appearance of the spin flips and their number is found to

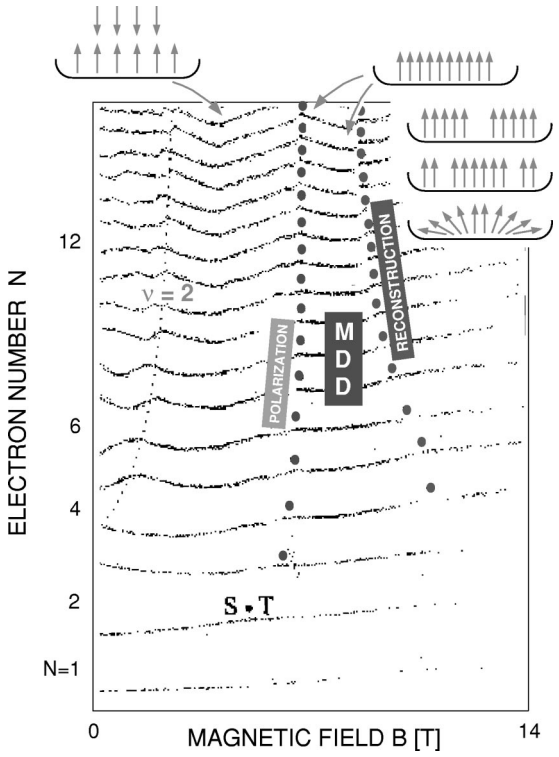

FIG. 37. Coulomb blockade peak positions as a function of magnetic field. The beginning and end of the maximum-density droplet (MDD) phase is marked by a dot. Different mechanisms for reconstruction of the maximum-density droplet in high magnetic fields (Secs. VI and VII), such as formation of a spin-polarized Chamon-Wen edge, reconstruction from the dot center, or spin textures, are indicated schematically. After Oosterkamp *et al.*, 1999.

be somewhat different from that in the planar dots investigated by McEuen *et al.* (1992, 1993). In Fig. 37 the solid dot labeled S-T marks the singlet-triplet transition for $N=2$. For $N>2$ the dots mark the polarization transition, where the last spin flip has occurred.

After complete polarization of the electron droplet, the particles occupy neighboring orbitals with angular momenta $m=0,1,2,\ldots,(N-1)$, belonging to the lowest Landau band with filling factor $\nu=1$. The exchange energy results in the formation of a compact and stable configuration, the *maximum-density droplet* (MacDonald, Yang, and Johnson, 1993); see Sec. VI. A further increase in the magnetic field continuously squeezes the compact electron droplet until the Coulomb interaction between the particles forces the maximum-density droplet to rearrange. At $\nu<1$, different scenarios for the reconstruction of the maximum-density droplet (i.e., a redistribution of the charge and/or the spins) are possible, depending on the relative strength of confinement and the Hartree energy, the Zeeman energy, and exchange and correlation effects. Suggested mechanisms for such a reconstruction include a charge redistribution either by creating holes in the center (MacDonald, Yang, and Johnson, 1993) or by splitting off a ring of electrons (de Chamon and Wen, 1994). Formation of spin textures in quantum dots was also discussed (Oaknin *et al.*, 1997; Heinonen, Kinaret, and Johnson, 1999). Theoretical concepts to describe the different phases of quantum dots in high magnetic fields mostly have involved exact diagonalization studies in the small-N limit, but also have included mean-field approaches such as (restricted and unrestricted) Hartree-Fock methods or current-density-functional theory for larger N. These approaches and their results will be summarized in the following sections.

VI. ROLE OF ELECTRON-ELECTRON INTERACTIONS IN MAGNETIC FIELDS

A. Exact diagonalization for parabolic dots in magnetic fields

We saw above that the single-particle Hamiltonian for a harmonic confinement, in the presence of a magnetic field, is exactly solvable (Fock, 1928; Darwin, 1930). For two interacting electrons, separating out the center-of-mass coordinate leads to an exact analytic solution (Dineykhan and Nazmitdinov, 1997), but this procedure is impractical when the number of electrons is larger. Performing configuration-interaction calculations or exact diagonalization (see Sec. III.A), it is then natural to use, as well, the Fock-Darwin states for the basis in the interacting case. At weak magnetic fields the single-particle basis must include states for both spins and several Landau bands. This makes the convergence of the many-body spectra very slow with respect to the number of included configurations. Full convergence can be obtained only if the particle number is small, typically much less than $N=10$ (Maksym and Chakraborty, 1992; Eto, 1997; Reimann *et al.*, 2000). The slow convergence is related to the fact that, for large N, the single-particle spectrum approaches the continuous spectrum of the infinite electron gas (Koskinen *et al.*, 1994). In the strong-magnetic-field limit, where the electron system is fully polarized, the configuration-interaction problem becomes easier due to the large reduction of configuration space. Often one can keep the number of configurations small by restricting the basis to the lowest Landau band. In any case, however, the basis size needed to obtain convergence of the many-body spectra increases rapidly for increasing particle number and magnetic field, or for decreasing average electron density, so that these microscopic approaches could be followed only for a very limited range of system parameters.

The relative simplicity of the exact diagonalization technique resulted in a vast literature. A rich scenario with many unexpected properties was revealed (as, for example, the nonmonotonic increase of spin and the magic orbital angular momentum values; see Maksym, 1996; Eto, 1997, 1999; Wójs and Hawrylak, 1997).

Exact diagonalization calculations for dots in magnetic fields were first performed for $N\leqslant 10$ in the spin-polarized case by Maksym and Chakraborty (1990). Quantum dots confining two and three electrons were studied by Pfannkuche, Gerhardts, *et al.* (1993) and Pfannkuche, Gudmundsson, and Maksym (1993) as well

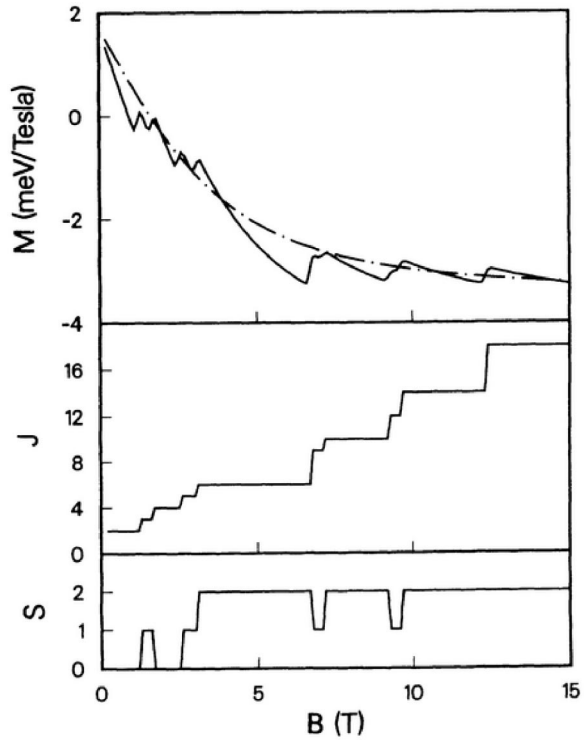

FIG. 38. Effects of magnetic field according to the exact diagonalization method: top panel, ground-state magnetization M; middle panel, total orbital angular momentum J; lower panel, total spin S for a four-electron dot as a function of magnetic field. From Maksym and Chakraborty, 1992. Note that here the authors used J instead of L for the total angular momentum.

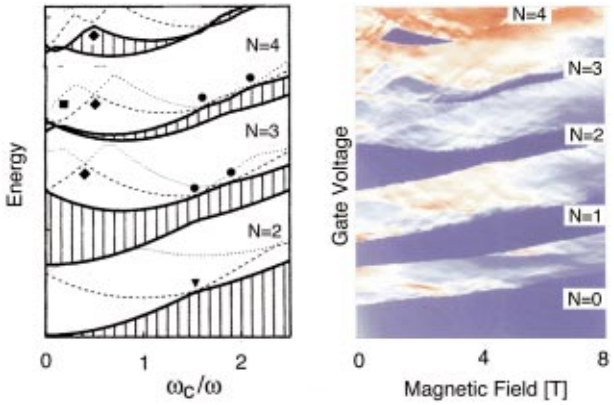

FIG. 39. Addition energies of small dots in magnetic fields: Left, addition energy spectra obtained by exact diagonalization for $2<N<5$ ($\hbar\omega=5$ meV, GaAs), shown for the ground state (solid line) and the first two excited states (dashed lines). The different symbols indicate transitions in the ground state. Right: current as a function of gate voltage and magnetic field, measured in the nonlinear regime. The ground state as well as the lowest excited states can contribute to the current. It is large (>10 pA) in the red regions and small (<0.1 pA) in the blue regions. The dark blue regions indicate Coulomb blockade, corresponding to the hatched regions in the configuration-interaction spectra (left). After Kouwenhoven, Oosterkamp, *et al.*, 1997 [Color].

as by Hawrylak and Pfannkuche (1993). Yang, McDonald, and Johnson (1993), Palacios *et al.* (1994), Tejedor *et al.*, (1994), and Eto (1997, 1999) used this method to systematically calculate the addition energies. At smaller magnetic fields, oscillations in the addition energy as a function of B were identified with different "phases." At filling factor $\nu\approx1$, the smooth evolution of the addition energy was brought into connection with the stability of the maximum-density droplet. Quantum dots at fractional filling $\nu<1$ have also been much studied in connection with edge phenomena in quantum Hall states (see, for example Palacios *et al.*, 1993, 1994; Yang, MacDonald, and Johnson, 1993; de Chamon and Wen, 1994; Oaknin *et al.*, 1995).

Maksym and Chakraborty (1990, 1992) studied the magnetism of dots confining three or four electrons as a function of the magnetic field. They observed that while the orbital angular momentum increases monotonically with the field, the spin does not. The four-electron case is shown in Fig. 38.

When the field increases from zero, the state first has $L=2$, $S=0$ (note that at zero field $L=0$ and $S=1$). In this state the Zeeman splitting is so small that both up and down electrons fill a similar maximum-density droplet and consequently we can associate it with filling factor $\nu=2$. Increasing the field causes transitions between different spin and angular momentum states until a stable region with $S=2$ and $L=6$ persists in a wider range of magnetic fields. This state is the spin-polarized maximum-density droplet with $\nu=1$. Wagner, Merkt, and Chaplik (1992) studied the magnetization and spin transitions in a two-electron dot. For larger dots with up to ten electrons, transitions between the nonpolarized compact state at $\nu=2$ and the fully polarized maximum-density droplet ($\nu=1$) were analyzed by Wójs and Hawrylak (1997). They found periodic oscillations of the spin as a function of the magnetic field until the $\nu=1$ state was reached. This was caused by an interplay between a maximization of spin and the formation of *compact configurations*, in which each spin component fills a maximum-density droplet of different size. We should note that Wójs and Hawrylak used only the lowest Landau band in the basis set. However, even in the maximum-density droplet ($\nu=1$) the higher Landau bands have an important contribution to the electron-electron correlation. In real systems the completely polarized state with $\nu=1$ (our definition of the maximum-density droplet) is reached at a field strength at which mixing with higher Landau bands is important (Palacios *et al.*, 1994). In the limit of an infinitely strong magnetic field, the Hartree-Fock approximation becomes exact for the maximum-density droplet (MacDonald *et al.*, 1993).

For dots containing up to five electrons, Eto (1999) calculated the addition energies for both the ground state and the first two excited states. Figure 39 (left) shows the addition energies as a function of magnetic field (expressed as the ratio of the cyclotron frequency ω_c to the confinement frequency ω).

Experimentally, the transitions between the different many-body states can be seen in the addition energies

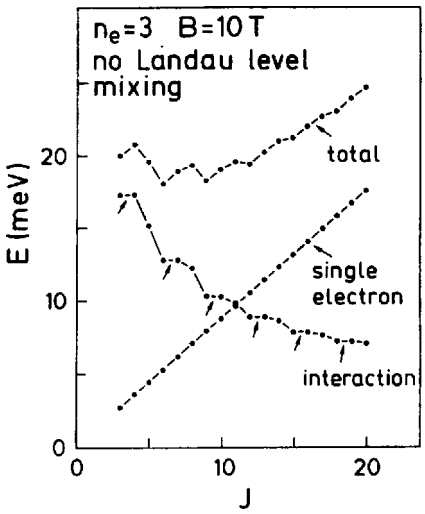

FIG. 40. Single-electron energy, interaction energy, and the total energy for a three-electron quantum dot at $B=10$ T and $\hbar\omega=4$ meV (for GaAs). After Maksym and Chakraborty, 1990. As in Fig. 38, here J labels the total angular momentum.

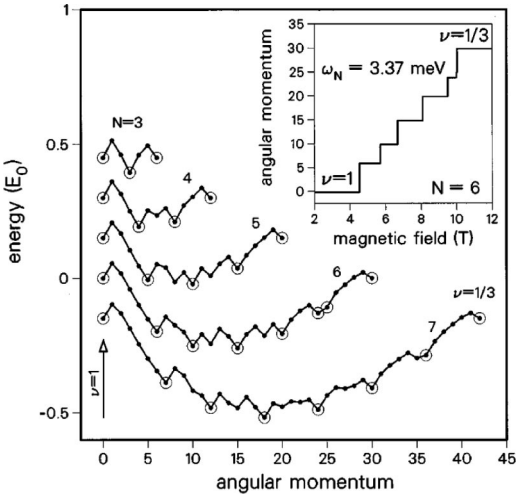

FIG. 41. Ground-state energy as a function of angular momentum for $N=3,\ldots,7$ electrons, obtained by exact diagonalization. The angular momentum is shifted so that $L=0$ corresponds to the maximum-density droplet (see text). The inset shows the dependence of the angular momentum on the magnetic field in the case of six electrons. From Wójs and Hawrylak, 1997.

obtained by conductance spectroscopy. If the transport window $-eV_{sd}$ is large (i.e., in the nonlinear regime; see Sec. II.B), so that the current is nonzero over a wider range of gate voltages, instead of single Coulomb peaks one observes the stripes shown in Fig. 39 (right). Kouwenhoven, Oosterkamp, *et al.* (1997) give a detailed comparison between the experimental data and the exact diagonalization study and argue that excited states can be identified with the pronounced curves inside these stripes.

Maksym and Chakraborty (1990, 1992) studied in detail the interplay between the single-particle orbital energies and the interaction energy and showed how it resulted in a nonmonotonic increase of the total angular momentum as a function of the field.

Figure 40 shows the single-electron energy of the Fock-Darwin states (linear in L) and the interaction contribution for a three-electron quantum dot, obtained by exact diagonalization of the many-body Hamiltonian. The interaction energy decreases with L as the occupation of orbitals with higher angular momentum reduces the Coulomb interaction. The total energy shows downward cusps at angular momentum values $L=3,6,9,12$, etc. [In a four-electron system, the corresponding cusps would occur at $L=6,10,14$, etc., as indicated by the plateaus of $J(B)$ in Fig. 38.] The strength of the magnetic field determines the angular momentum at which the total energy minimum occurs. At high fields, this minimum coincides with a cusp. Maksym and Chakraborty (1990) concluded that the ground state in a magnetic field occurs only at certain values of angular momentum, which they called "magic" (again pointing to the enhanced stability). As the magnetic field is varied, transitions from one magic angular momentum to another occur.

The usual way to define the filling factor in a finite quantum dot for $\nu\lesssim 1$ is

$$\nu=\frac{N(N-1)}{(2L)}. \tag{17}$$

Maksym and Chakraborty converted the magic angular momenta to such effective filling factors [Eq. (17)] and found a sequence 1,1/2,1/3,1/4, etc. in the case of three particles. (However, this simple sequence holds only in this particular case. If $N>3$, the effective filling factors are those familiar from the fractional quantum Hall effect: 1/3,1/5,1/7, etc.) Figure 41 shows the ground-state energy as a function of the angular momentum in a strong magnetic field for particle numbers $3\leqslant N\leqslant 7$ (Wójs and Hawrylak, 1997). Up to $N=5$ the period of magic L values is equal to N. These periods originate from rigid rotations of the classical configuration of electrons (Maksym, 1996; Maksym *et al.*, 2000), in analogy to what we discussed earlier for the rotational-vibrational spectra of quantum rings (see Sec. IV.B.2). The case $N=6$ is more complicated due to the interplay between two stable classical geometries. Ruan *et al.* (1995) and Bao (1997) used general symmetry arguments applied to the nodal structure of the wave function to explain the origin of these magic angular momenta.

As a probe of the many-body effects, heat capacity and magnetization measurements were suggested, also taking into account the spin degree of freedom at lower magnetic fields (Maksym and Chakraborty, 1992).

At this point, we should add that drastic truncations of Hilbert space, like those obtained for example by assuming spin polarization or restricting the basis to the lowest Landau band, seem to be reasonable in the high-field case. In the transition regions, however, such approximations might not be valid, as can be seen in Fig. 38, where a spin reduction is still observed at a filling factor $\nu\approx 0.4$.

B. Electron localization in strong magnetic fields

1. Laughlin wave function

In a strong magnetic field the electrons in a quantum dot will be spin polarized and eventually reach a state related to the incompressible quantum fluid of the fractional quantum Hall effect. For a filling factor $\nu=1/q$ (with $q\geqslant 3$) this state can be approximated by the Laughlin wave function (Laughlin, 1983)

$$\psi_L(q)=\prod_{i<j}(z_i-z_j)^q \exp\left(-\frac{1}{4}\sum_k |z_k|^2\right), \tag{18}$$

where coordinates are expressed as complex numbers $z=x+iy$, and the normalization is omitted. In the following we examine the relation of exact solutions of small electron systems to Laughlin-type wave functions.

If $q=1$ ($\nu=1$), the product in Eq. (18) forms a Slater determinant of single-particle levels with angular momenta ranging from 0 to $N-1$ (N being the number of electrons). This follows from the fact that, in a harmonic confinement, in the lowest Landau band the single-particle states with angular momentum m are $z^m \exp(-|z|^2/4)$ (these correspond to the Fock-Darwin states discussed earlier). The role of the external confinement is only to change the single-particle frequency to $\omega_h=\sqrt{\omega^2+\omega_c^2/4}$. The Laughlin state, Eq. (18), with $q=1$ is similar to the Hartree-Fock approximation of the maximum-density droplet. This state has total angular momentum $L_1=N(N-1)/2$.

The total angular momentum of the ground state depends on the magnetic field. The Laughlin state with $q=3$ becomes an estimate of the ground state when $L_3=3N(N-1)/2$. In such a high magnetic field the single-particle states of the higher Landau bands have been pushed up in energy and a good approximation is to assume that the exact ground state consists only of configurations of the lowest Landau band. Indeed, several studies have shown that the overlap of the $\psi_L(3)$ with the exact ground state is close to 1 in finite systems, more than 0.99 when $N<10$ (Laughlin, 1983; Jain and Kawamura, 1995; Seki *et al.*, 1996; Manninen, Viefers, *et al.*, 2001).

Johnson (1992) studied an exactly solvable model with r^2 interaction between the electrons and showed that in this case the exact wave functions are generalizations of the Laughlin state.

2. Close to the Laughlin state

For N electrons confined in an isotropic harmonic potential, the Laughlin wave function has angular momentum $L_q=qN(N-1)/2$. The lowest energy states for angular momenta above L_q can be composed by multiplying the Laughlin wave function with a symmetric polynomial. The order of the polynomial with respect to z determines the change in the angular momentum. Every power of z increases the angular momentum by 1. For L_q+1 the only symmetric polynomial is $\Sigma_i z_i=Nz_0$, where z_0 is the center-of-mass coordinate. Indeed, exact configuration-interaction calculations confirm that the lowest energy state with $L=L_q+1$ is within numerical accuracy a center-of-mass excitation, the excitation energy being $\hbar\omega_h$ (Trugman and Kivelson, 1985; Jain and Kawamura, 1995; Maksym, 1996). The center-of-mass state cannot increase the electron-electron correlation.

Laughlin (1983) suggested that an important low-energy excitation corresponds to a fractional charge $1/q$ and can be approximated by the wave function

$$\psi_L^N(q)=\prod_i^N (z_i-z_0)\psi_L(q), \tag{19}$$

where the angular momentum is increased by the number of particles N in the finite system. For small systems this wave function gives a good overlap with the exact solution (Laughlin, 1983). In the case of a finite quantum dot the fractionally charged excitation corresponds to angular momentum $L=L_q+N$. For intermediate angular momenta $L=L_q+n$ ($1<n<N$) one can interpolate between the wave functions $\psi_L(q)$ and $\psi_L^N(q)$ [Eqs. (18) and (19)] and multiply the Laughlin state with the polynomial

$$F_n=\sum_{i<j<\cdots<n}^{N}(z_i-z_0)(z_j-z_0)\cdots(z_n-z_0), \tag{20}$$

where the sum is used to guarantee that the polynomial is symmetric. Such a construction was suggested by Bertsch and Papenbrock (1999) for describing weakly interacting rotating Bose condensates.

In the case of $n=2$ it is easy to see that the above ansatz increases the pairwise correlation between the electrons. The polynomial can be written as

$$F_2=\sum_{i<j}(z_i-z_j)^2. \tag{21}$$

Related expansions can be carried out for larger n values. The increased correlation significantly reduces the energy as compared to the center-of-mass excitations. This can be seen in Fig. 42, where the lowest many-body states for a six-electron quantum dot are plotted as a function of the angular momentum. The spectrum is qualitatively similar after $L=15$ at $B=0.9$ T* (corresponding to $q=1$) and after $L=45$ at $B=2.5$ T* (corresponding to $q=3$). Note that the results presented in Fig. 42 are not based on the trial wave functions presented above, but are computed with the configuration-interaction method.

Jain (1989) proposed a somewhat different construction for the excited states in the fractional quantum Hall regime. Applied to finite dots, the wave function can be written as (Jain and Kawamura, 1995; Kamilla and Jain, 1995)

$$\psi_J(L)=\mathcal{P}\prod_{j<k}(z_j-z_k)^{2m}\phi_{L^*}, \tag{22}$$

where m is an integer, ϕ_{L^*} is an antisymmetric wave function of noninteracting electrons with angular momentum L^*, and $\mathcal{P}$ is a projection to the lowest Landau

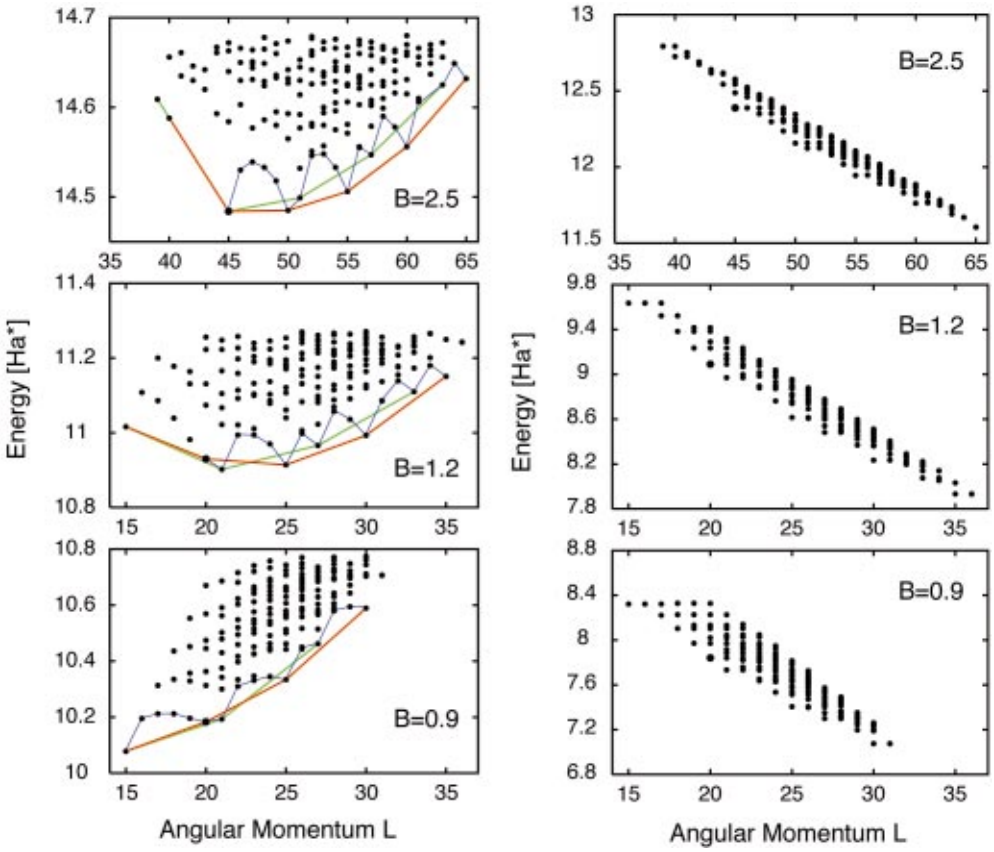

FIG. 42. Calculated many-body spectrum of a six-electron quantum dot as a function of the angular momentum for three different values of the external magnetic field, $B=0.9$ T*, 1.2 T*, and 2.5 T*, corresponding approximately to filling factors 1, 2/3, and 1/3. Using material parameters for GaAs, one effective atomic unit of the magnetic field corresponds to T*=6.68 T. The blue line marks the yrast line. The lowest energy states corresponding to a fivefold (sixfold) internal symmetry are connected with red (green) lines. The right panel shows the same many-body spectrum as in the left panel, but with the center-of-mass excitation energy $L\hbar\omega_h$ subtracted. After Manninen, Viefers, *et al.*, 2001 [Color].

level. Note that in this case the product is symmetric and the antisymmetry is provided by the noninteracting wave function.

For $L^*=L_1$ the ground state of the noninteracting electrons is just the Slater determinant $\psi_L(1)$ corresponding to the maximum-density droplet, and the wave function is equal to $\psi_L(2m+1)$, i.e., the Laughlin state with $q=2m+1$.

The Jain construction, Eq. (22), makes it possible to construct the lowest states, the yrast states (see the discussion in Sec. IV.D), for all angular momenta larger than or equal to that of the maximum-density droplet. The results are published by Jain and Kawamura (1995) and agree excellently with those of complete configuration-interaction calculations even when higher Landau bands are taken into account. This shows that the role of the higher Landau bands is only to decrease the total energy while the the lowest Landau band determines overall structure of the yrast spectrum. It was also noticed (Jain and Kawamura, 1995; Kamilla and Jain, 1995) that it is the noninteracting part of the wave function that determines the structure of the yrast line, and the correlations are taken into account similarly for all angular momenta via the Jastrow factor. Figure 42 (right) shows that the structure of the yrast line agrees with the structure predicted by the Jain construction. All the kinks of the spectrum are determined by noninteracting electrons up to $L=35$ in the case of six electrons ($L_1=15$).

Seki *et al.* (1996) studied in detail the applicability of the Jain construction in six- and seven-electron dots and found that it explains well all the magic angular momentum values.

It is important to note that the Jain construction is not limited to the states just above the maximum-density droplet, but that a similar construction can be used above the $q=3$ region. The wave function is the same [Eq. (22)], but the exponent is $m=2$. Again, above $L=L_3$ (45 for six electrons) the noninteracting electron part dominates the structure of the yrast line, as can be seen in Fig. 42, and the structure of the spectrum is very similar to that above L_1.

3. Relation to rotating Bose condensates

The rotational spectrum of polarized electrons is very similar for high magnetic fields and for large angular momenta at zero magnetic fields (Manninen, Viefers,

et al., 2001): the electrons will mainly occupy those single-particle states with the largest angular momenta in each energy shell.

The theory of rotating polarized electrons in a magnetic field is closely related to that of weakly interacting rotating Bose condensates with repulsive interaction between the atoms (Bertsch and Papenbrock, 1999; Butts and Rokshar, 1999; Cooper and Wilkin, 1999; Mottelson, 1999; Kavoulakis, Mottelson, and Pethick, 2000; Viefers, Hansson, and Reimann, 2000; Jackson *et al.*, 2001). In a 3D harmonic trap the states with high angular momenta become essentially two dimensional, as in the quantum dot. In the Bose condensates the atom-atom interaction has a very short range and is weak in the limit of a dilute gas. In this case the many-body wave function can be approximated as a linear combination of states in which all the particles belong to the lowest Landau band and the interaction between the levels is vanishingly small. The situation is then similar to that of (polarized) electrons in a quantum dot in a high magnetic field, the only difference being that electrons are fermions.

The Laughlin wave function [Eq. (18)] describes bosons if the exponent q is an even integer. The Jastrow factor tries to keep the particles apart from each other. This can be achieved in a rotating system by distributing the particles at different single-particle states. The lack of the Pauli exclusion principle does not help in the bosonic case, since the multiple occupation of single-particle states is unfavorable due to the repulsive interaction. The only difference between the fermion and boson cases is then (apart from the form of the interaction) the exponent q, which dictates the symmetry of the wave function. Similar approximations can then be used for both. The Jain wave function [Eq. (22)] can be applied for bosons by replacing the Jastrow exponent $2m$ with an odd number (Cooper and Wilkin, 1999; Viefers, Hansson, and Reimann, 2000). Since the main property of the yrast line is again dictated by the noninteracting particles, the yrast spectra should be similar. At least for small systems this is indeed the case. Trugman and Kivelson (1985) have calculated the yrast spectrum of four electrons using a short-range interaction, and Viefers, Hansson, and Reimann (2000) have studied the four-atom Bose condensate with a similar interaction (see Fig. 43). Note that $L=6$ in the case of electrons corresponds to the maximum-density droplet ($q=1$), which should be compared to $L=12$ ($q=2$) in the case of four bosons.

Bertsch and Papenbrock (1999) have suggested that the beginning of the yrast line of a weakly interacting Bose condensate is described by the polynomial F_n of Eq. (20), multiplied by the bosonic ground state. Replacing the bosonic ground state with the maximum-density droplet or the $q=3$ state and taking $n=N$, the Bertsch-Papenbrock state equals the Laughlin (1983) ansatz for the low-energy excitations (with fractional charge). As discussed before, beyond the Laughlin states the Bertsch-Papenbrock ansatz is a good approximation to the exact wave function for interacting electrons.

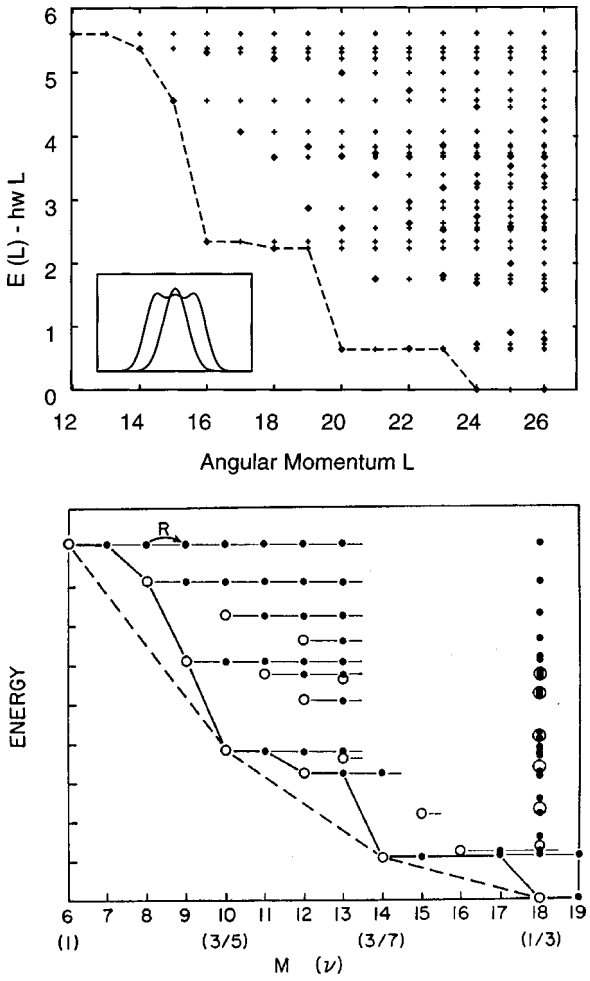

FIG. 43. The four-particle yrast spectrum: upper panel, spinless rotating Bose condensates, from Viefers, Hansson, and Reimann, 2000; lower panel, rotating polarized electrons, from Trugman and Kivelson, 1985. Both spectra are calculated using a similar short-range interaction between the particles.

4. Localization of electrons and the Laughlin state

Let us now look at electron localization in a strong magnetic field in terms of the trial wave functions. As noted earlier, the circular symmetry hides the possible localization in the laboratory frame of reference. The internal localization can be seen by looking at correlation functions or at the many-body spectrum.

Yoshioka (1984) determined the pair-correlation function in an infinite 2D electron gas with filling factor 1/3 using numerical diagonalization with periodic boundary conditions. He obtained a modulation in the pair correlation that corresponded to localization in a triangular lattice. A much stronger Wigner crystallization was obtained at filling factor 1/7 by Yang *et al.* (2001).

Maksym (1996) used the rotating-frame theory of Eckardt (1935) to study the internal correlation of few-electron systems in a strong magnetic field. The results clearly show the electron localization to Wigner crystal molecules with geometries determined by classical charged particles in quantum dots (see Sec. IV.A).

Laughlin (1983) pointed out the relation of the trial wave function [Eq. (18)] to the localization of classical

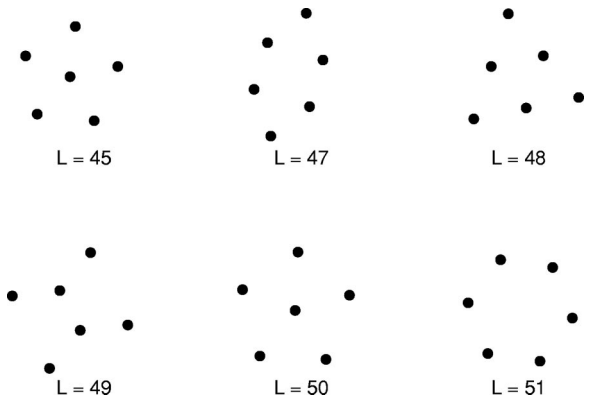

FIG. 44. Geometry of the "localized" electrons in a six-electron quantum dot determined from the maximum amplitude of the trial wave function of Eq. (20) for different values of the angular momentum.

electrons. It is easy to determine the N-particle correlation function, which is just the square of the many-body wave function. Writing this as

$$|\psi_L(q)|^2 = e^{-\Phi/q}, \tag{23}$$

determining the maximum correlation is equivalent to finding the minimum of

$$\Phi = -\sum_{i<j} 2q^2 \ln|z_i - z_j| + \frac{1}{2} q \sum_k |z_k|^2. \tag{24}$$

This is the energy of a classical one-component plasma in two dimensions, i.e., particles confined in a harmonic trap ($\omega = \sqrt{q}$) and with repulsive logarithmic interparticle interactions.

Classical electrons in a 2D harmonic confinement form Wigner molecules consisting of rings of electrons (Bedanov and Peeters, 1994), as we have seen in Sec. IV.A. In small systems the geometries are not sensitive to whether the interaction is logarithmic or $1/r$ (in large systems the number of electrons in each ring changes in some cases when going from $1/r$ to the logarithmic interaction). The geometry of the classical plasma cluster gives only the coordinates of the maximum correlation. The degree of localization can be studied, for example, by looking at the sensitivity of Φ to the position of the particles. It is easy to show that

$$\left(\frac{\partial^2}{\partial x_i^2} + \frac{\partial^2}{\partial y_i^2} \right) |\psi_L(q)|^2 = -2q|\psi_L(q)|^2. \tag{25}$$

This demonstrates that the localization of electrons increases rapidly with q, as is known from the theory of the fractional quantum Hall effect. (For a review of the quantum Hall effect see Prange and Girvin, 1990.)

Laughlin (1983) showed that a similar analysis of the trial wave function, Eq. (19), leads to a classical plasma with a phantom charge of $1/q$ at point z_0. In the case of a finite quantum dot this excitation means a vortex at the center of the dot. In the single-particle picture the Jastrow factor in Eq. (19) means that the angular momentum of each particle is increased by one. Consequently there will be no electrons at the $m=0$ state. If the classical system has an electron in the center, the geometry of this excitation will be different from that of the ground state. In the six-electron case the geometry of the $L = L_q$ state is a pentagon with one electron at the center, while the geometry of the $L = L_q + N$ state is a hexagon of six electrons, as shown in Fig. 44. Note that these internal geometries are independent of q. The polynomial of Eq. (20) combined with the Laughlin state is a good approximation to the exact wave function along the yrast line (above L_3) and can be used to analyze how the internal geometry changes with L. Figure 44 shows the geometries dictated by this assumption. The order of the polynomial ($L-45$ in this case) determines how many electrons form the outer ring.

In the de Chamon–Wen (1994) edge reconstruction, at a certain field strength a ring of electrons becomes separated from the maximum-density droplet, as discussed in Sec. VII.D. A suggestion for the Chamon-Wen edge state is $F_n \psi_L(q)$, where n is the number of electrons in the outer ring. The increase of angular momentum when the Chamon-Wen edge is formed is then simply determined by the number of electrons in the outer ring. This is in good agreement with existing calculations (Goldmann and Renn, 1999; Reimann, Koskinen, Manninen, and Mottelson, 1999). This geometrical interpretation also explains the successive formation of rings when further increasing the magnetic field. Moreover, similar low-energy excitations where rings of electrons are excited further out should also appear after each "fractional" Laughlin state ($q = 3,5,\ldots$; Manninen, Viefers, *et al.*, 2001).

5. Localization and the many-body spectrum

As discussed previously (Sec. IV.D), for quantum rings the localization of electrons was most convincingly seen by folding the exact many-body spectrum into that of a model Hamiltonian of localized electrons (Koskinen *et al.*, 2001). Similarly, the rotational spectrum of four electrons (Fig. 26) in a quantum dot (without a magnetic field) indicated localization of electrons in a square geometry. In the presence of a strong magnetic field the electron system will be fully polarized and the analysis of the rotational spectrum becomes even simpler. If the electron system were a rigid rotor the yrast spectrum would show a periodicity determined by the rotational symmetry of the Wigner molecule. In the case of four electrons only rotations with $L = 2,6,10$, etc. would be allowed (apart from center-of-mass excitations). A period of four is indeed seen clearly in Fig. 43.

In the case of six or more electrons the classical configuration can have more than one energetically close-lying stable geometry. The quantum state then also includes properties of several isomers, since the Laughlin state corresponds to a classical plasma. Consequently the many-body spectrum becomes more complicated, as pointed out by Maksym (1996). Figure 42 showed the the many-body spectra of six electrons in a quantum dot. Classically the six-electron system has two isomers that are very close in energy: a pentagon with one atom in

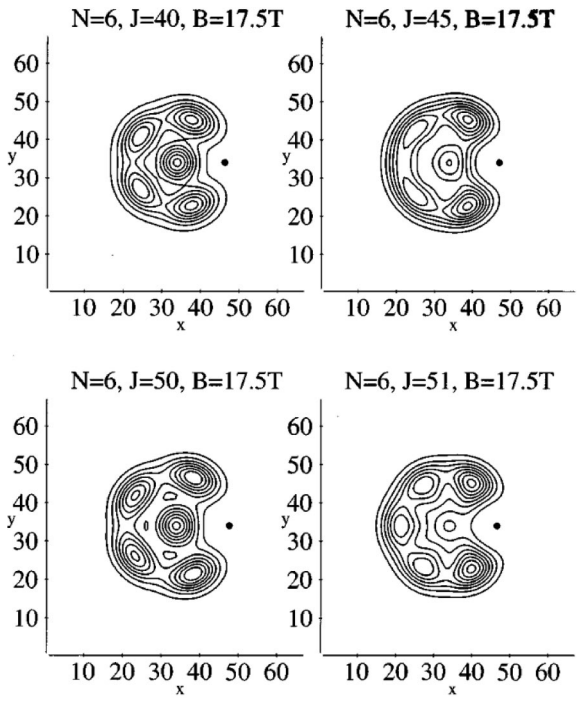

FIG. 45. Pair-correlation function for a six-electron quantum dot at different angular momenta L. The black dots mark the fixed position of one of the electrons. From Maksym, 1996.

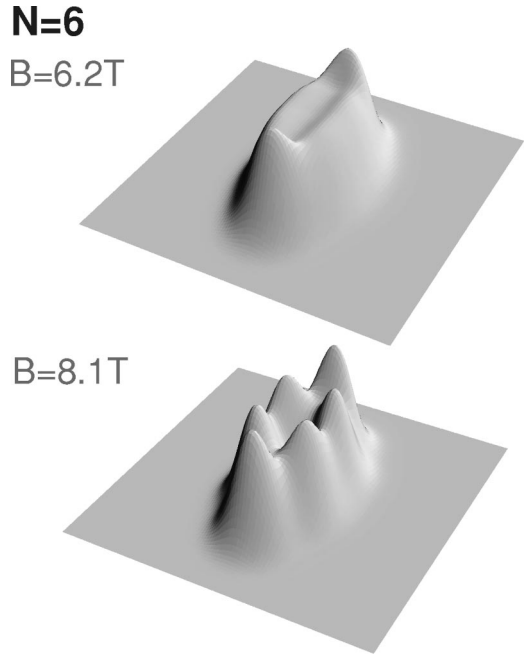

FIG. 46. Electron densities in elliptic quantum dots containing six electrons ($r_s = 1.5a_B^*$). In the upper panel the magnetic field corresponds to that of the maximum-density droplet ($B = 6.2$ T for GaAs) and in the lower panel it is increased by 30% ($B = 8.1$ T). From Manninen, Koskinen, *et al.*, 2001.

the center and a slightly deformed hexagon (see Sec. IV.A). Periods of five and six are marked in the spectra with red and green lines, respectively. Increasing the magnetic field after formation of the maximum-density droplet ($L = 15$) the next minimum occurs at $L = 21$, which is a sixfold ring. In this region of the spectrum the sixfold ring and the fivefold ring alternate at the yrast line. However, when the field is so strong that we have reached the $q = 3$ state the yrast line is dominated by the fivefold rings. The reason is the increased localization of the Laughlin state when q increases [Eq. (25)], causing the classical ground state, the fivefold ring, to be favored over the sixfold ring.

It should be possible to excite the system in such a way that only the outer Chamon-Wen ring of localized electrons is rigidly rotating. The yrast line should then show a minimum when the angular momentum is increased by the number of atoms in the outermost ring. This is the case seen in Fig. 42 for six electrons. So far no detailed many-body computations for larger dots exist in which one could definitely see these "surface excitations." The spectrum should be similar after the formation of the maximum-density droplet and after the fractional Laughlin state, but the surface excitations should be clearer after the $q \geqslant 3$ state in which the localization is stronger.

6. Correlation functions and localization

For a circular quantum dot, the exact electron density has circular symmetry in the laboratory frame of reference, as discussed earlier. This is also the case when the quantum dot is exposed to a homogeneous external magnetic field. In order to identify broken symmetries in the internal electronic structure, a rotating frame or correlation functions have to be examined.

Figure 45 (Maksym, 1996) shows the pair-correlation function for a six-electron quantum dot in a strong magnetic field corresponding to a filling factor close to the fractional quantum Hall regime ($\nu \approx 1/3$). The internal structures of fivefold and sixfold rings are clearly seen for angular momenta $L = 45$ and $L = 51$, respectively.

Goldmann and Renn (1999) observed the localization of electrons in the Chamon-Wen edge region, $\nu \lesssim 1$, for large quantum dots with $N \leqslant 40$. They used a partial diagonalization technique in which the occupancies of the deep inner orbitals of the maximum-density droplet were frozen. The exact wave function obtained in this way has 99% overlap with a trial wave function that was obtained from the angular momentum projection of a maximum-density droplet surrounded by a ring of localized electrons. The authors called this a "necklace state." Goldmann and Renn (1999) found that in a 40-electron dot the necklace has 18 maxima corresponding to the localization of 18 electrons. This is in fair agreement with the 16-electron ring obtained by Reimann, Koskinen, Manninen, and Mottelson (1999) in a dot with 42 electrons (see Sec. VII.D.1). The actual number of electrons in the outer ring could depend on the density of electrons and on the magnetic field. (In the large dots several stable configurations of localized electrons exist.)

We mentioned above that, around $\nu \approx 1$, the approximation to use only the lowest Landau band does not hold. There accurate configuration-interaction calculations require a large basis set that includes higher Lan-

dau bands and thus can be performed only for a small number of electrons ($N<10$) even though the electron system is fully polarized. In such a small system the Chamon-Wen edge of course loses its meaning and at a certain field strength all electrons localize simultaneously.

As we have seen in the case of a circular dot, localization can be studied using correlation functions, a rotating frame, or the many-body rotational spectrum. Manninen, Koskinen, *et al.* (2001) suggested another straightforward way: In an elliptic dot the external potential breaks the symmetry of the Hamiltonian in the laboratory frame of reference and makes a symmetry-broken electron density possible in the case of an exact many-body calculation. Figure 46 shows the ground-state electron densities for six electrons in an elliptic quantum dot obtained by a configuration-interaction calculation. (The current-spin-density-functional method discussed below gives very similar densities.) In a magnetic field corresponding to the maximum-density droplet, the density is uniform. When the field is increased by 30% the electrons become localized (Manninen, Koskinen, *et al.*, 2001). The result of Fig. 46 shows that, beyond the maximum-density droplet, localization can be seen directly in the electron density if the symmetry of the system is broken, while in circular symmetry the localization is seen only by studying the internal structure of the exact many-body state or by using a geometrically unrestricted, approximative mean-field theory, as discussed in the following section.

VII. DENSITY-FUNCTIONAL APPROACH FOR QUANTUM DOTS IN MAGNETIC FIELDS

Vignale and Rasolt (1987, 1988) developed an extension of density-functional theory that makes it possible to include gauge fields in the energy functional. This formalism has been widely used to describe the electronic structure and addition energy spectra of quantum dots in magnetic fields (Ferconi and Vignale, 1994, 1997; Lipparini *et al.*, 1997; Steffens, Rössler, and Suhrke, 1998; Steffens, Suhrke, and Rössler, 1998a, 1998b; Koskinen *et al.*, 1999; Reimann, Koskinen, Manninen, and Mottelson, 1999; Steffens and Suhrke, 1999; Ullrich and Vignale, 2000).

A. Current-spin-density-functional theory

In addition to the parabolic confinement $V(\mathbf{r})$ of a quantum dot with N electrons, we again consider a magnetic field $\mathbf{B}=B\mathbf{e}_z$ applied perpendicular to the x-y plane. The vector field $\mathbf{A}(\mathbf{r})=B/2(-y,x)$ adds extra terms to the energy functional (special care is needed for implementing the local-density approximation; we comment on this problem in Sec. VII.B):

$$\begin{aligned} E[\phi_{i\sigma}] = & \sum_{i\delta} f_{i\sigma}\left\langle \phi_{i\sigma}\left| -\frac{\hbar^2\nabla^2}{2m^*}\right|\phi_{i\sigma}\right\rangle \\ & + \frac{1}{2}\frac{e^2}{4\pi\epsilon_0\epsilon}\int\int d\mathbf{r}\,d\mathbf{r}'\frac{n(\mathbf{r})n(\mathbf{r}')}{|\mathbf{r}-\mathbf{r}'|} \\ & + \int d\mathbf{r}\,n(\mathbf{r})V(\mathbf{r}) \\ & + \int d\mathbf{r}\,n(\mathbf{r})e_{\rm xc}[n_\sigma(\mathbf{r}),\gamma(\mathbf{r})] \\ & + \frac{1}{2}g^*\mu_B B\int d\mathbf{r}[n_\uparrow(\mathbf{r})-n_\downarrow(\mathbf{r})] \\ & + e\int d\mathbf{r}\,\mathbf{j}_p(\mathbf{r})\cdot\mathbf{A}(\mathbf{r}) + \frac{e^2}{2m^*}\int d\mathbf{r}\,n(\mathbf{r})A(\mathbf{r})^2. \end{aligned} \tag{26}$$

Here e is the (absolute) electron charge, g^* is a reduced Landé g factor, and μ_B is the Bohr magneton. The paramagnetic current density $\mathbf{j}_p(\mathbf{r})$ is defined as

$$\begin{aligned} \mathbf{j}_p(\mathbf{r}) = & -\frac{i\hbar}{2m^*}\sum_{i\sigma} f_{i\sigma}[\phi^*_{i\sigma}(\mathbf{r})\nabla\phi_{i\sigma}(\mathbf{r}) \\ & -\phi_{i\sigma}(\mathbf{r})\nabla\phi^*_{i\sigma}(\mathbf{r})] \end{aligned} \tag{27}$$

with thermal occupation numbers

$$f_{i,\sigma}=\frac{1}{1+\exp[(\varepsilon_{i,\sigma}-\mu)/k_BT]}, \tag{28}$$

where μ is the chemical potential adjusted at each iteration step to preserve the total electron number.

The first three terms of Eq. (26) describe the energy expectation value of the internal Hamiltonian, *a priori* not containing any references to the external field. In the bulk, the exchange-correlation energy per particle $e_{\rm xc}$ depends on the field B. This is a consequence of the fact that the external field changes the internal structure of the wave function. Formally $e_{\rm xc}$ depends on the vorticity

$$\gamma(\mathbf{r})=\nabla\times\frac{\mathbf{j}_p(\mathbf{r})}{n(\mathbf{r})}\bigg|_z, \tag{29}$$

which can be related to the external field B via the real current density,

$$\mathbf{j}(\mathbf{r})=\mathbf{j}_p(\mathbf{r})+\frac{e}{m^*}\mathbf{A}(\mathbf{r})n(\mathbf{r}). \tag{30}$$

For the homogeneous bulk, $\mathbf{j}(\mathbf{r})=0$. Dividing Eq. (30) by the density n and taking the cross product $\nabla\times$ gives

$$\nabla\times\frac{\mathbf{j}_p(\mathbf{r})}{n(\mathbf{r})}=-\frac{e}{m^*}\mathbf{B}. \tag{31}$$

Thus one replaces the external field by

$$B\rightarrow\frac{m^*}{e}|\gamma(\mathbf{r})|. \tag{32}$$

To minimize the total energy of the system, a functional derivative of $E[\phi_{i\sigma}]$ is taken with respect to $\phi_{i\sigma}^*$, applying the constraint of the $\phi_{i\sigma}$'s being normalized. The resulting self-consistent one-electron equation is (we drop the arguments $\mathbf{r}$ for simplicity)

$$\left[\frac{\mathbf{p}^2}{2m^*}+\frac{e}{2m^*}(\mathbf{p}\cdot\mathcal{A}+\mathcal{A}\cdot\mathbf{p})+\mathcal{V}_\sigma\right]\phi_{i\sigma}=\varepsilon_{i\sigma}\phi_{i\sigma}, \quad (33)$$

where $\mathbf{p}=-i\hbar\nabla$ and $\mathcal{A}=\mathbf{A}+\mathbf{A}_{\rm xc}$, with the exchange-correlation vector potential

$$e\mathbf{A}_{\rm xc}=\frac{1}{n}\left\{\frac{\partial}{\partial y}\frac{\partial[ne_{\rm xc}(n_\sigma,\gamma)]}{\partial\gamma}, \; -\frac{\partial}{\partial x}\frac{\partial[ne_{\rm xc}(n_\sigma,\gamma)]}{\partial\gamma}\right\}. \quad (34)$$

The quantity

$$\mathcal{V}_\sigma(\mathbf{r})=\frac{e^2}{2m^*}A(\mathbf{r})^2+V_\sigma(\mathbf{r})+V_H(\mathbf{r})+V_{{\rm xc}\sigma}(\mathbf{r}) \quad (35)$$

includes the external potential and Zeeman energy

$$V_{\uparrow,\downarrow}=V\pm\frac{1}{2}g^*\mu_B B, \quad (36)$$

the Hartree term

$$V_H=\frac{e^2}{4\pi\epsilon_0\epsilon}\int d\mathbf{r}'\frac{n(\mathbf{r}')}{|\mathbf{r}-\mathbf{r}'|}, \quad (37)$$

and the exchange and correlation potential

$$V_{{\rm xc}\sigma}=\frac{\partial[ne_{\rm xc}(n_\sigma,\gamma)]}{\partial n_\sigma}-\frac{e}{n}\mathbf{j}_p\cdot\mathbf{A}_{\rm xc}. \quad (38)$$

The total canonical angular momentum of the solution is defined as

$$L_z=\sum_{i\sigma}f_{i\sigma}\langle\phi_{i\sigma}|\hat{l}_z|\phi_{i\sigma}\rangle \quad (39)$$

$$=m^*\int d\mathbf{r}\;[xj_{p,y}(\mathbf{r})-yj_{p,x}(\mathbf{r})]. \quad (40)$$

Further details can be found in the original work of Vignale and Rasolt (1987, 1988).

The numerical solution of Eq. (33) is rather involved and requires special techniques to obtain good convergence. For details, see Koskinen *et al.* (1999).

B. Parametrization of the exchange-correlation energy in a magnetic field

Making use of the local-density approximation, the exchange-correlation energy per particle $e_{\rm xc}$ in a magnetic field can be expressed in terms of the total particle density n, the spin polarization $\zeta=(n_\uparrow-n_\downarrow)/n$, and the filling factor $\nu=2\pi\hbar n/eB$, where B is replaced by $m^*|\gamma|/e$; see Eq. (32). In the zero-field limit we earlier approximated the exchange-correlation energy per particle for the two-dimensional electron gas by a sum of the exact exchange and the correlation part, $e_{\rm xc}^{\rm TC}(n,\zeta)=e_{\rm x}^{\rm HF}(n,\zeta)+e_{\rm c}^{\rm TC}(n,\zeta)$, using a Padé approximant for $e_{\rm c}^{\rm TC}(n,\zeta)$ as provided by Tanatar and Ceperley (1989).

In the limit of very strong, spin-polarizing magnetic fields with filling factors $\nu<1$, Levesque, Weis, and MacDonald (1984) suggested a smooth dependence of the correlation energy on the filling factor ν,

$$e_{\rm xc}^{\rm LWM}(n,\nu)[{\rm Ha}^*]=-0.782\,133\sqrt{2\pi n}\,(1-0.211\nu^{0.74}+0.012\nu^{1.7}). \quad (41)$$

Fano and Ortolani (1988) interpolated the exchange-correlation energy from Monte Carlo results by Morf *et al.* (1986, 1987) and obtained

$$e_{\rm xc}^{\rm FO}(r_s,\nu)=\frac{\sqrt{2\pi n}}{\nu^{3/2}}\left[-\sqrt{\frac{\pi}{8}}\nu^2-0.782133\nu^{3/2}(1-\nu)^{3/2}+0.683\nu^2(1-\nu)^2-0.806\nu^{5/2}(1-\nu)^{5/2}\right]. \quad (42)$$

At arbitrary magnetic fields, Rasolt and Perrot (1992) suggested the following interpolation between the limits of zero fields ($\nu\to\infty$), using the approximation of Tanatar and Ceperley, and strong fields ($\nu<1$) using the Levesque-Weis-MacDonald parametrization:

$$e_{\rm xc}(n,\zeta,\nu)=[\varepsilon_{\rm xc}^{\rm LWM}(n,\nu)+\nu^4\varepsilon_{\rm xc}^{\rm TC}(n,\zeta)]/(1+\nu^4). \quad (43)$$

Alternatively, Koskinen *et al.* (1999) suggested the form

$$e_{\rm xc}(n,\zeta,\nu)=e_{\rm xc}^{\infty}(n)e^{-f(\nu)}+e_{\rm xc}^{\rm TC}(n,\zeta)(1-e^{-f(\nu)}), \quad (44)$$

where $f(\nu)=1.5\nu+7\nu^4$. This equation interpolates between the spin-polarized infinite magnetic-field limit,

$$e_{\rm xc}^{\infty}(n)=-0.782\,133\sqrt{2\pi n}, \quad (45)$$

as approximated by Fano and Ortolani (1988), and the zero-field limit $e_{\rm xc}^{\rm TC}(n,\xi)$ generalized for intermediate polarizations [see Sec. III.B and Eqs. (9) and (10)]. For $\nu<0.9$, Eq. (45) closely follows the results of Fano and Ortolani for polarized electrons in the lowest Landau level, and quickly saturates to the zero-field result for $\nu>1$.

Due to the correlation in the fractional quantum Hall regime, the full exchange-correlation energy has cusps (infinite derivatives) at certain filling factors, which were ignored in the above approximations. Heinonen, Lubin, and Johnson (1995) added such cusps to the denominator of the Padé approximant Eq. (43) (see also Heinonen *et al.*, 1999). A similar approach was taken by Price and Das Sarma (1996).

C. Ground states and addition energy spectra within the symmetry-restricted current-spin-density-functional theory

1. Angular momentum transitions

The current-spin-density-functional theory (CSDFT) was first applied to quantum dots by Ferconi and Vignale (1994), who worked in the symmetry-restricted formalism with a parabolic confinement potential. For the vorticity-dependent exchange-correlation energy in the

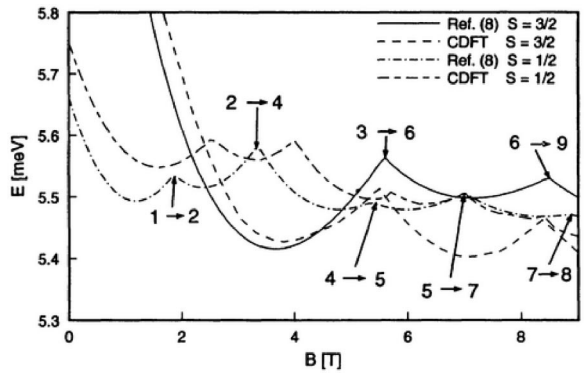

FIG. 47. Comparison of the ground-state energies between CSDFT and exact diagonalization (Ref. 8 in Ferconi and Vignale; see Pfannkuche, Gudmundsson, and Maksym, 1993) for a parabolic quantum dot with three electrons and spin $S=3/2$ or 1/2. The transitions in orbital angular momentum are given as well. (An energy ω_h/N was subtracted from the total energy.) From Ferconi and Vignale, 1994.

local-density approximation, they used the interpolation of Rasolt and Perrot (1992) [Eq. (43)]. Ferconi and Vignale (1994) tested the symmetry-restricted CSDFT against results of exact diagonalizations for quantum dots confining two and three electrons (Hawrylak and Pfannkuche, 1993; Pfannkuche, Gudmundsson, and Maksym, 1993). This comparison is shown in Fig. 47 for the different spin configurations of the three-electron quantum dot (where typical GaAs parameters and $\hbar\omega=3.37$ meV were used). Ferconi and Vignale noted that the transitions in orbital angular momentum with increasing field were accurately obtained. The deviation of the current CSDFT energies from the exact ones is less than $\lesssim 5\%$.

2. Addition energy spectra in magnetic fields

Steffens, Rössler, and Suhrke (1998) modeled the addition energy spectra in the symmetry-restricted current spin-density-functional approach, using GaAs system parameters as in Fig. 47, but a larger confinement energy $\hbar\omega=5$ meV and including a Zeeman energy with an effective Landé factor $g^*=-0.44$. They used the same exchange-correlation energy as Ferconi and Vignale (1994) [Eq. (43)]. The addition energies, as shown in Fig. 48, agree remarkably well with the measurements of Tarucha *et al.* (1996), correctly reproducing the shell gaps at both zero and (weak) finite magnetic fields. In the Fock-Darwin spectra (Fig. 31), large orbital degeneracies occur as a function of B. Just as in the zero-field case, when occupying different (quasi)degenerate states it can be favorable to align the spins in order to maximize the exchange energy. (This is indicated in Fig. 48 by arrows, showing the excess spin of the corresponding ground state at $B\neq 0$.) The main features in the CSDFT addition spectrum agree well with the constant-interaction model plus exchange corrections, used by Tarucha *et al.* (1996) for a description of the experimental data.

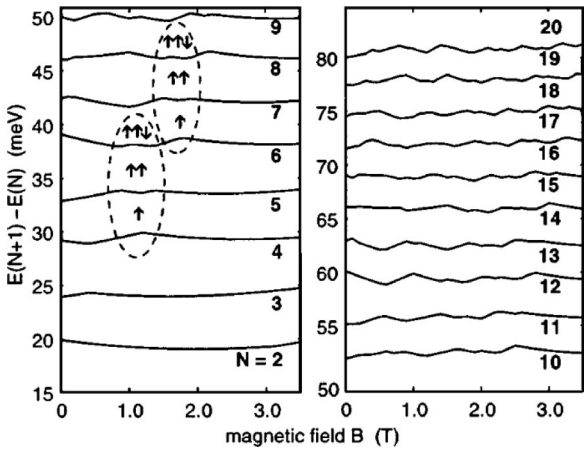

FIG. 48. Addition spectrum for $N<20$ obtained from symmetry-restricted CSDFT for a parabolic quantum dot ($\hbar\omega=5$ meV, $g^*=-0.44$, $m^*=0.067$, and $\epsilon=12.4$). From Steffens, Rössler, and Suhrke, 1998.

D. Reconstruction of quantum Hall edges in large systems

As discussed earlier, de Chamon and Wen (1994) showed that the $\nu=1$ edge of an extended quantum Hall system (or correspondingly a large quantum dot in a strong magnetic field) may undergo a polarized reconstruction to a "stripe phase": a lump of electrons separates from the bulk at a distance $\approx 2\ell_B$ (where $\ell_B=\sqrt{\hbar/eB}$). Karlhede *et al.* (1996) noted that for a sufficiently small Zeeman gap, the polarized reconstruction suggested by Chamon and Wen may be preempted by edge spin textures. Crossing the edge, the spins tilt away from their bulk direction. Along the edge they precess around the direction of the magnetic field. The spin-textured edge exists only for a sufficiently smooth confinement and small Zeeman coupling. From unrestricted Hartree-Fock calculations, Franco and Brey (1997) obtained a phase diagram that for steep confining potentials predicts a sharp and fully polarized edge. When the confinement potential is softened and the Zeeman energy is comparably large, de Chamon and Wen (1994) predicted the formation of a translation-invariant edge. It turned out later that reconstruction with a modulated charge density along the edge can be energetically favorable. For large Zeeman energy, a transition into a polarized charge-density-wave edge was found. For a small Zeeman energy the edge will reconstruct into a spin-textured state with translation-invariant charge density along the edge, or a combination of charge modulation along the edge and spin textures (see also Karlhede and Lejnell, 1997). (For filling fractions $\nu\leqslant 1$, quantum Hall edges were also studied within the Chern-Simons-Ginsburg-Landau theory; see, among others, Zhang *et al.*, 1988; Lee and Kane, 1990; Leinaas and Viefers, 1998.)

The following discussion of edge reconstruction in large quantum dots is restricted to the spin-polarized regime. Reconstruction of the maximum-density droplet can take place for an increasing ratio of ω/ω_c, i.e., ei-

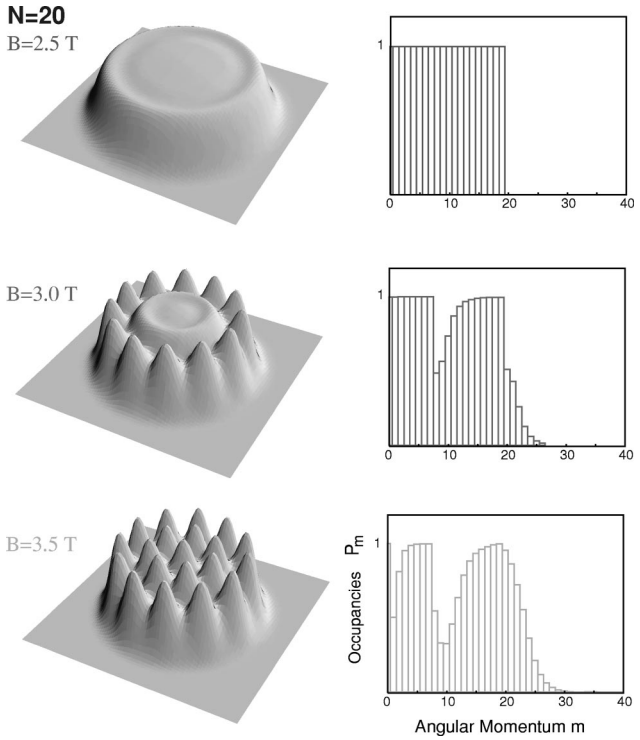

FIG. 49. Single-particle densities as obtained in CSDFT for a 20-electron quantum dot: left, together with the angular momentum occupancies P_m; right, in the maximum-density droplet phase, after edge formation, and at full reconstruction (see text). From Reimann, Koskinen, Manninen, and Mottelson, 1999.

ther by softening the confinement (smaller ω) or equivalently by increasing the magnetic field (larger ω_c) since a higher field effectively compresses the droplet.

1. Edge reconstruction in current-spin-density-functional theory

For filling factors around $\nu=1$, Reimann, Koskinen, Manninen, and Mottelson (1999) applied current-spin-density-functional theory to calculate the ground states of N parabolically confined electrons in the symmetry-unrestricted scheme. Figure 49 shows the ground-state densities for a 20-electron quantum dot at various field strengths B, calculated for typical GaAs parameters and a confinement strength $\hbar\omega=4.192N^{-1/4}$ meV, chosen such that independent of N, the electron density in the dot is kept approximately constant ($r_s\approx 2a_B^*$).

The droplet becomes completely polarized at $B\approx 2.4$ T, forming a maximum-density droplet as shown in the upper panel of Fig. 49 (here at a field $B=2.5$ T). This figure also shows the angular momentum occupancy

$$P_m=\sum_{i<N,n}|\langle nm|\phi_{i,\downarrow}\rangle|^2 \tag{46}$$

obtained by projecting the Kohn-Sham single-particle states $|\phi_{i,\downarrow}\rangle$ on the Fock-Darwin states $|nm\rangle$. As expected, all angular momenta $m<N-1$ have occupancy one for the maximum-density droplet. As suggested by de Chamon and Wen (1994) as well as MacDonald, Yang, and Johnson (1993) (and discussed briefly in Sec. V.B.4 above), with increasing magnetic field the Coulomb repulsion causes the droplet to redistribute its charge density. Electrons are moved from lower to higher angular momentum states, leaving a gap of unoccupied states for $m<N-1$ and forming the Chamon-Wen edge state, as illustrated in the middle panel of Fig. 49. After reconstruction, the maximum-density droplet has thrown out a ring of separate lumps of charge density located at a distance $\approx 2\ell_B$ from the inner droplet, with each lump containing one electron and having a radius somewhat larger than the magnetic length ℓ_B. Figure 51 below shows a similar edge reconstruction for a larger dot, confining $N=42$ particles. The mean-field solution breaks the azimuthal symmetry of the underlying Hamiltonian, and the expectation value of the total angular momentum can take fractional values (here, $L=205.13$).

The broken-symmetry edge states appear similar to the "Wigner-necklace" states reported by Goldmann and Renn (1999); see Sec. VI.B.6. For even stronger fields, a sequence of rings is formed until the whole droplet is reconstructed (lowest panel in Fig. 49). This process is accompanied by the opening of a large Fermi gap in the Kohn-Sham single-particle spectrum. Intriguingly, the distribution of density maxima agrees well with the predictions of geometric shell structure in classical Wigner molecules (Sec. IV.A).

Figure 50 shows the real current $\mathbf{j}(x,y)$ [Eq. (30)], plotted as a vector diagram. It shows vortices that are located around the individual density maxima.

2. Phase diagram

A systematic study of broken-symmetry edge formation and subsequent reconstruction into sequences of rings is displayed in Fig. 51. The polarization line separates the maximum-density droplet state from the not fully polarized states. It approaches the reconstruction line, which marks the onset for the formation of the broken-symmetry Chamon-Wen edge. Such narrowing of the region in which the maximum-density droplet is stable was noted earlier by MacDonald, Yang, and Johnson (1993), by de Chamon and Wen (1994), and in a more recent study by Ferconi and Vignale (1997). (In the above example, however, the shapes of the phase boundaries differ from the result of Ferconi and Vignale, as they used a fixed confinement strength ω for different N.) With increasing B, sequences of rings form until the maximum-density droplet is fully reconstructed. CSDFT then yields localization of electrons in the whole dot region, in agreement with the prediction made within the unrestricted Hartree-Fock approach by Müller and Koonin (1996).

Observable consequences of the deformed solutions found within the CSDFT and Hartree-Fock could be rotational spectra (Müller and Koonin, 1996). Analyzing the Kohn-Sham single-particle orbitals for the first edge reconstruction of the maximum-density droplet, one notices that they fall into two discrete subsets, the

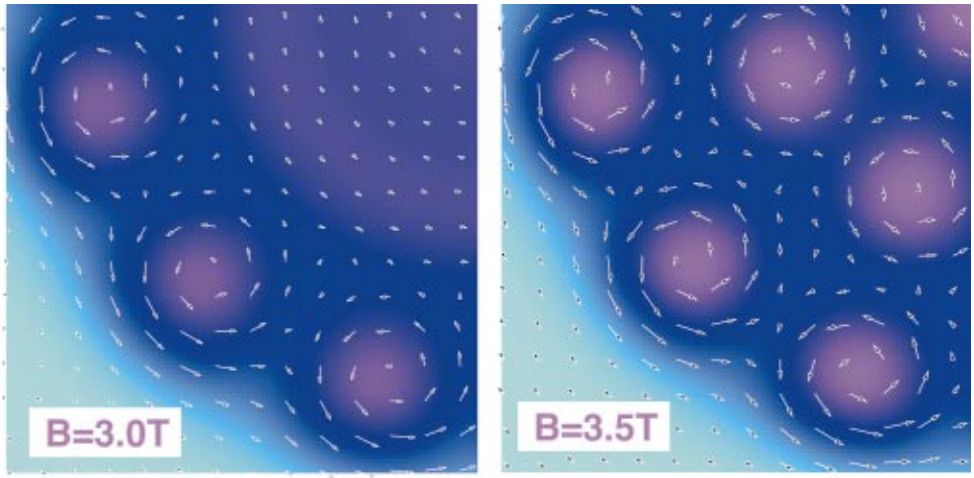

FIG. 50. Current $\mathbf{j}(\mathbf{r})$, left, for $N=20$ at $B=3.0$ T; and, right, $B=3.5$ T. From Reimann, Koskinen, Manninen, and Mottelson, 1999 [Color].

maximum-density droplet and the broken-symmetry edge. This further opens up a possibility for collective excitations localized at the edge.

We earlier discussed the phase diagram obtained from capacitance spectroscopy (Ashoori, Störmer, *et al.*, 1992; Ashoori *et al.*, 1993; Ashoori, 1996) as well as resonant tunneling Coulomb blockade spectra (Oosterkamp *et al.*, 1999) as a function of magnetic field. Comparing Fig. 51 with Fig. 37, in fact we note that the phase boundaries (which in the experimental data correspond to the pronounced kinks in the addition energy curves) qualitatively agree with the predictions of CSDFT. (The fact that the transitions between the different phases are found at smaller fields, is due to a different electron density, which for the experimental data was estimated to correspond to $r_s \approx 1.3 a_B^*$.)

Recently Yang and MacDonald (2002) studied in detail the phase diagram beyond the maximum-density droplet. They performed Hartree-Fock and exact diagonalization calculations and observed that the maximum-density droplet becomes unstable due to the addition of interior holes, i.e., moving the occupancies of single-particle states from smaller to higher angular momenta. For $N \leqslant 14$, the hole was located at the center of the dot, while for larger N the hole occured for nonzero single-particle angular momentum, in accordance with the results of CSDFT.

E. Edge reconstruction and localization in unrestricted Hartree-Fock theory

The formation of localized states was first predicted by Müller and Koonin (1996) from a geometrically unrestricted Hartree-Fock approach. The spectrum of rotational excitations was approximated by projection of Φ_{HF} onto eigenfunctions of good angular momentum (Sec. IV.B.3). To test the validity of the Hartree-Fock approach, Müller and Koonin improved the wave functions for the polarized localization regime by introducing Jastrow-type correlations of the form

$$\left(\mathcal{S} \prod_{i<j} |z_i - z_j|^k \right) \Phi_{\mathrm{HF}}, \tag{47}$$

with a symmetrizing operator $\mathcal{S}$ and a variational parameter k. Φ_{HF} denotes the Hartree-Fock Slater determinant. They found that the Jastrow-type wave function did not significantly improve the Hartree-Fock energy. The phase diagram provided by Müller and Koonin is only in qualitative agreement with Fig. 51, partly because Hartree-Fock theory does not correctly predict the magnetic-field strength at which localization occurs (Klein *et al.*, 1995, 1996).

Dean, Strayer, and Wells (2001) extended the work of Müller and Koonin to an investigation of the thermal response of quantum dots in high magnetic fields, showing that temperature can induce transitions between the different phases.

F. Ensemble density-functional theory and noncollinear spins

The standard spin-dependent density-functional theory assumes the single-particle density matrix to be diagonal in the spin space. However, in the exact DFT formalism this does not have to be the case (von Barth and Hedin, 1972; Gunnarsson and Lundqvist, 1976). If the off-diagonal elements are nonzero, the Kohn-Sham equations no longer separate to two coupled equations for spin-up and spin-down electrons, but the single-particle states have to be described with two-component spinors. The solutions then give possibilities for more complicated spin structures, like the so-called Skyrmions (Skyrme, 1961) with noncollinear spins, which can lower the total ground-state energy.

In ensemble DFT (Heinonen *et al.*, 1995, 1999; Lubin *et al.*, 1997), the effect of the nondiagonality of the density matrix can be taken into account and still retain some of the local character of the exchange-correlation potential. Heinonen *et al.* (1999) developed the neces-

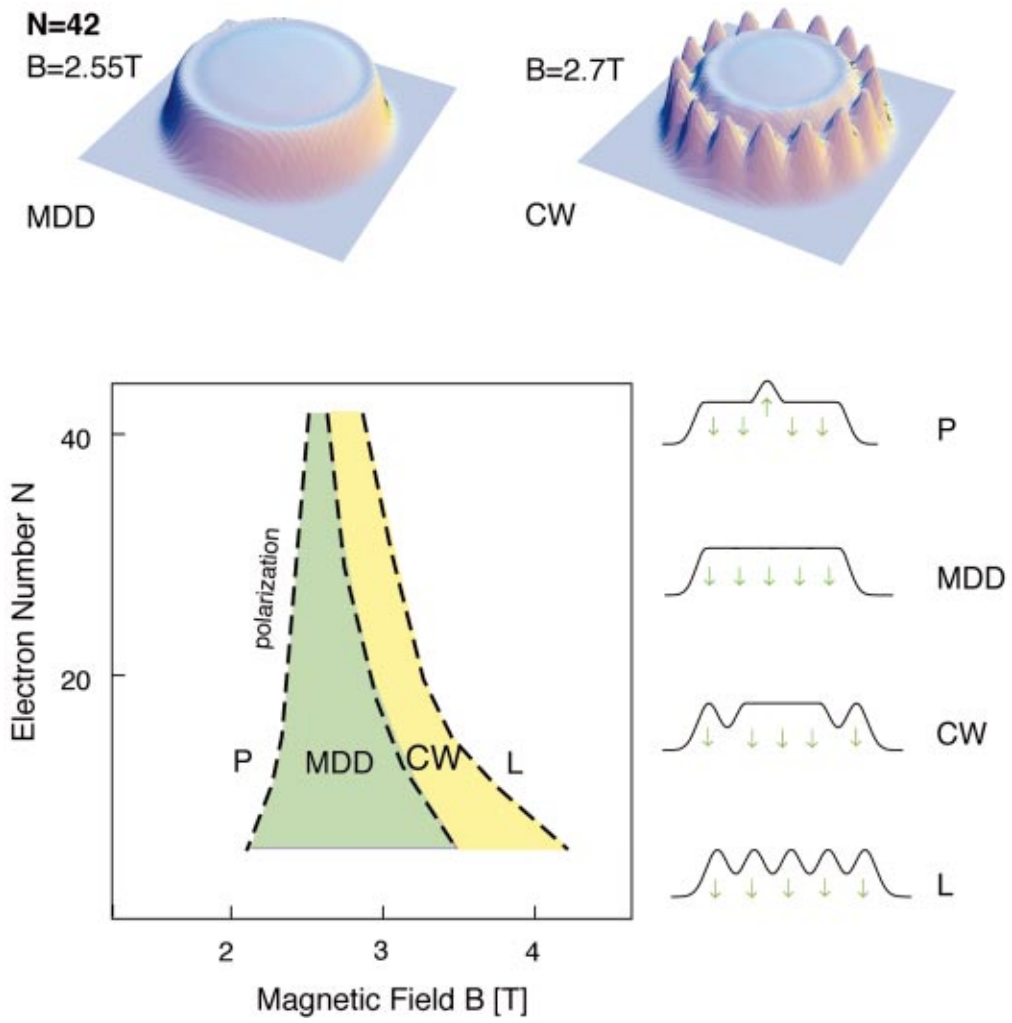

FIG. 51. Maximum-density droplet and phase diagram. Upper panel, charge density of a spin-polarized quantum dot with $N=42$ electrons forming a maximum-density droplet (MDD) and a reconstructed edge (CW); lower panel, phase diagram as a function of magnetic field B and electron number N. The schematic density profiles on the right indicate the polarization transition (P), the maximum-density droplet (MDD), formation of the Chamon-Wen edge (CW) and localization (L). After Reimann, Koskinen, Manninen, and Mottelson, 1999 [Color].

sary exchange-correlation functionals and applied ensemble DFT to circular quantum dots in a strong magnetic field. They found that the spin-textured states with noncollinear spins were ground states in magnetic fields corresponding to filling factors close to $\nu=1$ and $\nu=1/3$. The existence of noncollinear spins necessarily means reduction of the total spin from a fully polarized state. Within the configuration-interaction method, such a reduction of the total spin was also found by Maksym and Chakraborty (1992) for a four-electron system in corresponding magnetic fields. However, a detailed comparison of this spin structure to the type obtained by Heinonen *et al.* (1999) was not made.

The ensemble DFT calculations of Heinonen *et al.* restricted the electron density to a circular symmetry. This prevents solutions with electron localization, which are known to be the ground-state solutions in the usual LSDA in strong magnetic fields. Whether the possible charge localization will hinder the spin textures or vice versa is still an open question.

VIII. QUANTUM RINGS IN A MAGNETIC FIELD

A. Electronic structure of quantum rings

A narrow quantum ring in a (perpendicular) magnetic field forms a many-body system with interesting properties. If the ring is narrow enough it is a quasi-one-dimensional conductor. The magnetic flux can be restricted (at least in theory) to the inner region of the ring, making it a perfect Ahanorov-Bohm (1959) system. The main interest in small rings in a magnetic field is the possibility of persistent currents, first predicted by Hund (1938). The Aharonov-Bohm effect and persistent currents first became important in connection with macroscopic superconducting rings with or without Josephson junctions (Byers and Yang, 1961; Bloch, 1972; Büttiker *et al.*, 1983). More recently, much attention has been paid to studies of persistent currents in microscopic quantum rings with a small number of electrons (Chakraborty and Pietiläinen, 1995; Niemelä *et al.*, 1996; Tan and Inkson, 1999; Hu *et al.*, 2000).

Here we concentrate only on the many-body problem of small circular quantum rings and on the possibility of describing it within CSDFT. In a small system the concept of superconductivity as a macroscopic quantum state loses its meaning. A simple (single-particle) picture of the persistent current in a ring with circular symmetry is that electrons occupy orbital angular momentum states rotating in only one direction around the center.

For a circular ring in two dimensions, we begin with the single-electron Hamiltonian

$$H=\frac{\hbar^2}{2m}(\mathbf{p}+e\mathbf{A})^2+\frac{1}{2}m^*\omega^2(r-r_0)^2, \tag{48}$$

where r_0 is the radius of the ring and ω determines its width. Electron-electron interactions can be added as normal Coulomb $e^2/(4\pi\epsilon_0\epsilon r)$ forces. By choosing the vector potential as (Viefers, Deo, *et al.*, 2000)

$$A_\varphi=\begin{cases} B_0 r/2, & r\leqslant r_i \\ B_0 r_i^2/(2r), & r>r_i, \end{cases} \tag{49}$$

$$A_r=0, \tag{50}$$

where $r_i \ll r_0$, the magnetic flux is restricted to the inside of the ring so that the electrons essentially move in a field-free region.

In a strictly one-dimensional ring penetrated by a magnetic flux $\Phi=\pi r_i^2 B_0$, the vector potential in the Hamiltonian, Eq. (48), causes a periodic boundary condition for the single-particle states,

$$\psi(r_0,\varphi)=e^{-i2\pi\Phi/\Phi_0}\psi(r_0,\varphi+2\pi), \tag{51}$$

where $\Phi_0=h/e$ is the flux quantum. This is similar to the one-dimensional Bloch condition in the theory of band structures (Büttiker *et al.*, 1983). It is then obvious that single-particle energy levels will be periodic functions of Φ with a periodicity of Φ_0. In the strictly 1D case the single-particle levels can be written as

$$\epsilon_m=\frac{\hbar^2}{2m}\frac{1}{r_0^2}\left(m+\frac{\Phi}{\Phi_0}\right)^2. \tag{52}$$

The quantum number m is the orbital angular momentum of the single-particle level as before. As in the case of a harmonic dot, the effect of the magnetic field (flux) is to move electrons from low to high angular momentum states. Figure 52 shows the single-particle energy levels for narrow rings and for rings with finite thickness (defined by the parameter $\alpha=\pi r_0^2 m^*\omega/h$). When the ring thickness increases, the second and higher Landau bands become lower in energy and the low-lying states start to resemble those of a parabolic quantum dot, like that shown in Fig. 31. The total energy of a noninteracting system is determined solely as the sum of single-particle energy levels. In the strictly 1D case it is a periodic function of the magnetic flux. In a quasi-1D ring the total energy increases with the flux as shown in Fig. 53 for four "spinless" (i.e., polarized) electrons. Figure 53 also shows that the only effect of the electron-electron interaction in the spinless case is an upward shift of the total energy. This is due to the fact that in a narrow ring

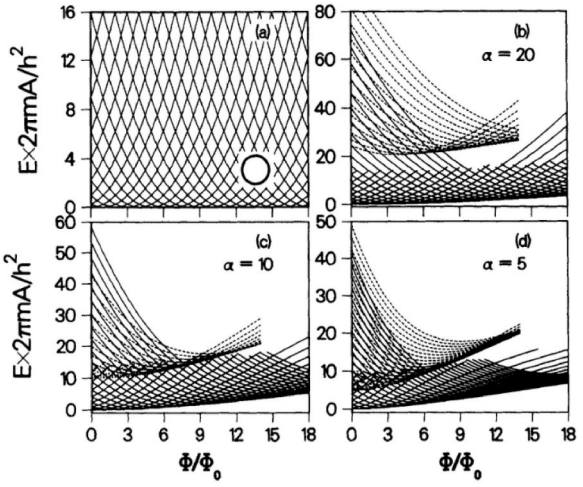

FIG. 52. Single-electron energy levels as a function of the flux for (a) a narrow ring and (b)–(d) rings with finite thickness. The Fock-Darwin levels belonging to the second Landau band are shown as dotted lines. $\alpha=\pi r_0^2 m^*\omega/h$. From Chakraborty and Pietiläinen, 1994.

all the close-lying states belong to the lowest Landau band and cannot be coupled by the Coulomb interaction because of the conservation of the angular momentum (Chakraborty and Pietiläinen, 1994). The spin degree of freedom makes the many-body spectrum more complicated and increases the effect of the electron-electron interactions. This is understood most easily in the case of a strictly 1D ring with delta-function interactions between the electrons. In the spinless case the delta-function interaction does not have any effect due to the Pauli exclusion principle, which prevents two electrons from being in the same place. If the spin degree of freedom is included, the spectrum changes as demonstrated by Niemelä *et al.*, 1996: Figure 54 shows the many-body spectra as a function of magnetic flux for a four-electron ring with and without a Coulomb interaction between

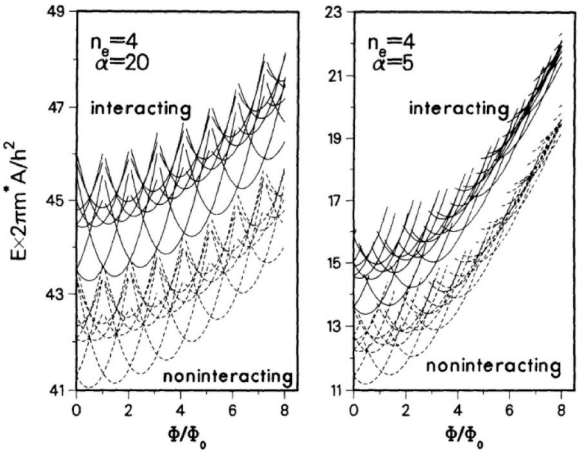

FIG. 53. Total energy spectrum of four noninteracting and interacting "spinless" electrons, for two different widths of the ring. Results for the interacting case were obtained by the configuration-interaction method. From Chakraborty and Pietiläinen, 1994.

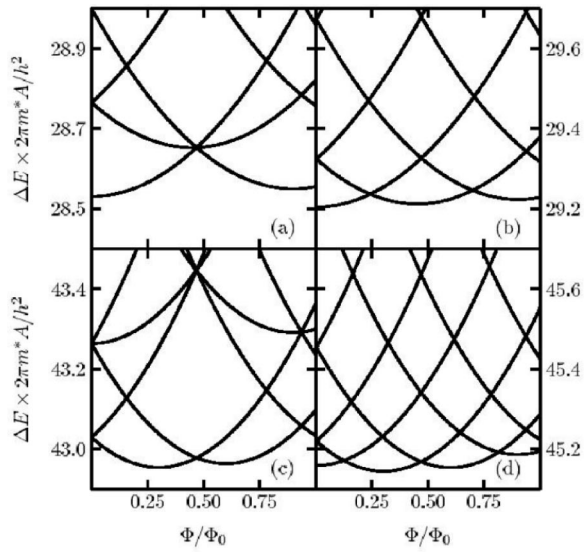

FIG. 54. Lowest (many-body) energy levels of a four-electron ring: (a) noninteracting electrons with $S_z=1$; (b) interacting electrons with $S_z=1$ (configuration-interaction method); (c) noninteracting electrons with $S_z=0$; and (d) interacting electrons with $S_z=0$. Note that all states with $S_z=1$ have a degenerate state with $S_z=0$, since for total spin $S=1$, S_z has values $-1,0,1$. From Niemelä *et al.*, 1996.

the electrons. The ring has a finite thickness. The spectrum is more complicated than in the spinless case (Fig. 53) and the electron-electron interactions change the spectrum drastically.

Current-density-functional theory has been used to compute the ground-state energy of small rings in a magnetic field. Viefers, Deo, *et al.* (2000) used the single-particle Hamiltonian, Eq. (48), and the CSDFT described in Sec. VII. They computed the ground-state properties of fairly narrow rings pierced with a magnetic flux using the vector potential from Eqs. (49) and (50), which leaves the electron ring in a field-free region. The results are in fair agreement with the full many-body results shown in Figs. 54(b) and (d). In both cases the $S=0$ state has the lowest energy at the flux value $\Phi=\Phi_0/2$, while at $\Phi=0$ and at $\Phi=\Phi_0$ the lowest energy state is the $S=1$ state. The total orbital angular momentum increases from 0 to 4 when the flux increases from 0 to Φ_0. The main difference between the results of the CSDFT and configuration-interaction calculation is that in the former the orbital angular momentum changes gradually as the flux is increased, while in the exact calculation the angular momentum is a good quantum number and has only integer values. The reason for the noninteger values of L in the CSDFT is spontaneous symmetry breaking due to the the mean-field character of the CSDFT, as discussed previously.

B. Persistent current

In the independent-electron picture the persistent current (here along the ring) associated with the single-particle state n is (Byers and Yang, 1961)

$$J_n=-\frac{\partial \epsilon_n}{\partial \Phi}, \tag{53}$$

where ϵ_n is the energy eigenvalue of the state in question. [It is straightforward to derive this equation in the case of a strictly 1D system where the electron wave vector is restricted to be $k_n=(1/r_0)\Phi/\Phi_0$ and consequently the electron velocity is $v_n=\hbar k_n/m=\partial E_n/\hbar\partial k_n$.] In the independent-particle model the total current is a sum over the single-particle currents [Eq. (53)]. In the framework of a many-body theory, say configuration interaction, the total current for a many-body state can still be calculated from a similar equation, only ϵ_n in Eq. (53) is replaced with the total energy of the many-body state in question.

At zero temperature the persistent current will have discontinuities due to level crossings. In unrestricted CSDFT some of these discontinuities are smeared out due to internal symmetry breaking (Viefers, Deo, *et al.*, 2000), although the overall structure of the persistent current is in fair agreement with the exact result. The consistency of the CSDFT was tested by integrating the current density over the cross section of the ring to compute the current. The result was in excellent agreement with that determined from the total energy by Eq. (53).

In a real physical system the quantum ring does not have a perfect circular symmetry but is necessarily distorted by the underlying lattice and its impurities. The effect of an impurity on the persistent current was studied by Chakraborty and Pietiläinen (1995) using exact diagonalization and by Viefers, Deo, *et al.* (2000) using CSDFT. Another important subject is the effect of the electron leads on the persistent current (Büttiker, 1985; Jayannavar and Deo, 1995).

Leggett (1991) proposed that in a one-dimensional ring the oscillations of the persistent current as a function of the flux are independent of the interactions. His conjecture was verified by Chakraborty and Pietiläinen (1995) using the configuration-interaction technique for a four-electron system. The effect of the impurity is to reduce the persistent current, but it does not change the phase of the oscillations as a function of the flux. The only effect of the electron-electron interactions is a shift of the energy spectrum to higher energies.

It should be noted that in the case of "spinless" electrons the electron-electron interactions do not have any effect on the flux dependence of the current. This does not hold if the spin degree of freedom is taken into account (as should be done in the case of a weak field), as demonstrated above in Fig. 54. Moreover it has been shown that topological defects, for example, a finite-length wire connected to an ideal ring, will diminish the parity effect and affect the persistent current (Deo, 1995, 1996).

IX. QUANTUM DOT MOLECULES

Quantum dot molecules consist of two or more quantum dots that are so close to each other that electrons

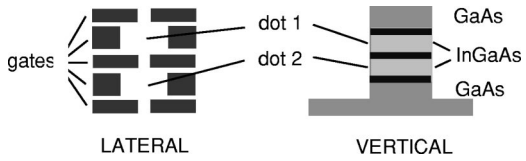

FIG. 55. Schematic pictures of lateral and vertical double dots (top and side view, respectively), made from gated or etched heterostructures.

can tunnel between them. Here we shall concentrate on the double quantum dot, i.e., a system consisting of two identical quantum dots separated by a tunnel barrier. For a review on electron transport through double quantum dots, we refer the reader to the forthcoming article by van der Wiel *et al.* (2003). Coupled quantum dots have recently also attracted attention in connection with research on quantum computing (see, for example, the work of Loss and Di Vincenzo, 1998, or Burkhard, Loss, and Di Vincenzo, 1999).

Figure 55 illustrates schematically lateral- and vertical-dot molecules fabricated by the gating or etching of heterostructures, as described above for single dots (Sec. II.A). Another method used to fabricate quantum dot molecules is the cleaved-edge overgrowth (see Schedelbeck *et al.*, 1997).

Experimentally it is difficult to manufacture two identical dots with exactly the same capacitances, tunneling contacts, and leads (needed for conductance measurements). In the case of a lateral dot this problem can be partly overcome by constructing the gates (see Fig. 55) such that their voltages can be independently varied, allowing the electronic tuning of the potential wells and tunnel barriers (Waugh *et al.*, 1995). In vertical molecules, the similarity of the two dots is sensitive to the etching process and it is not easy to make a sample with two identical dots (Austing *et al.*, 1997).

As with single dots, in a double dot the Coulomb blockade dominates the conductance. However, different charging energies of the two dots complicate the mechanism. The conductance peaks are usually described as a "phase diagram" showing the Coulomb blockades caused by charging the dots independently (Hofmann *et al.*, 1995; Blick *et al.*, 1996).

The conductance can be plotted on a plane spanned by two gate voltages, which are differently coupled to the two individual dots (Fig. 56). The resulting honeycomb-shaped phase boundaries determine the number of electrons in the two dots. This phase diagram (the details of which depend on the experimental setup) can be understood by minimizing the charging energy of the capacitative system, with the restriction that each dot have an integer number of electrons. Either one can study the tunneling through the two dots, or the tunneling current goes through only one of the dots while the other dot is capacitatively coupled to the conducting dot (Hofmann *et al.*, 1995). The resulting phase diagram is qualitatively similar in both cases. This shows that it is the coupling of the electronic structures of the two dots

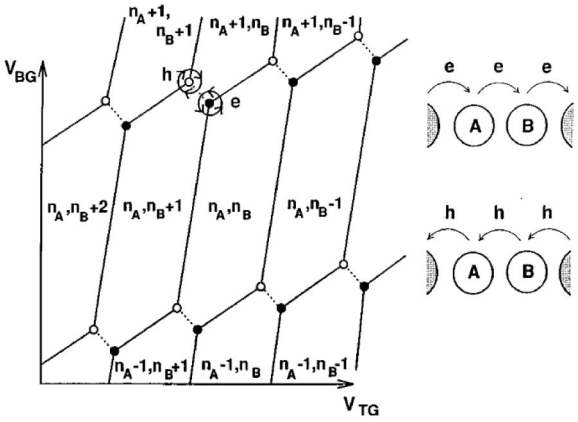

FIG. 56. Dependence of the positions of the conductance maxima on the two gate voltages of a double dot, schematically illustrated by the lines forming a lattice. n_A and n_B indicate the numbers of electrons in dots A and B, respectively. Black dots and open circles denote the electron- and hole-transport processes, as indicated in the inset and on the right-hand side. From Blick *et al.*, 1996.

that plays the dominating role in the conductance measurements, and not the leads.

In a tunable double-dot system the coupling between the potential wells can be varied and the two dots can be adjusted to be similar (Waugh *et al.*, 1995; Dixon *et al.*, 1996). The conduction peaks then split into two peaks reflecting the coupling of the energy levels of the two dots. For example, a tight-binding model causes each of the single-dot levels to split into a "bonding" and an "antibonding" level. When these resonances pass the Fermi surface, a conductance peak is observed. This simple interpretation is supported by the fact that in a triple-dot system each conductance peak is split into three separate peaks (Waugh *et al.*, 1995). More recently, Schmidt *et al.* (1997) and Blick *et al.* (1998) studied in detail the formation of this coherent molecular mode in the tunneling current through a double dot.

Theoretically conductance spectroscopy through dot arrays has been studied using model Hamiltonians based on the Anderson (1961) or Hubbard (1963) models. We do not go into the details here, but only mention that the most general model Hamiltonian of this type includes the energy levels and the charging energy for each dot, the interdot tunneling as well as the continuous spectra of the leads, and tunneling between the dots and the leads (Chen *et al.*, 1994; Klimeck *et al.*, 1994; Stafford and Das Sarma, 1994; Niu *et al.*, 1995; Sun *et al.*, 2000). The electron transport can be calculated using Green's-function techniques (Meir and Wingreen, 1992). In the Hubbard model, the splitting of the conductance peaks into, for example, two separate peaks for a double-dot molecule depends on the interdot hopping parameter t and on the charging energy U as illustrated in Fig. 57 (Klimeck *et al.*, 1994).

The qualitative features of the conductance peaks can be understood as coming from the internal structure of the dot molecule, while the leads (with a continuous energy spectrum) play a minor role. Let us now investigate

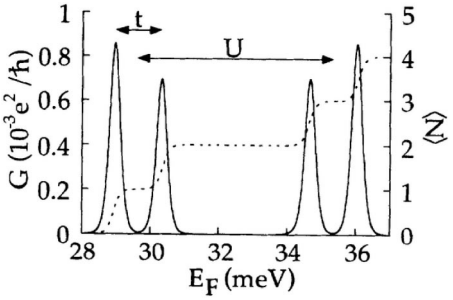

FIG. 57. Calculated conductance for a system of coupled symmetric quantum dots as a function of the Fermi energy. U is the charging energy and t is the coupling between the dots. The dashed line shows the change in the number of electrons N. From Klimeck *et al.*, 1994.

this internal structure in detail, while neglecting the interaction with the contacts.

A. Lateral-dot molecules in the local spin-density approximation

We return to a description of the double-dot systems in the density-functional formalism. Again, we restrict the discussion to the ground-state properties of isolated systems, i.e., dot molecules without leads. In lateral-dot molecules, the electrons of the individual dots move in the same plane, now confined by a potential with two or more distinctive minima. There are several ways to construct such a model potential. Often two harmonic potentials are superimposed (Wensauer *et al.*, 2000). However, for extending the molecule from a double dot to more complicated molecules it is more straightforward to use a finite-range potential for the single-dot components, which overlap only if close. For example, a confining potential can be modeled by inverted Gaussians (Adamowski *et al.*, 2000; Kolehmainen *et al.*, 2000). For a double dot we then use

$$V_{\text{ext}}(\mathbf{r}) = V_0(2 - e^{-\alpha|\mathbf{r}-\mathbf{d}/2|^2} - e^{-\alpha|\mathbf{r}+\mathbf{d}/2|^2}), \tag{54}$$

where V_0 and α are parameters adjusting the depth and the curvature of the potential of a single dot, and d is the distance between the two dots. The bottom of each dot is harmonic and the electronic structure of a single dot is very similar to that obtained by harmonic confinement.

In a double dot molecular states are formed if the two dots interact. In the simplest case with only one electron per dot, a symmetric bonding and an antisymmetric antibonding state are formed. The symmetric orbital, corresponding to the spin singlet, is the ground state. The antibonding state is a spin triplet. In the local spin-density approximation the singlet state will localize one electron with spin down in one of the dots, while the spin-up electron localizes in the other dot. This spin-density-wave-like state is again a manifestation of the internal symmetry breaking in the LSDA mean-field approach.

Wensauer *et al.* (2000) studied double dots with 2, 4, and 8 electrons with overlapping harmonic confinement potentials. In the case of two electrons the electronic structure changes from the "artificial helium atom" to an "artificial hydrogen molecule" when the dot-dot distance is increased from zero. Wensauer *et al.* (2000) found that the closed-shell spin-singlet state of the helium changes to an $S=1$ triplet of the hydrogen molecule. However, one would expect that in the case of the molecule, the true ground state should be a singlet. In the local spin-density approximation, this is expected to correspond to an antiferromagnetic coupling of the spins of the two artificial hydrogen atoms due to the fact that the LSDA tends to reflect the internal structure of the quantum state. (Note that two electrons in a strongly deformed ellipsoidal quantum dot already form a spin-density wave, as we saw in Fig. 17.) When the number of electrons in each dot increases, the electronic structure becomes more complicated. If the distance of the dots is large, at magic electron numbers in the single dots the molecule is likely also to form closed shells, like a molecule of noble-gas atoms. For open shells, the individual dots can have a spin determined by Hund's rule or can even form an internal spin-density wave (see Sec. IV.B). Wensauer *et al.* (2000) find that for two electrons in each dot, there is a transition from the well separated closed-shell dots to open-shell single dots with four electrons. The molecule with $S=0$ becomes a dot with $S=1$ when the interdot distance decreases. For molecules with four electrons in each dot, Wensauer *et al.* found ferromagnetic coupling between the dots, the total spin being $S=2$. Again the possibility of antiferromagnetic coupling was not considered.

Kolehmainen *et al.* (2000) studied quantum dot dimers described with the external potential Eq. (54) and having 10, 12, or 14 electrons in each dot. Single dots with 10 or 14 electrons have $S=1$ in accordance with Hund's rule. When the dot molecule is formed, the spins of the individual dots are coupled antiferromagnetically. At short distances, however, a more complicated spin-density wave is favored.

Yannouleas and Landman (1999, 2000b) studied the spin structure of a molecule of two closed-shell dots with six electrons each, using the unrestricted Hartree-Fock approximation. For molecules consisting of nonmagic clusters, they reported zero total spin, indicating an antiferromagnetic coupling between the dots, in agreement with the results of Kolehmainen *et al.* (2000). Although an antiferromagnetic coupling between polarized quantum dots seems to dominate in dimers, we should note that the interaction is very weak and the energy difference between an antiferromagnetic state and a ferromagnetic state is very small, of the order of 1 meV (GaAs). Surprisingly, in a square of four quantum dots, with $4N=40$ electrons, the ground state was ferromagnetic, with the antiferromagnetic state being clearly higher in energy. Similarly a row of four dots had a ferromagnetic ground state (Kohlehmainen *et al.*, 2000).

A more realistic model for a lateral double dot was discussed by Nagaraja *et al.* (1999). They treated the

whole nanostructure, including gates and leads, in three-dimensional SDFT. The results show the splitting of the conductance peaks in excellent agreement with experiments.

B. Vertical double dots in the local spin-density approximation

In the case of vertical-dot molecules the system is inherently three dimensional. Nevertheless, each dot can be separately approximated by a two-dimensional system, if the distance between the two layers is large enough and the interdot correlation is taken into account properly. Rontani *et al.* (1999b) have used a generalized Hubbard model to study the smallest double dots with up to six electrons and demonstrated the richness of the many-body states as a function of the interdot distance. It should be noted that if the distance between the dots becomes small, the situation approaches that of a single-layer dot with an extra degree of freedom: The electrons at different layers have different "isospins" or "pseudospins" (Hawrylak and Palacios, 1995), as long as they still belong to different layers.

Partoens and Peeters (2000) assumed each layer to be two dimensional and used the LSDA within the layers, while describing the actual overlap between electrons in different layers with a Hubbard-like term. In practice this is done with an energy shift between symmetric and antisymmetric single-particle states. In addition to those terms coming from individual layers, the effective potential includes the interdot Coulomb potential. In principle, the effective potential should also include interdot correlation, but there is no simple way to approximate it. The interdot correlation can play an important role in the low-density limit where, for example, the Wigner molecules of each dot are strongly correlated (Baker and Rojo, 2001). The results of Partoens and Peeters (2000) show that at small distances the addition energy as a function of the electron number is similar to that for a single dot, in qualitative agreement with experimental results of Austing *et al.* (1998); see Fig. 58. When the interdot distance increases, the addition energy spectra depend sensitively on the level crossings of the molecular levels. A monotonic trend as a function of the interdot distance could not be observed. The situation is similar to the effect of deformation on the addition spectra of a single dot, studied in Sec. III.I.

Recently, Pi *et al.* (1998, 2001) have studied the vertical double dot using a three-dimensional LSDA model and making detailed comparisons with experimental addition energy spectra. They observe that when the interdot distance is small, the spectrum is similar to that of a single dot, as expected. When the dot-dot distance increases, the spectrum becomes more complicated until the molecule "dissociates." At intermediate distances a strong addition energy peak is observed at $N=8$ corresponding to two four-electron dots with $S=1$ in each, according to Hund's rule.

The comparison with experiment is complicated by the fact that real dots are not identical. Moreover, since

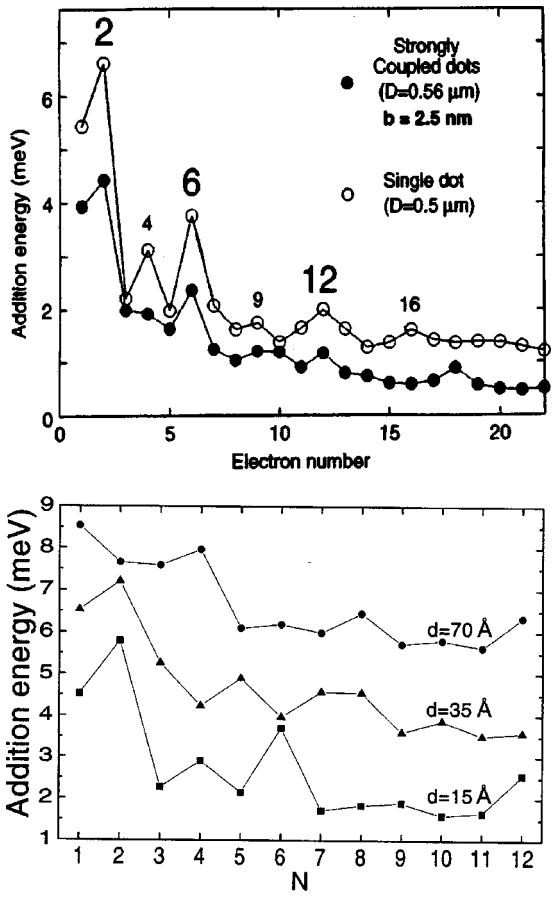

FIG. 58. Energy spectra for vertical double dots: Upper panel, experimental (Austing *et al.*, 1998); lower panel, calculated (Partoens and Peeters, 2000). In the upper panel, D is the dot diameter and b the interdot distance, while in the lower panel d is the interdot distance.

molecules with different interdot distances are fabricated separately, the mismatch differs from molecule to molecule and can also depend on the number of electrons. Pi *et al.* (2001) studied in detail the effect of the mismatch of the confining potentials of the two dots. With a reasonable mismatch, of the order of 1 meV, they were able to reproduce most features of the experimental addition energy spectra.

The results of Pi *et al.* (2001) provide confirmation of the conclusions of Partoens and Peeters (2000). More recently, the latter authors extended their studies to magnetic fields, making use of the CSDFT approach. They showed that compared to a single quantum dot, the spin-polarized maximum-density droplet has a significantly reduced stability (Partoens and Peeters, 2001), as was also observed experimentally (Austing *et al.*, 2001).

C. Exact results for vertical-dot molecules in a magnetic field

The exact diagonalization technique (configuration-interaction method) for a double-dot system is even more demanding than for a single dot. The single-

particle levels will be doubled and the configuration space increases due to the "isospin," i.e., the extra degree of freedom provided by the fact that the electrons can belong to different layers (Hawrylak and Palacios, 1995). Consequently the total number of electrons that can be treated accurately is smaller than in the case of a single dot.

Hawrylak and Palacios (1995) studied isospin effects in double dots with $N \leqslant 6$ in a strong magnetic field. For significant interdot correlations, minimum-isospin states were found.

Imamura *et al.* (1996, 1999) studied a vertical-dot system with three and four electrons using the exact diagonalization method. The dots were assumed to be two-dimensional harmonic traps and the Fock-Darwin states were used as a single-particle basis in each dot. The tunneling between the dots was included with a Hubbard-type hopping term in which the energy parameter describes the energy gap between symmetric and antisymmetric molecular orbitals made out of the single-dot states. The interdot Coulomb interaction was explicitly included without any further approximations. The results show the effect of the extra degree of freedom provided by the second dot. If the distance between the dots is small, all the electrons are correlated. In the case of large distances, however, the interdot Coulomb correlation is weak and the dots become independent. As a function of magnetic field the ground state of the small double-dot system changes similarly to that in a single dot, but the jumps in the total spin and angular momentum happen at slightly different places. The strong-field case is again dominated by magic angular momentum values associated with the localization of electrons in the double dot.

Imamura *et al.* (1999) also studied the case in which the confining potentials of the two dots have different strengths. This causes one set of single-particle states to be higher in energy than the other. Since this effect is similar to the Zeeman splitting of spin states in a magnetic field, it can be called a "pseudospin Zeeman splitting" (Hawrylak and Palacios, 1995). The results of Imamura *et al.* (1999) show that the pseudospin Zeeman splitting causes complicated transitions of the spin and angular momentum as a function of magnetic field.

D. Lateral-dot molecules in a magnetic field

In an external magnetic field the electronic structure of a dot molecule shows transitions as a function of the field strength that are similar to those in an individual dot. Kolehmainen *et al.* (2000) studied the two-dot molecule with ten electrons in each dot using CSDFT. As discussed above, in zero field the individual dots have spin $S=1$. In a molecule they form an antiferromagnet. At large interdot distances the energy difference between the antiferromagnetic and ferromagnetic states disappears and an infinitesimal field changes the antiferromagnetic state into a ferromagnetic one. Surprisingly, when the distance between the dots is small, an increasing magnetic field changes the antiferromagnetic state

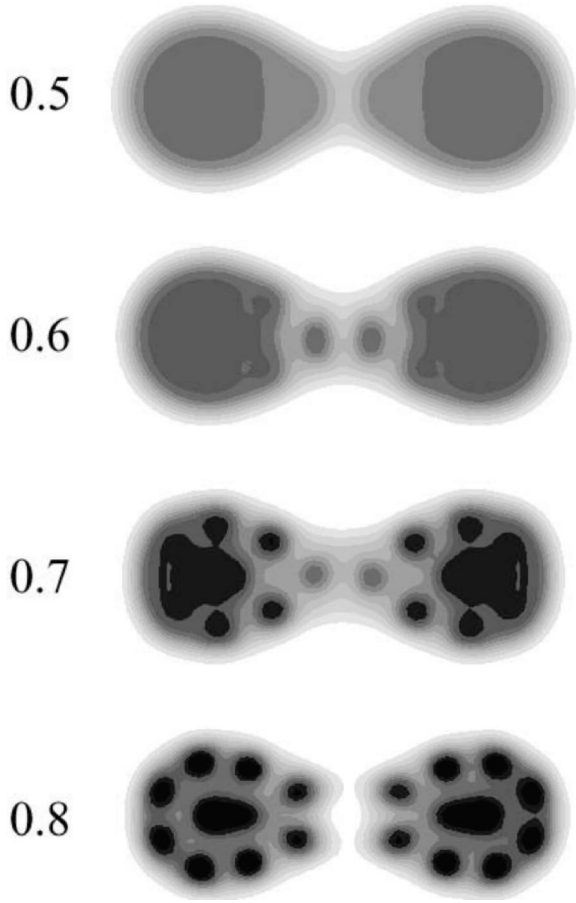

FIG. 59. Dependence of the ground-state electron density (obtained in current-spin-density-functional theory) on the magnetic field $B=0.5$ T*, . . . ,0.8 T* in a quantum dot molecule with $10+10$ electrons. The equidensity contours are shown using material parameters for GaAs, $T^*=6.68$ T. From Kolehmainen *et al.*, 2000.

first to a nonmagnetic state (with zero spin density). Only for stronger fields does the state become ferromagnetic and eventually fully polarized. The dot molecule forms two maximum-density droplets at about the same field strength as a single dot. When the field is increased further, the Chamon-Wen edge begins to separate from the individual maximum-density droplets. In the dot molecule the localization of electrons begins in the neck region as shown in Fig. 59.

Oosterkamp *et al.* (1998) demonstrated that with conductance measurements one can study changes of the magnetization in a double-dot system.

While a qualitative understanding can be reached in the single-particle picture or mean-field theories, measurements of magnetic interactions between the many-body states of quantum dots appear to be so sensitive that we still have a long way to go before reaching a quantitative understanding of the magnetic order in more complex quantum dot molecules.

X. SUMMARY

Finite nanoscale quantal systems exhibit a high potential for employing quantum electronics in technology

and continue to be a fast-growing area of study in condensed-matter physics. New spectroscopic methods applied to a large variety of man-made quantum systems open up new possibilities for studing basic many-body phenomena, having at the same time far-reaching prospects for applications. Such technological innovations, however, clearly require a profound expansion of our basic theoretical understanding of many-body effects in finite quantal systems. Artificial atoms provide many exciting opportunities for investigating the physical properties of many-particle systems with reduced dimensions: experiments have in the past revealed many surprises (for example, the occurrence of new phases) and certainly many new phenomena will be discovered in the future.

Much of the theoretical modeling of artificial atoms reviewed here was based on density-functional theory. For small vertical dots with azimuthal symmetry, a comparison of measured addition energies (i.e., the energies needed to put additional electrons sequentially into the dot) with the results of density-functional calculations confirmed that, as in atoms, the electronic structure is systematically determined by the subsequent filling of shells, obeying Hund's rules. Closed shells are particularly stable, i.e., the addition energy is large, implying the existence of a "noble-gas" structure for certain numbers of electrons. The orbital degeneracy of the oscillator shells can lead to spin alignment, resulting in maximized addition energies also at the midshell configuration.

Surprisingly, we have seen that, even in the absence of external magnetic fields, different types of magnetic ground states can exist: even in cases where one should expect nonmagnetic behavior, static spin-density waves were found even for rather moderate densities of the two-dimensional electron gas. Such spin ordering in the ground state is particularly pronounced for quasi-one-dimensional quantum rings, where up and down spins are regularly arranged in antiferromagnetic order. Regarding the many approximations that density-functional calculations inevitably include, a more detailed comparison to the results of full many-body calculations was needed to validate this surprising mean-field result. In the many-body approach the states with internally broken symmetry were discovered from an analysis of rotational spectra obtained by exact diagonalization. For quantum rings, the fact that the electrons are rather rigidly arranged in a lattice with antiferromagnetic order in the ground state could be understood from an analysis of the rotational and vibrational excitations.

Studies within density-functional theory also showed that changing the dot geometry may lead to piezomagnetic behavior: the total spin of a quantum dot changes as a function of the deformation of the dot.

When a magnetic field is applied perpendicular to the plane of the quasi-two-dimensional electron droplet, the chemical potential is significantly modified as the field strength is increased. For different densities and magnetic fields, the experimental data show clear traces of the Coulomb blockade peak positions, which allow the identification of transitions to different phases when going from the weak-field limit to the quantum Hall regime. Above a certain strength of the magnetic field, a compact droplet, in which the electrons occupy adjacent orbitals with consecutive angular momentum, is reconstructed by separating rings of charge density. These rings consist of nearly localized electrons. The phase boundaries between transitions from the nonpolarized to the polarized regime, where the droplet is compact, and the reconstruction regime in the high-field limit, where the electrons localize, are in qualitative agreement with experimental results.

Either at a low electron density or in a strong magnetic field, the many-body correlations dominate, as manifested, for example, by the localization of electrons in Wigner molecules. In the smallest systems the localization is understood qualitatively as an internal property of the exact many-body state.

ACKNOWLEDGMENTS

We thank Matti Koskinen and Ben Mottelson for fruitful collaboration during the last several years. Numerous discussions with them, as well as with Guy Austing, Rajat Bhaduri, Matthias Brack, Vidar Gudmundsson, Klavs Hansen, Wolfgang Häusler, Georgios Kavoulakis, Jere Kolehmainen, Poul-Erik Lindelof, Daniela Pfannkuche, Seigo Tarucha, Susanne Viefers, Andreas Wacker, Sven Åberg, and many others, helped us to shape our understanding of artificial atoms, as reflected in this review. We acknowledge financial support by the Bayerische Staatsministerium für Wissenschaft, Forschung und Kunst, NORDITA, the Academy of Finland, the Swedish Research Council, and the Swedish Foundation for Strategic Research.

REFERENCES

Adamowski, J., M. Sobkowicz, B. Szafran, and S. Bednarek, 2000, Phys. Rev. B **62**, 4234.
Aharonov, Y., and D. Bohm, 1959, Phys. Rev. **115**, 485.
Alder, K., A. Bohr, T. Huus, B. Mottelson, and A. Winther, 1956, Rev. Mod. Phys. **28**, 432.
Aleiner, I. L., P. W. Brouwer, and L. I. Glazman, 2002, Phys. Rep. **358**, 309.
Alhassid, Y., 2000, Rev. Mod. Phys. **72**, 895.
Alivisatos, A. P., 1996, Science **271**, 933.
Altshuler, B. L., P. A. Lee, and R. A. Webb, 1991, *Mesoscopic Phenomena in Solids* (North-Holland, Amsterdam).
Anderson, P. W., 1961, Phys. Rev. **124**, 41.
Ando, T., A. B. Fowler, and F. Stern, 1982, Rev. Mod. Phys. **54**, 437.
Ashoori, R. C., 1996, Nature (London) **379**, 413.
Ashoori, R. C., R. H. Silsbee, L. N. Pfeiffer, and K. W. West, 1992, in *Nanostructures and Mesoscopic Systems*, Proceedings of the Int. Symp. Santa Fe, May, 1991, edited by M. Reed and W. Kirk (Academic, San Diego).
Ashoori, R. C., H. L. Störmer, J. S. Weiner, L. N. Pfeiffer, K. W. Baldwin, and K. W. West, 1993, Phys. Rev. Lett. **71**, 613.

Ashoori, R. C., H. L. Störmer, J. S. Weiner, L. N. Pfeiffer, S. J. Pearton, K. W. Baldwin, and K. W. West, 1992, Phys. Rev. Lett. **68**, 3088.
Austing, D. G., T. Honda, K. Muraki, Y. Tokura, and S. Tarucha, 1998, Physica B **249-251**, 206.
Austing, D. G., T. Honda, and S. Tarucha, 1996, Semicond. Sci. Technol. **11**, 388.
Austing, D. G., T. Honda, and S. Tarucha, 1997, Jpn. J. Appl. Phys., Part 1 **36**, 1667.
Austing, D. G., S. Sasaki, S. Tarucha, S. M. Reimann, M. Koskinen, and M. Manninen, 1999, Phys. Rev. B **60**, 11 514.
Austing, D. G., H. Tamura, Y. Tokura, K. Muraki, S. Amaha, K. Ono, and S. Tarucha, 2001, Physica E (Amsterdam) **10**, 112.
Austing, D. G., Y. Tokura, T. Honda, S. Tarucha, M. Danoesastro, J. Janssen, T. H. Oosterkamp, and L. P. Kouwenhoven, 1999, Jpn. J. Appl. Phys., Part 1 **38**, 372.
Austing, D. G., Y. Tokura, S. Tarucha, P. Matagne, and J. P. Leburton, 2000, Physica E (Amsterdam) **11**, 63.
Averin, D. V., and K. K. Likharev, 1986, J. Low Temp. Phys. **62**, 345.
Averin, D. V., and K. K. Likharev, 1991, in *Mesoscopic Phenomena in Solids*, edited by B. I. Altshuler, P. A. Lee, and R. A. Webb (Elsevier, Amsterdam), p. 167.
Baker, J., and A. G. Rojo, 2001, J. Phys.: Condens. Matter **13**, 5313.
Balian, R., and C. Bloch, 1970, Ann. Phys. (N.Y.) **60**, 401.
Balian, R., and C. Bloch, 1971, Ann. Phys. (N.Y.) **63**, 592.
Balian, R., and C. Bloch, 1972, Ann. Phys. (N.Y.) **69**, 76.
Bao, C. G., 1997, Phys. Rev. Lett. **79**, 3475.
Baranger, H. U., and R. M. Westervelt, 1998, Chapter 14 in *Nanotechnology*, edited by G. Timp (Springer, New York), p. 537.
Bawendi, M. G., M. L. Steigerwald, and L. E. A. Brus, 1990, Annu. Rev. Phys. Chem. **41**, 447.
Beck, D. E., 1984, Solid State Commun. **49**, 381.
Bedanov, V. M., and F. M. Peeters, 1994, Phys. Rev. B **49**, 2667.
Bednarek, S., B. Szafran, and J. Adamowski, 1999, Phys. Rev. B **59**, 13036.
Beenakker, C. W. J., 1991, Phys. Rev. B **44**, 1646.
Beenakker, C. W. J., and H. van Houten, 1991, in *Solid State Physics*, edited by H. Ehrenreich and D. Turnbull (Academic, New York), Vol. 44, p. 1.
Bertsch, G. F., and T. Papenbrock, 1999, Phys. Rev. Lett. **83**, 5412.
Bimberg, D., M. Grundmann, and N. N. Ledentsov, 1999, *Quantum Dot Heterostructures* (Wiley, Chichester/New York).
Blick, R. H., R. J. Haug, J. Weis, D. Pfannkuche, K. v. Klitzing, and K. Eberl, 1996, Phys. Rev. B **53**, 7899.
Blick, R. H., D. Pfannkuche, R. J. Haug, K. v. Klitzing, and K. Eberl, 1998, Phys. Rev. Lett. **80**, 4032.
Bloch, F., 1972, Phys. Rev. B **2**, 109.
Bøggild, P., A. Kristensen, H. Bruus, S. M. Reimann, and P. E. Lindelof, 1998, Phys. Rev. B **57**, 15 408.
Bohr, Å., and B. R. Mottelson, 1953, Mat. Fys. Medd. K. Dan. Vidensk. Selsk. **27**, 16.
Bohr, Å., and B. R. Mottelson, 1975, *Nuclear Structure* (World Scientific, New York).
Bolton, F., 1994a, Solid-State Electron. **37**, 1159.
Bolton, F., 1994b, Phys. Rev. Lett. **73**, 158.
Bolton, F., 1996, Phys. Rev. B **54**, 4780.
Bolton, F., and U. Rössler, 1993, Superlattices Microstruct. **13**, 139.
Brack, M., 1993, Rev. Mod. Phys. **65**, 677.
Brack, M., and Bhaduri, R. K., 1997, *Semiclassical Physics* (Addison-Wesley, Reading, MA).
Brack, M., J. Blaschke, S. C. Creagh, A. G. Magner, P. Meier, and S. M. Reimann, 1997, Z. Phys. D: At., Mol. Clusters **40**, 276.
Brack, M., J. Damgaard, A. S. Jensen, H. C. Pauli, V. M. Strutinsky, and C. Y. Wong, 1972, Rev. Mod. Phys. **44**, 320.
Brey, L., N. F. Johnson, and B. I. Halperin, 1989, Phys. Rev. B **40**, 10647.
Brodsky, M., N. B. Zhitenev, R. C. Ashoori, L. N. Pfeiffer, and K. W. West, 2000, Phys. Rev. Lett. **85**, 2356.
Bruce, N. A., and P. A. Maksym, 2000, Phys. Rev. B **61**, 4718.
Brunner, K., U. Bockelmann, G. Abstreiter, M. Walther, G. Böhm, G. Tränkle, and G. Weimann, 1992, Phys. Rev. Lett. **69**, 3216.
Bryant, G. W., 1987, Phys. Rev. Lett. **59**, 1140.
Büttiker, M., 1985, Phys. Rev. B **32**, 1846.
Büttiker, M., Y. Imry, and R. Landauer, 1983, Phys. Lett. **96A**, 365.
Burkhard, G., D. Loss, and D. P. Di Vincenzo, 1999, Phys. Rev. B **59**, 2070.
Butler, P. A., and W. Nazarewicz, 1996, Rev. Mod. Phys. **68**, 349.
Butts, D. A., and D. S. Rokhsar, 1999, Nature (London) **397**, 327.
Byers, N., and C. N. Yang, 1961, Phys. Rev. Lett. **7**, 46.
Campbell, L. J., and R. M. Ziff, 1979, Phys. Rev. B **20**, 1886.
Canali, C. M., 2000, Phys. Rev. Lett. **84**, 3934.
Capelle, K., and G. Vignale, 2001, Phys. Rev. Lett. **86**, 5546.
Ceperley, D. M., and B. J. Alder, 1980, Phys. Rev. Lett. **45**, 566.
Chakraborty, T., 1992, Comments Condens. Matter Phys. **16**, 35.
Chakraborty, T., 1999, *Quantum Dots: A Survey of the Properties of Artificial Atoms* (North-Holland, Amsterdam).
Chakraborty, T., and P. Pietiläinen, 1994, Phys. Rev. B **50**, 8460.
Chakraborty, T., and P. Pietiläinen, 1995, Phys. Rev. B **52**, 1932.
Chang, L. L., L. Esaki, W. E. Howard, and R. Ludeke, 1973, J. Vac. Sci. Technol. **10**, 11.
Chang, L. L., L. Esaki, and R. Tsu, 1974, Appl. Phys. Lett. **24**, 593.
Chen, G., G. Klimeck, S. Datta, G. Chen, and W. A. Goddard III, 1994, Phys. Rev. B **50**, 8035.
Chengguang, B., R. Wenying, and L. Youyang, 1996, Phys. Rev. B **53**, 10 820.
Chou, M. Y., A. Cleland, and M. L. Cohen, 1984, Solid State Commun. **52**, 645.
Chui, S. T., and B. Tanatar, 1995, Phys. Rev. Lett. **74**, 458.
Ciorga, M., A. S. Sachrajda, P. Hawrylak, C. Gould, P. Zawadzki, S. Jullian, Y. Feng, and Z. Wasilewski, 2000, Phys. Rev. B **61**, R16 315.
Cooper, N. R., and N. K. Wilkin, 1999, Phys. Rev. B **60**, R16 279.
Cornell, E. A., 2001, Nobel Lecture. See http://www.nobel.se/physics/laureates/2001/cornell-lecture.html
Creffield, C. E., W. Häusler, J. H. Jefferson, and S. Sarkar, 1999, Phys. Rev. B **59**, 10 719.
Dalfovo, F., S. Giorgini, L. P. Pitaevskii, and S. Stringari, 1999, Rev. Mod. Phys. **71**, 463.
Darnhofer, T., and U. Rössler, 1993, Phys. Rev. B **47**, 16 020.
Darwin, C. G., 1930, Proc. Cambridge Philos. Soc. **27**, 86.

Date, G., M. V. N. Murthy, and R. Vathsan, 1998, J. Phys.: Condens. Matter **10**, 5876.
Davidocvić, D., and M. Tinkham, 1999, Phys. Rev. Lett. **83**, 1644.
de Chamon, C., and X. G. Wen, 1994, Phys. Rev. B **49**, 8227.
de Heer, W., 1993, Rev. Mod. Phys. **65**, 611.
Dean, D. J., M. R. Strayer, and J. C. Wells, 2001, Phys. Rev. B **64**, 125305.
Dellow, M. W., P. H. Beton, M. Henini, P. C. Main, and L. Eaves, 1991, Electron. Lett. **27**, 134.
Delsing, P., K. K. Likharev, L. S. Kuzmin, and T. Claeson, 1989a, Phys. Rev. Lett. **63**, 1180.
Delsing, P., K. K. Likharev, L. S. Kuzmin, and T. Claeson, 1989b, Phys. Rev. Lett. **63**, 1861.
Demel, T., D. Heitmann, P. Grambow, and K. Ploog, 1990, Phys. Rev. Lett. **64**, 788.
Dempsey, J., B. Y. Gelfand, and B. I. Halperin, 1993, Phys. Rev. Lett. **70**, 3639.
Deo, P. S., 1995, Phys. Rev. B **51**, 5441.
Deo, P. S., 1996, Phys. Rev. B **53**, 15 447.
Dineykhan, M., and R. G. Nazmitdinov, 1997, Phys. Rev. B **55**, 13 707.
Dingle, R., A. C. Gossard, and W. Wiegmann, 1974, Phys. Rev. Lett. **33**, 827.
Dixon, D., L. P. Kouwenhoven, P. L. McEuen, Y. Nagamune, J. Motohisa, and H. Sakaki, 1996, Phys. Rev. B **53**, 12 625.
Dreizler, R. M., and E. K. U. Gross, 1990, *Density Functional Theory* (Springer, Berlin).
Drexler, H., D. Leonard, W. Hansen, J. P. Kotthaus, and P. M. Petroff, 1994, Phys. Rev. Lett. **73**, 2252.
Eckardt, C., 1935, Phys. Rev. **47**, 552.
Egger, R., W. Häusler, C. H. Mak, and H. Grabert, 1999, Phys. Rev. Lett. **82**, 3320.
Ekardt, W., 1984, Phys. Rev. B **29**, 1558.
Ekardt, W., 1999, *Metal Clusters* (Wiley, New York).
El-Said, M., 1996, Phys. Status Solidi B **193**, 105.
Esaki, L., and L. L. Chang, 1974, Phys. Rev. Lett. **33**, 495.
Esaki, L., and R. Tsu, 1970, IBM J. Res. Dev. **14**, 61.
Eto, M., 1997, Jpn. J. Appl. Phys., Part 1 **36**, 3924.
Eto, M., 1999, Jpn. J. Appl. Phys., Part 1 **38**, 376.
Ezaki, T., N. Mori, and C. Hamaguchi, 1997, Phys. Rev. B **56**, 6428.
Ezaki, T., Y. Sugimoto, N. Mori, and C. Hamaguchi, 1998a, Physica B **249-251**, 238.
Ezaki, T., Y. Sugimoto, N. Mori, and C. Hamaguchi, 1998b, Semicond. Sci. Technol. **13**, A1.
Fano, G., and F. Ortolani, 1988, Phys. Rev. B **37**, 8179.
Ferconi, M., and G. Vignale, 1994, Phys. Rev. B **50**, 14 722.
Ferconi, M., and G. Vignale, 1997, Phys. Rev. B **56**, 12 108.
Filinov, A. V., M. Bonitz, and Yu. E. Lozovik, 2001, Phys. Rev. Lett. **86**, 3851.
Fock, V., 1928, Z. Phys. **47**, 446.
Fonseca, L. R. C., J. L. Jimenez, J. P. Leburton, R. M. Martin, 1998, Phys. Rev. B **57**, 4017.
Foxman, E. B., P. L. McEuen, U. Meirav, N. S. Wingreen, Y. Meir, P. A. Belk, N. R. Belk, M. A. Kastner, and S. J. Wind, 1993, Phys. Rev. B **47**, 10 020.
Franceschetti, A., and A. Zunger, 2000, Europhys. Lett. **50** (2), 243.
Franco, M., and L. Brey, 1997, Phys. Rev. B **56**, 10 383.
Frauendorf, S., 2001, Rev. Mod. Phys. **73**, 463.
Fricke, M., A. Lorke, J. P. Kotthaus, G. Medeiros-Ribeiro, and P. M. Petroff, 1996, Europhys. Lett. **36**, 197.
Fujito, M., A. Natori, and H. Yasunaga, 1996, Phys. Rev. B **53**, 9952.
Fulton, T. A., and G. J. Dolan, 1987, Phys. Rev. Lett. **59**, 109.
Gammon, D., 2000, Nature (London) **405**, 899.
Geilikman, B. T., 1960, in *Proceedings of the International Conference on Nuclear Structure*, Kingston, Canada, edited by D. A. Branley and E. W. Vogt (University of Toronto, Toronto), p. 874.
Giaever, I., and H. R. Zeller, 1968, Phys. Rev. Lett. **20**, 1504.
Gilbert, T. L., 1975, Phys. Rev. B **12**, 2111.
Girvin, S. M., and T. Jach, 1983, Phys. Rev. B **28**, 4506.
Goeppert-Mayer, M., 1949, Phys. Rev. **75**, 1969.
Goldmann, E., and S. R. Renn, 1999, Phys. Rev. B **60**, 16 611.
González, A., L. Quiroga, and B. A. Rodriguez, 1996, Few-Body Syst. **21**, 47.
Goodings, C. J., J. R. A. Cleaver, and H. Ahmed, 1992, Electron. Lett. **28**, 1535.
Gorter, C. J., 1951, Physica (Amsterdam) **17**, 777.
Grabert, H., and M. H. Devoret, 1991, Eds., *Single Charge Tunneling* (Plenum, New York).
Groshev, A., 1990, Phys. Rev. B **42**, 5895.
Gross, E. K. U., E. Runge, and O. Heinonen, 1991, *Many Particle Theory* (Hilger, Bristol).
Grundmann, M., J. Christen, N. N. Ledentsov, J. Böhrer, D. Bimberg, S. Ruvimov, P. Werner, U. Richter, U. Gösele, J. Heydenreich, V. M. Ustinov, A. Yu. Egorov, A. E. Zhukov, P. S. Kopév, and Zh. I. Alferov, 1995, Phys. Rev. Lett. **74**, 4043.
Gudmundsson, V., A. Braatas, P. Grambow, B. Meurer, T. Kurth, and D. Heitmann, 1995, Phys. Rev. B **51**, 17 744.
Gudmundsson, V., and R. R. Gerhardts, 1991, Phys. Rev. B **43**, 12 098.
Gudmundsson, V., and J. J. Palacios, 1995, Phys. Rev. B **52**, 11 266.
Gudmundsson, V., and G. Pálsson, 1994, Phys. Scr. T **54**, 92.
Guéret, P., N. Blanc, R. Germann, and H. Rothuizen, 1992, Phys. Rev. Lett. **68**, 1896.
Gunnarsson, O., and B. I. Lunqvist, 1976, Phys. Rev. B **13**, 4274.
Häkkinen, H., J. Kolehmainen, M. Koskinen, P. O. Lipas, and M. Manninen, 1997, Phys. Rev. Lett. **78**, 1034.
Hamamoto, I., B. R. Mottelson, H. Xie, and X. Z. Zhang, 1991, Z. Phys. D: At., Mol. Clusters **21**, 163.
Hansen, W., T. P. Smith III, and K. Y. Lee, 1990, Phys. Rev. Lett. **64**, 1992.
Hansen, W., T. P. Smith III, K. Y. Lee, J. A. Brum, C. M. Knoedler, and D. P. Kern, 1989, Phys. Rev. Lett. **62**, 2168.
Hansen, W., *et al.*, 1990, Appl. Phys. Lett. **56**, 168.
Harju, A., V. A. Sverdlov, and R. M. Nieminen, 1999, Phys. Rev. B **59**, 5622.
Harting, J., O. Mülken, and P. Borrmann, 2000, Phys. Rev. B **62**, 10 207.
Häusler, W., 1994, Adv. Solid State Phys. **34**, 171.
Häusler, W., 2000, Europhys. Lett. **49**, 231.
Häusler, W., and B. Kramer, 1993, Phys. Rev. B **47**, 16 353.
Hawrylak, P., 1993, Phys. Rev. Lett. **71**, 3347.
Hawrylak, P., and J. J. Palacios, 1995, Phys. Rev. B **51**, 1769.
Hawrylak, P., and D. Pfannkuche, 1993, Phys. Rev. Lett. **70**, 485.
Haxel, O., J. H. D. Jensen, and H. E. Suess, 1949, Phys. Rev. B **75**, 1766.
Heinonen, O., J. M. Kinaret, and M. D. Johnson, 1999, Phys. Rev. B **59**, 8073.

Heinonen, O., M. I. Lubin, and M. D. Johnson, 1995, Phys. Rev. Lett. **75**, 4110.
Herzberg, G., 1945, *Infrared and Raman Spectra of Polyatomic Molecules* (Van Nostrand, New York).
Hintermann, A., and M. Manninen, 1983, Phys. Rev. B **27**, 7262.
Hirose, K., and N. Wingreen, 1999, Phys. Rev. B **59**, 4604.
Hofmann, F., T. Heinzel, D. A. Wharam, J. K. Kotthaus, G. Böhm, W. Klein, G. Tränkle, and G. Weimann, 1995, Phys. Rev. B **51**, 13 872.
Hohenberg, P., and W. Kohn, 1964, Phys. Rev. **136**, B864.
Hu, L., H. Li, and G. He, 2000, Phys. Rev. B **62**, 16 744.
Hubbard, J., 1963, Proc. R. Soc. London, Ser. A **276**, 238.
Hüller, A., and D. M. Kroll, 1975, J. Chem. Phys. **63**, 4495.
Hund, F., 1938, Ann. Phys. (Leipzig) **32**, 102.
Imamura, H., H. Aoki, and P. A. Maksym, 1998, Phys. Rev. B **57**, R4257.
Imamura, H., P. A. Maksym, and H. Aoki, 1996, Phys. Rev. B **53**, 12 613.
Imamura, H., P. A. Maksym, and H. Aoki, 1999, Phys. Rev. B **59**, 5817.
Jacak, L., P. Hawrylak, and A. Wójs, 1998, *Quantum Dots* (Springer, Berlin).
Jackson, A. D., G. M. Kavoulakis, B. Mottelson, and S. M. Reimann, 2001, Phys. Rev. Lett. **63**, 055602.
Jahn, H. A., and E. Teller, 1937, Proc. R. Soc. London, Ser. A **161**, 220.
Jain, J. K., 1989, Phys. Rev. Lett. **63**, 199.
Jain, J. K., and T. Kawamura, 1995, Europhys. Lett. **29**, 321.
Janak, J. F., 1978, Phys. Rev. B **18**, 7165.
Jauregui, K., W. Häusler, and B. Kramer, 1993, Europhys. Lett. **24**, 581.
Jayannavar, A. M., and P. S. Deo, 1995, Phys. Rev. B **51**, 10 175.
Jefferson, J. H., and W. Häusler, 1997, Mol. Phys. Rep. **17**, 81.
Jiang, T. F., Xiao-Min Tang, and Shih-I Chu, 2001, Phys. Rev. B **63**, 045317.
Johnson, A. T., L. P. Kouwenhoven, W. de Jung, N. C. van der Vaart, C. J. P. M. Harmans, and C. T. Foxon, 1992, Phys. Rev. Lett. **69**, 1592.
Johnson, N. F., 1992, Phys. Rev. B **46**, 2636.
Johnson, N. F., and M. C. Payne, 1991, Phys. Rev. Lett. **67**, 1157.
Johnson, N. F., and L. Quiroga, 1994, Solid State Commun. **89**, 661.
Johnson, N. F., and L. Quiroga, 1995, Phys. Rev. Lett. **74**, 4277.
Jones, R. O., and O. Gunnarsson, 1989, Rev. Mod. Phys. **61**, 689.
Jovanovic, D., and J. P. Leburton, 1994, Phys. Rev. B **49**, 7474.
Kamilla, R. K., and J. K. Jain, 1995, Phys. Rev. B **52**, 2798.
Karlhede, A., S. A. Kivelson, K. Lejnell, and S. L. Sondhi, 1996, Phys. Rev. Lett. **77**, 2061.
Karlhede, A., and K. Leijnell, 1997, Physica E (Amsterdam) **1**, 42.
Kash, J. A., M. Zachau, E. Mendez, J. M. Hong, and T. Fukuzawa, 1991, Phys. Rev. Lett. **66**, 2247.
Kastner, M. A., 1992, Rev. Mod. Phys. **64**, 849.
Kastner, M. A., 1993, Phys. Today **46** (1), 24.
Kavoulakis, G. M., B. Mottelson, and C. Pethick, 2000, Phys. Rev. A **62**, 063605.
Ketterle, W., 2001, Nobel lecture. See http://www.nobel.se/physics/laureates/2001/ketterle-lecture.html
Klein, O., C. de Chamon, D. Tang, D. M. Abusch-Magder, U. Meirav, X.-G. Wen, and M. Kastner, 1995, Phys. Rev. Lett. **74**, 785.
Klein, O., D. Goldhaber-Gordon, C. de C. Chamon, and M. A. Kastner, 1996, Phys. Rev. B **53**, R4221.
Klimeck, G., G. Chen, and S. Datta, 1994, Phys. Rev. B **50**, 2316.
Knight, W. D., K. Clemenger, W. A. de Heer, W. A. Saunders, M. Y. Chou, and M. L. Cohen, 1984, Phys. Rev. Lett. **52**, 2141.
Kohn, W., 1959, Phys. Rev. **115**, 1160.
Kohn, W., 1961, Phys. Rev. **123**, 1242.
Kohn, W., 1999, Rev. Mod. Phys. **71**, 1253.
Kohn, W., and L. J. Sham, 1965, Phys. Rev. **140**, A1133.
Kolagunta, V. R., D. B. Janes, G. L. Chen, K. J. Webb, and M. R. Melloch, 1995, Superlattices Microstruct. **17**, 339.
Kolehmainen, J., S. M. Reimann, M. Koskinen, and M. Manninen, 2000, Eur. Phys. J. B **13**, 731.
Kolomeisky, E. B., and J. P. Straley, 1996, Rev. Mod. Phys. **68**, 175.
Koopmans, T., 1933, Physica (Amsterdam) **1**, 104.
Korotkov, A. N., D. V. Averin, and K. K. Likharev, 1900, Physica B **165**, 927.
Koskinen, M., J. Kolehmainen, S. M. Reimann, J. Toivanen, and M. Manninen, 1999, Eur. Phys. J. D **9**, 487.
Koskinen, M., P. O. Lipas, and M. Manninen, 1994, Phys. Rev. B **49**, 8418.
Koskinen, M., M. Manninen, B. Mottelson, and S. M. Reimann, 2001, Phys. Rev. B **63**, 205323.
Koskinen, M., M. Manninen, and S. M. Reimann, 1997, Phys. Rev. Lett. **79**, 1389.
Kouwenhoven, L. P., D. G. Austing, and S. Tarucha, 2001, Rep. Prog. Phys. **64**, 701.
Kouwenhoven, L. P., and C. Marcus, 1998, Phys. World **11** (6), 35.
Kouwenhoven, L. P., C. M. Marcus, P. L. McEuen, S. Tarucha, R. M. Westervelt, and N. S. Wingreen, 1997, in *Mesoscopic Electron Transport*, Proceedings of the NATO Advanced Study Institute on Mesoscopic Electron Transport, Series E345, edited by L. L. Sohn, L. P. Kouwenhoven, and G. Schön (Kluwer, Dordrecht/Boston), p. 105.
Kouwenhoven, L. P., and P. L. McEuen, 1999, in *Nanotechnology*, edited by G. Timp (Springer, New York), p. 471.
Kouwenhoven, L. P., T. H. Oosterkamp, M. W. S. Danoesastro, M. Eto, D. G. Austing, T. Honda, and S. Tarucha, 1997, Science **278**, 1788.
Kouwenhoven, L. P., N. C. van der Vaart, A. T. Johnson, W. Kool, C. J. P. M. Harmans, J. G. Williamson, A. A. M. Staring, and C. T. Foxon, 1991, Z. Phys. B: Condens. Matter **85**, 367.
Kulik, I. O., and R. I. Shekhter, 1975, Zh. Eksp. Teor. Fiz. **68**, 623 [Sov. Phys. JETP **41**, 308].
Kumar, A., S. E. Laux, and F. Stern, 1990, Phys. Rev. B **42**, 5166.
Kuzmin, L. S., P. Delsing, T. Claeson, and K. K. Likharev, 1989, Phys. Rev. Lett. **62**, 2539.
Kuzmin, L. S., and K. K. Likharev, 1987, Pis'ma Zh. Eksp. Teor. Fiz. **45**, 250 [JETP Lett. **45**, 495].
Lai, Ying-Ju, and I. Lin, 1999, Phys. Rev. E **60**, 4743.
Lambe, J., and R. C. Jaklevic, 1969, Phys. Rev. Lett. **22**, 1371.
Landau, L., 1930, Z. Phys. **64**, 629.
Lang, N. D., and W. Kohn, 1970, Phys. Rev. B **1**, 4555.
Laughlin, R. B., 1983, Phys. Rev. B **27**, 3383.

Lebens, J. A., C. S. Tsai, K. J. Vahala, 1990, Appl. Phys. Lett. **56**, 2642.
Lee, D. H., and C. L. Kane, 1990, Phys. Rev. Lett. **64**, 1313.
Lee, I.-H., Yong-Hoon Kim, and Kang-Hun Ahn, 2001, J. Phys.: Condens. Matter **13**, 1987.
Lee, I.-H., V. Rao, R. M. Martin, and J.-P. Leburton, 1998, Phys. Rev. B **57**, 9035.
Leggett, A. J., 1991, in *Granular Nano-Electronics*, edited by D. K. Ferry, J. R. Barker, and C. Jacoboni, NATO Advanced Study Institute, Series B: Physics, Vol. 251 (Plenum, New York), p. 297.
Leggett, A. J., 2001, Rev. Mod. Phys. **73**, 307.
Leinaas, J. M., and S. Viefers, 1998, Nucl. Phys. B **520**, 675.
Levesque, D., J. J. Weis, and A. H. MacDonald, 1984, Phys. Rev. B **30**, 1056.
Levy, M., 1979, Proc. Natl. Acad. Sci. U.S.A. **76**, 6062.
Lieb, E., and D. Mattis, 1969, Phys. Rev. **125**, 164.
Lipparini, E., N. Barbéran, M. Barranco, M. Pi, and L. Serra, 1997, Phys. Rev. B **56**, 12 375.
Lipparini, E., and L. Serra, 1998, Phys. Rev. B **57**, R6830.
Lorke, A., M. Fricke, B. T. Miller, M. Haslinger, J. P. Kotthaus, G. Medeiros-Ribeiro, and P. M. Petroff, 1997, in *Compound Semiconductors 1996*, edited by M. S. Shur and R. A. Suris, IOP Conference Proceedings No. 155 (Institute of Physics, Bristol/Philadelphia), p. 803.
Lorke, A., J. P. Kotthaus, and K. Ploog, 1990, Phys. Rev. Lett. **64**, 2559.
Lorke, A., and R. J. Luyken, 1998, Physica B **256**, 424.
Loss, D., and D. P. Di Vincenzo, 1998, Phys. Rev. A **57**, 120.
Lozovik, Yu. E., and V. A. Mandelshtam, 1990, Phys. Lett. A **145**, 269.
Lozovik, Yu. E., and V. A. Mandelshtam, 1992, Phys. Lett. A **165**, 469.
Lubin, M. I., O. Heinonen, and M. D. Johnson, 1997, Phys. Rev. B **56**, 10 373.
Luyken, R. J., A. Lorke, M. Haslinger, B. T. Miller, M. Fricke, J. P. Kotthaus, G. Medeiros-Ribeiro, and P. M. Petroff, 1998, Physica E (Amsterdam) **2**, 704.
MacDonald, A. H., S. R. E. Yang, and M. D. Johnson, 1993, Aust. J. Phys. **46**, 345.
Macucci, M., K. Hess, and G. J. Iafrate, 1993, Phys. Rev. B **48**, 17 354.
Macucci, M., K. Hess, and G. J. Iafrate, 1995, J. Appl. Phys. **77**, 3267.
Macucci, M., K. Hess, and G. J. Iafrate, 1997, Phys. Rev. B **55**, R4879.
Mak, C. H., R. Egger, and H. Weber-Gottschick, 1998, Phys. Rev. Lett. **81**, 4533.
Maksym, P. A., 1993, Physica B **184**, 385.
Maksym, P. A., 1996, Phys. Rev. B **53**, 10 871.
Maksym, P. A., 1998, Physica B **249**, 233.
Maksym, P. A., and N. A. Bruce, 1997, Physica E (Amsterdam) **1**, 211.
Maksym, P. A., and T. Chakraborty, 1990, Phys. Rev. Lett. **65**, 108.
Maksym, P. A., and T. Chakraborty, 1992, Phys. Rev. B **45**, 1947.
Maksym, P. A., H. Imamura, G. P. Mallon, and H. Aoki, 2000, J. Phys.: Condens. Matter **12**, R299.
Manninen, M., 1986, Solid State Commun. **59**, 281.
Manninen, M., M. Koskinen, S. M. Reimann, and B. Mottelson, 2001, Eur. Phys. J. D **16**, 381.
Manninen, M., and R. Nieminen, 1978, J. Phys. F: Met. Phys. **8**, 2243.
Manninen, M., R. Nieminen, P. Hautojärvi, and A. Arponen, 1975, Phys. Rev. B **12**, 4012.
Manninen, M., S. Viefers, M. Koskinen, and S. M. Reimann, 2001, Phys. Rev. B **64**, 245322.
Martins, J. L., J. Buttet, and R. Car, 1985, Phys. Rev. B **31**, 1804.
Martins, J. L., R. Car, and J. Buttet, 1981, Surf. Sci. **106**, 265.
Marzin, J.-Y., J.-M. Gerard, A. Izrael, D. Barrier, and G. Bastard, 1994, Phys. Rev. Lett. **73**, 716.
Matagne, P., J. P. Leburton, D. G. Austing, and S. Tarucha, 2001, Phys. Rev. B **65**, 085325.
McEuen, P. L., 1997, Science **278**, 1729.
McEuen, P. L., E. B. Foxman, J. Kinaret, U. Meirav, M. A. Kastner, N. S. Wingreen, and S. J. Wind, 1992, Phys. Rev. B **45**, 11 419.
McEuen, P. L., E. B. Foxman, U. Meirav, M. A. Kastner, Y. Meir, N. S. Wingreen, and S. J. Wind, 1991, Phys. Rev. Lett. **66**, 1926.
McEuen, P. L., N. S. Wingreen, E. B. Foxman, J. Kinaret, U. Meirav, M. A. Kastner, Y. Meir, and S. J. Wind, 1993, Physica B **189**, 70.
Meir, Y., and N. S. Wingreen, 1992, Phys. Rev. Lett. **68**, 2512.
Meir, Y., N. S. Wingreen, and P. A. Lee, 1991, Phys. Rev. Lett. **66**, 3048.
Meirav, U., M. A. Kastner, and S. J. Wind, 1990, Phys. Rev. Lett. **65**, 771.
Meurer, B., D. Heitmann, and K. Ploog, 1992, Phys. Rev. Lett. **68**, 1371.
Miller, B. T., W. Hansen, S. Manus, R. J. Luyken, A. Lorke, J. P. Kotthaus, S. Huant, G. Medeiros-Ribeiro, and M. Petroff, 1997, Phys. Rev. B **56**, 6764.
Monnier, R., and J. P. Perdew, 1978, Phys. Rev. B **17**, 2595.
Morf, R., N. d'Ambrumenil, and B. I. Halperin, 1986, Phys. Rev. B **34**, 3037.
Morf, R., and B. J. Halperin, 1987, Z. Phys. B: Condens. Matter **68**, 391.
Mottelson, B., 1999, Phys. Rev. Lett. **83**, 2695.
Müller, H.-M., and S. E. Koonin, 1996, Phys. Rev. B **54**, 14 532.
Nagaraja, S., J.-P. Leburton, and R. M. Martin, 1999, Phys. Rev. B **60**, 8759.
Nagaraja, S., P. Matagne, V.-Y. Thean, J.-P. Leburton, Y.-H. Kim, and R. M. Martin, 1997, Phys. Rev. B **56**, 15 752.
Niemelä, K., P. Pietiläinen, P. Hyvönen, and T. Chakraborty, 1996, Europhys. Lett. **36**, 533.
Nilsson, S. G., 1955, Mat. Fys. Medd. K. Dan. Vidensk. Selsk. **29**, 16.
Nishioka, H., K. Hansen, and B. Mottelson, 1990, Phys. Rev. B **42**, 9377.
Niu, C., L. Liu, and T. Lin, 1995, Phys. Rev. B **51**, 5130.
Notzel, R., J. Temmo, A. Kozen, T. Tamamura, T. Fukui, and H. Hasegawa, 1995, Appl. Phys. Lett. **66**, 2525.
Oaknin, J. H., L. Martín-Moreno, J. J. Palacios, and C. Tejedor, 1995, Phys. Rev. Lett. **74**, 5120.
Oaknin, J. H., B. Paredes, L. Martín-Moreno, and C. Tejedor, 1997, Physica E (Amsterdam) **1**, 47.
Ohno, H., E. E. Mendez, J. A. Brum, J. M. Hong, F. Agulló-Rueda, L. L. Chang, and L. Esaki, 1990, Phys. Rev. Lett. **64**, 2555.
Oosterkamp, T. H., S. F. Godijn, M. J. Uilenreef, Y. V. Nazarov, N. C. van der Vaart, and L. P. Kouwenhoven, 1998, Phys. Rev. Lett. **80**, 4951.

Oosterkamp, T. H., J. W. Janssen, L. P. Kouwenhoven, D. G. Austing, T. Honda, and S. Tarucha, 1999, Phys. Rev. Lett. **82**, 2931.
Overhauser, A. W., 1960, Phys. Rev. Lett. **4**, 462.
Overhauser, A. W., 1962, Phys. Rev. **128**, 1437.
Overhauser, A. W., 1968, Phys. Rev. Lett. **167**, 691.
Palacios, J. J., L. Martín-Moreno, G. Chiappe, E. Louis, and C. Tejedor, 1994, Phys. Rev. B **50**, 5760.
Palacios, J. J., L. Martín-Moreno, and C. Tejedor, 1993, Europhys. Lett. **23**, 495.
Partoens, B., and F. M. Peeters, 2000, Phys. Rev. Lett. **84**, 4433.
Partoens, B., and F. M. Peeters, 2001, Physica B **298**, 282.
Pederiva, F., C. J. Umrigar, and E. Lipparini, 2000, Phys. Rev. B **62**, 8120.
Pedersen, J., S. Bjørnholm, J. Borggreen, K. Hansen, T. P. Martin, and H. D. Rasmussen, 1991, Nature (London) **353**, 733.
Peierls, R. E., and D. J. Thouless, 1962, Nucl. Phys. **38**, 154.
Peierls, R. E., and J. Yoccoz, 1957, Proc. R. Soc. London, Ser. A **70**, 381.
Perdew, J. P., and A. Zunger, 1981, Phys. Rev. B **23**, 5048.
Persson, M., P. E. Lindelof, B. von Sydow, J. Pettersson, and A. Kristensen, 1995, J. Phys.: Condens. Matter **7**, 3733.
Persson, M., J. Pettersson, A. Kristensen, and P. E. Lindelof, 1994, Physica B **194**, 1273.
Persson, M., J. Pettersson, B. von Sydow, P. E. Lindelof, A. Kristensen, and K. F. Berggreen, 1995, Phys. Rev. B **52**, 8921.
Pethick, C. J., and H. Smith, 2002, *Bose-Einstein Condensation in Dilute Gases* (Cambridge, England).
Petroff, P. M., and S. P. Denbaars, 1994, Superlattices Microstruct. **15**, 15.
Petroff, P. M., A. Lorke, and A. Imamoglu, 2001, Phys. Today **54** (5), 46.
Pfannkuche, D., R. R. Gerhardts, P. A. Maksym, and V. Gudmundsson, 1993, Physica B **189**, 6.
Pfannkuche, D., V. Gudmundsson, P. Hawrylak, and R. R. Gerhardts, 1994, Solid-State Electron. **37**, 1221.
Pfannkuche, D., V. Gudmundsson, and P. A. Maksym, 1993, Phys. Rev. B **47**, 2244.
Pfeiffer, L., K. W. West, H. L. Stormer, J. P. Eisenstein, K. W. Baldwin, D. Gershoni, and J. Spector, 1990, Appl. Phys. Lett. **56**, 1697.
Pi, M., M. Barranco, A. Emperador, E. Lipparini, and Ll. Serra, 1998, Phys. Rev. B **57**, 14 783.
Pi, M., A. Emperador, M. Barranco, F. Garcias, K. Muraki, S. Tarucha, and D. G. Austing, 2001, Phys. Rev. Lett. **87**, 066801.
Pople, J. A., 1999, Rev. Mod. Phys. **71**, 1267.
Prange, E., and S. M. Girvin, 1990, Eds., *The Quantum Hall Effect* (Springer-Verlag, New York).
Price, R., and S. Das Sarma, 1996, Phys. Rev. B **54**, 8033.
Puente, A., and L. Serra, 1999, Phys. Rev. Lett. **83**, 3266.
Quiroga, L., D. Ardila, and N. F. Johnson, 1993, Solid State Commun. **86**, 775.
Ralph, D. C., C. T. Black, and M. Tinkham, 1997, Phys. Rev. Lett. **78**, 4087.
Rapisarda, F., and G. Senatore, 1996, Aust. J. Phys. **49**, 161.
Rasolt, M., and F. Perrot, 1992, Phys. Rev. Lett. **69**, 2563.
Reed, M. A., 1993, Sci. Am. (Int. Ed.) **268** (1), 98.
Reed, M. A., J. N. Randall, R. J. Aggarwall, R. J. Matyi, T. M. Moore, and A. E. Wetsel, 1988, Phys. Rev. Lett. **60**, 535.
Reimann, S. M., M. Koskinen, H. Häkkinen, P. E. Lindelof, and M. Manninen, 1997, Phys. Rev. B **56**, 12 147.
Reimann, S. M., M. Koskinen, J. Helgesson, P. E. Lindelof, and M. Manninen, 1998, Phys. Rev. B **58**, 8111.
Reimann, S. M., M. Koskinen, J. Kolehmainen, M. Manninen, D. G. Austing, and S. Tarucha, 1999, Eur. Phys. J. D **9**, 105.
Reimann, S. M., M. Koskinen, P. E. Lindelof, and M. Manninen, 1998, Physica E (Amsterdam) **2**, 648.
Reimann, S. M., M. Koskinen, and M. Manninen, 1999, Phys. Rev. B **59**, 1613.
Reimann, S. M., M. Koskinen, and M. Manninen, 2000, Phys. Rev. B **62**, 8108.
Reimann, S. M., M. Koskinen, M. Manninen, and B. Mottelson, 1999, Phys. Rev. Lett. **83**, 3270.
Reimann, S. M., M. Persson, P. E. Lindelof, and M. Brack, 1996, Z. Phys. B: Condens. Matter **101**, 377.
Reusch, B., W. Häsler, and H. Grabert, 2001, Phys. Rev. B **63**, 113313.
Ring, P., and P. Schuck, 1980, *The Nuclear Many-Body Problem* (Springer, New York), p. 438ff.
Rontani, M., F. Rossi, F. Manghi, and E. Molinari, 1999a, Phys. Rev. B **59**, 10 165.
Rontani, M., F. Rossi, F. Manghi, and E. Molinari, 1999b, Solid State Commun. **112**, 151.
Ruan, W. Y., Y. Y. Liu, C. G. Bao, and Z. Q. Zhang, 1995, Phys. Rev. B **51**, 7942.
Saint Jean, M., C. Even, and C. Guthmann, 2001, Europhys. Lett. **55**, 45.
Sakaki, H., 1980, Jpn. J. Appl. Phys., Part 2 **19**, L735.
Schedelbeck, G., W. Wegscheider, M. Bichler, and G. Abstreiter, 1997, Science **278**, 1792.
Schmidt, T., R. J. Haug, K. v. Klitzing, A. Förster, and H. Lüth, 1997, Phys. Rev. Lett. **78**, 1544.
Schmidt, T., M. Tewordt, R. H. Blick, R. J. Haug, D. Pfannkuche, K. v. Klitzing, A. Förster, and H. Lüth, 1995, Phys. Rev. B **51**, 5570.
Schulte, F. K., 1974, J. Phys. C **7**, L370.
Schulte, F. K., 1977, Z. Phys. B **27**, 303.
Schulz, H. J., 1993, Phys. Rev. Lett. **71**, 1864.
Schweigert, V. A., and F. M. Peeters, 1994, Superlattices Microstruct. **16**, 243.
Schweigert, V., and F. M. Peeters, 1995, Phys. Rev. B **51**, 7700.
Scott-Thomas, J. H. F., S. B. Field, M. A. Kastner, H. I. Smith, and D. A. Antonadius, 1989, Phys. Rev. Lett. **62**, 583.
Seki, T., Y. Kuramoto, and T. Nishino, 1996, J. Phys. Soc. Jpn. **65**, 3945.
Serra, L., M. Barranco, A. Emperador, M. Pi, and E. Lipparini, 1998, Phys. Rev. B **59**, 15 290.
Serra, L., and E. Lipparini, 1997, Europhys. Lett. **40**, 667.
Serra, L., A. Puente, and E. Lipparini, 1999, Phys. Rev. B **60**, R13 966.
Shumway, J., L. R. C. Fonseca, J. P. Leburton, R. M. Martin, and D. M. Ceperley, 2000, Physica E (Amsterdam) **8**, 260.
Sikorski, C., and U. Merkt, 1989, Phys. Rev. Lett. **62**, 2164.
Silsbee, R. H., and R. C. Ashoori, 1990, Phys. Rev. Lett. **64**, 1991.
Skyrme, T. H. R., 1961, Proc. R. Soc. London, Ser. A **626**, 233.
Smith, T. P., III, H. Arnot, J. M. Hong, C. M. Knoedler, S. E. Laux, and H. Schmid, 1987, Phys. Rev. Lett. **59**, 2802.
Smith, T. P., III, K. Y. Lee, C. M. Knoedler, J. M. Hong, and D. P. Kern, 1988, Phys. Rev. B **38**, 2172.
Sondhi, S. L., A. Karlhede, S. A. Kivelson, and E. H. Rezayi, 1993, Phys. Rev. B **47**, 16 419.
Stafford, C. A., and S. Das Sarma, 1994, Phys. Rev. Lett. **72**, 3590.

Steffens, O., U. Rössler, and M. Suhrke, 1998, Europhys. Lett. **42**, 529.
Steffens, O., and M. Suhrke, 1999, Phys. Rev. Lett. **82**, 3891.
Steffens, O., M. Suhrke, and U. Rössler, 1998a, Europhys. Lett. **44**, 222.
Steffens, O., M. Suhrke, and U. Rössler, 1998b, Physica B **256**, 147.
Stewart, D. R., D. Sprinzak, C. M. Marcus, C. I. Duruöz, and J. S. Harris, Jr., 1997, Science **278**, 1784.
Stopa, M., 1993, Phys. Rev. B **48**, 18 340.
Stopa, M., 1996, Phys. Rev. B **54**, 13 767.
Stranski, I. N., and L. von Krastanow, 1939, Sitzungsber. Akad. Wiss. Wien, Math.-Naturwiss. Kl., Abt. 2B **146**, 797.
Su, B., V. I. Goldman, and J. E. Cunningham, 1992a, Science **255**, 313.
Su, B., V. I. Goldman, and J. E. Cunningham, 1992b, Phys. Rev. B **46**, 7644.
Su, B., V. I. Goldman, and J. E. Cunningham, 1994, Surf. Sci. **305**, 566.
Sun, Q., J. Wang, and T. Lin, 2000, Phys. Rev. B **61**, 12 643.
Szafran, B., J. Adamowski, and S. Bednarek, 2000, Phys. Rev. B **61**, 1971.
Tamm, I., 1932, Phys. Z. Sowjetunion **1**, 733.
Tan, W.-C., and J. C. Inkson, 1999, Phys. Rev. B **60**, 5626.
Tanaka, Y., and H. Akera, 1996, Phys. Rev. B **53**, 3901.
Tanatar, B., and D. M. Ceperley, 1989, Phys. Rev. B **39**, 5005.
Tarucha, S., D. G. Austing, and T. Honda, 1995, Superlattices Microstruct. **18**, 121.
Tarucha, S., D. G. Austing, T. Honda, R. J. van der Haage, and L. Kouwenhoven, 1996, Phys. Rev. Lett. **77**, 3613.
Taut, M., 1994, J. Phys. A **27**, 1045.
Tejedor, C., L. Martín-Moreno, J. J. Palacios, J. H. Oaknin, G. Chiappe, and E. Louis, 1994, Phys. Scr., T **55**, 20.
Thornton, T. J., M. Pepper, H. Ahmed, D. Andrews, and G. J. Davies, 1986, Phys. Rev. Lett. **56**, 1198.
Trugman, S. A., and S. Kivelson, 1985, Phys. Rev. B **31**, 5280.
Ullrich, C. A., and G. Vignale, 2000, Phys. Rev. B **61**, 2729.
van der Wiel, W. G., S. De Franceschi, J. M. Elzermann, T. Fujisawa, S. Tarucha, and L. P. Kouwenhoven, 2002, Rev. Mod. Phys. (in press).
van Houten, H., and C. W. J. Beenakker, 1989, Phys. Rev. Lett. **63**, 1893.
Viefers, S., P. S. Deo, S. M. Reimann, M. Manninen, and M. Koskinen, 2000, Phys. Rev. B **62**, 10 668.
Viefers, S., T. H. Hansson, and S. M. Reimann, 2000, Phys. Rev. A **62**, 053604.
Vignale, G., and M. Rasolt, 1987, Phys. Rev. Lett. **59**, 2360.
Vignale, G., and M. Rasolt, 1988, Phys. Rev. B **37**, 10 685.
von Barth, U., and L. Hedin, 1972, J. Phys. C **5**, 1629.
von Delft, J., and D. C. Ralph, 2001, Phys. Rep. **345**, 61.
Wagner, M., U. Merkt, and A. V. Chaplik, 1992, Phys. Rev. B **45**, 1951.
Wang, L., J. K. Zhang, and A. R. Bishop, 1994, Phys. Rev. Lett. **73**, 585.
Waugh, F. R., M. J. Berry, D. J. Mar, R. M. Westervelt, K. L. Campman, and A. C. Gossard, 1995, Phys. Rev. Lett. **75**, 705.
Wegscheider, W., and G. Abstreiter, 1998, Phys. Bl. **54**, 1115 (in German).
Wegscheider, W., L. N. Pfeiffer, and K. W. West, 1996, in *Advances in Solid State Physics*, edited by R. Helbig (Vieweg, Braunschweig), Vol. 35, p. 155.
Weinmann, D., W. Häusler, and B. Kramer, 1995, Phys. Rev. Lett. **74**, 984.
Weis, J., R. J. Haug, K. von Klitzing, and K. Ploog, 1992, Phys. Rev. B **46**, 12 837.
Weis, J., R. J. Haug, K. von Klitzing, and K. Ploog, 1993, Phys. Rev. Lett. **71**, 4019.
Wensauer, A., O. Steffens, M. Suhrke, and U. Rössler, 2000, Phys. Rev. B **62**, 2605.
Wheeler, R. G., K. K. Choi, A. Goel, R. Wisnieff, and D. E. Prober, 1982, Phys. Rev. Lett. **49**, 1674.
Wieman, C. E., 2001, Nobel lecture. See http://www.nobel.se/physics/laureates/2001/wieman-lecture.html
Wigner, E. P., 1934, Phys. Rev. **46**, 1002.
Wójs, A., and P. Hawrylak, 1996, Phys. Rev. B **53**, 10 841.
Wójs, A., and P. Hawrylak, 1997, Phys. Rev. B **56**, 13 227.
Wong, C. Y., 1970, Phys. Lett. **32B**, 668.
Yakimenko, I. I., A. M. Bychkov, and K.-F. Berggren, 2001, Phys. Rev. B **63**, 165309.
Yang, K., F. D. M. Haldane, E. H. Rezayi, 2001, Phys. Rev. B **64**, 081301.
Yang, S.-R. E., and A. H. MacDonald, 2002, Phys. Rev. B **66**, 041202.
Yang, S.-R. E., A. H. MacDonald, and M. D. Johnson, 1993, Phys. Rev. Lett. **71**, 3194.
Yannouleas, C., and U. Landman, 1999, Phys. Rev. Lett. **82**, 5325.
Yannouleas, C., and U. Landman, 2000a, Phys. Rev. Lett. **85**, 1726.
Yannouleas, C., and U. Landman, 2000b, Phys. Rev. B **61**, 15 895.
Yip, S. K., 1991, Phys. Rev. B **43**, 1707.
Yoshioka, D., 1984, Phys. Rev. B **29**, 6833.
Zangwill, A., 1988, *Physics at Surfaces* (Cambridge University, Cambridge, England).
Zeller, H. R., and I. Giaever, 1969, Phys. Rev. **181**, 789.
Zeng, Y. H., B. Goodman, and R. A. Serota, 1993, Phys. Rev. B **47**, 15 660.
Zhang, S. C., T. H. Hansson, and S. Kivelson, 1988, Phys. Rev. Lett. **62**, 82.
Zhitenev, N. B., R. C. Ashoori, L. N. Pfeiffer, and K. W. West, 1997, Phys. Rev. Lett. **79**, 2308.
Zhitenev, N. B., M. Brodsky, R. C. Ashoori, L. N. Pfeiffer, and K. W. West, 1999, Science **285**, 715.
Zhu, J.-L., 2000, Phys. Lett. A **269**, 343.